STRUCTURE-PROPERTY RELATIONS ON STRAIN-MEDIATED MULTIFERROIC HETEROSTRUCTURES

Min Gao

Dissertation submitted to the faculty of the Virginia Polytechnic Institute and State University in partial fulfillment of the requirements for the degree of

Doctor of Philosophy

In

Materials Science and Engineering

Dwight D. Viehland, Chair
Jiefang Li
Marius K. Orlowski
Alex O. Aning

November 5th, 2019
Blacksburg, Virginia

Keywords: multiferroic, thin films, phase transition, strain engineering, domain engineering, adaptive phase theory, energy storage, antiferroelectricity, antiferromagnetism.

Structure-Property Relations on Strain-Mediated Multiferroic Heterostructures

Min Gao

ABSTRACT

Multiferroic thin-film heterostructures have attracted a great deal of attention due to the increasing demand for novel energy-efficient micro/nano-electronic devices. Both single phase multiferroic materials like $BiFeO_3$ (BFO) thin films, and strain-mediated magnetoelectric (ME) nanocomposites, have the potential to fulfill a number of functional requirements in actual applications—principally, direct control of magnetization by the application of an electric field (E) and vice-versa. From the perspective of material science, however, it is essential to develop a fuller understanding of the complex fabrication-structure-property triangle relationship for these multiferroic thin films.

Pulsed laser deposition (PLD) was used in this study to fabricate diverse epitaxial thin film heterostructures on top of single crystal substrates. The crystal structure, phase transition processes (amongst nanodomain distributions, dielectric phases, magnetic spin states, etc.), and various ME-related properties were characterized under different E or temperature environments. Resulting data enabled us to determine the structure-property relationships for a range of multiferroic systems.

First, BFO-based heterostructures were studied. Epitaxial BFO thin films were deposited on top of (001)-oriented $Pb(Mg_{1/3}Nb_{2/3})O_3$-$30PbTiO_3$ (PMN-30PT) single crystal substrates. The strain states of BFO and crystal structural phases were tunable by E applied on the PMN-30PT via both the in-plane and out-of-plane modes. The strain-mediated antiferromagnetic state changes of BFO were also studied using neutron diffraction spectroscopy under E. Then, $CoFe_2O_4$(CFO)/tetragonal BFO nanocomposites were successfully fabricated on top of (001)-

oriented $LaAlO_3$ single crystal substrates. The surface morphology, crystal structure, magnetic properties, and ME effects were evaluated and compared with CFO/rhombohedral BFO nanocomposites.

To enhance the performance of ME heterostructures with PMN-PT substrates, PMN-30PT single crystals with nanograted electrodes were also studied, which evidenced an enhancement in piezoelectric properties and dielectric constant by 36.7% and 38.3%, respectively. X-ray diffraction reciprocal space mapping (RSM) was used to monitor E-induced changes in the apparent symmetry and domain distribution of near-surface regions for the nanograted PMN-30PT crystals.

Finally, in order to add antiferroelectric thin films to the family of strain-mediated multiferroic nanocomposites, epitaxial antiferroelectric thin films were prepared. Epitaxial $(Pb_{0.98}La_{0.02})(Zr_{0.95}Ti_{0.05})O_3$ (PLZT) thin films were deposited on differently oriented $SrTiO_3$ single crystal substrates. A thickness dependent incommensurate/commensurate antiferroelectric-to-ferroelectric phase transition was identified. The crystal structure, phase transition characteristics and pathways, and energy storage behaviors from room temperature to 250 °C were studied, enabling a more systematic understanding of PLZT-based AFE epitaxial thin films.

To summarize, a range of epitaxial thin films were prepared using PLD, whose crystal structures and multiferroic properties were related through the strain. Accordingly, properties such as dielectricity, antiferroelectricity, and antiferromagnetism could be adjusted by E. This study sheds further light on the potential for designing desirable strain-mediated multiferroic nano-/micro-devices in the future.

Structure-Property Relations on Strain-Mediated Multiferroic Heterostructures

Min Gao

GENERAL AUDIENCE ABSTRACT

As a general definition, the class of materials known as multiferroics possess more than one ferroic order parameter. Multiferroic thin-film heterostructures have attracted a great deal of attention due to the increasing demand for novel energy-efficient micro/nano-electronic devices. Both single phase multiferroic materials like $BiFeO_3$ (BFO) thin films and strain-mediated magnetoelectric (ME) nanocomposites show significant potential for use in next-generation devices due to the fact that one can control magnetic properties via the application of an electric field (E) and vice-versa. From the perspective of material science, however, it is essential to develop a fuller understanding of the complex fabrication-structure-property triangle relationship for these multiferroic thin films.

In this study, diverse epitaxial thin film heterostructures were fabricated on top of single crystal substrates. The crystal structure, phase transition processes (amongst nanodomain distributions, dielectric phases, magnetic spin states, etc.), and various ME-related properties were characterized under different E or temperature environments. Resulting data enabled us to determine the structure-property relationships for a range of multiferroic systems.

First, BFO-based heterostructures were studied. Epitaxial BFO thin films were deposited on top of (001)-oriented $Pb(Mg_{1/3}Nb_{2/3})O_3$-$30PbTiO_3$ (PMN-30PT) single crystal substrates. The strain states of BFO and crystal structural phases were tunable by E applied on the PMN-30PT via both the in-plane and out-of-plane modes. The strain-mediated antiferromagnetic state changes of BFO were studied using powerful neutron diffraction spectroscopy under E. Then, $CoFe_2O_4$(CFO)/tetragonal BFO nanocomposites were successfully fabricated on top of (001)-

oriented $LaAlO_3$ single crystal substrates. The surface morphology, crystal structure, magnetic properties, and ME effects were discussed and compared with CFO/rhombohedral BFO nanocomposites.

To enhance the performance of ME heterostructures with PMN-PT substrates, PMN-PT single crystals with nanograted electrodes were also studied, which evidenced an enhancement in piezoelectric properties and dielectric constant by 36.7% and 38.3%, respectively. X-ray diffraction reciprocal space mapping (RSM) technique was used to monitor E-induced changes in the apparent symmetry and domain distribution of near-surface regions for nanograted PMN-PT crystals.

Finally, in order to add antiferroelectric thin films to the family of strain-mediated multiferroic nanocomposites, epitaxial antiferroelectric thin films were prepared. Epitaxial $(Pb_{0.98}La_{0.02})(Zr_{0.95}Ti_{0.05})O_3$ (PLZT) thin films were deposited on differently oriented $SrTiO_3$ substrates. A thickness dependent incommensurate antiferroelectric-to-ferroelectric phase transition was identified. The crystal structure, phase transition characteristics and pathways, and energy storage behaviors from room temperature to 250 ℃ were studied, enabling a more systematic understanding of PLZT-based AFE epitaxial thin films.

To summarize, a range of epitaxial perovskite thin films were prepared, whose crystal structures and multiferroic properties were related through the strain. Accordingly, the properties such as dielectricity, antiferroelectricity, and antiferromagnetism could be adjusted by E. This study sheds further light on the potential for designing desirable strain-mediated multiferroic nano-/micro-devices in the future.

ACKNOWLEDGEMENTS

First, I would like to thank my advisor Prof. Dwight D. Viehland for his patience, encouragement, and unwavering support. The motto on his desk, “Trust me, I am a doctor”, became the great attraction and encouraged me to pursue my Ph.D. degree. During my studies here, I have always been deeply inspired by his scientific knowledge and passion for research. I have benefited so much from many thoughtful discussions about our mutual research interests, his thorough hand-written corrections on my manuscripts and proposals, and his enthusiastic assistance on my conference presentations—all of which significantly impacted my progress as a Ph.D. student and researcher. I cannot thank him enough for his invaluable help in making me a confident young scientist.

Equally important, I would like to express my sincerest gratitude to Dr. Jiefang Li for her countless instances of support and insightful suggestions. She was always the first person to appear for help when I had trouble in testing. Without her experienced knowledge in experimental techniques, I would not have been able to accomplish my research plans. In addition, as a foreign student in the U.S., I particularly want to thank Dr. Li for her efforts toward building a warm and harmonious academic environment for us.

I would like to thank Dr. Alex O. Aning and Dr. Marius Orlowski for serving as my committee members, and their helpful suggestions for my dissertation.

It would be remiss if I did not thank all the faculty and staff in the MSE department for their kind help, making me feel comfortable and be able to focus on my studies and research at Virginia Tech.

I also extend my thanks to my colleagues and fellow researchers in Dr. Viehland's group: Xiao Tang, Junran Xu, Dr. Chengtao Luo, Dr. Chung Ming Leung, Dr. Xin Zhuang, and Dr. Yanxi Li, for their shared experimental experience and valuable comments on my research.

For assistance with TEM measurements, I must thank Dr. Christopher Winkler at the Nanoscale Characterization and Fabrication Laboratory (NCFL) for his patient training and instrument support. His remarkable skill with the TEM and his dedicated attitude is impressive.

I also want to acknowledge the help of Dr. Wei Tian at Oak Ridge National Lab (ORNL), for her selfless guidance and assistance on my neutron diffraction measurements. I also appreciate that she trusted me to conduct these complex experiments at the national lab and work with many outstanding scientists.

Finally, I would like to express my deepest gratefulness to my parents, Xingfang Zheng and Wenchao Gao, for their constant faith and encouragement during my Ph.D. studies. I will be forever grateful for their unconditional love and support.

TABLE OF CONTENTS

LIST OF FIGURES

LIST OF TABLES

Chapter 1. Introduction

1.1. Multiferroics

As a general definition, the class of materials known as multiferroics possesses more than one ferroic order parameter (i.e., ferroelectricity, ferromagnetism, ferroelasticity, or ferrotoroidicity in most cases) [1-3]. Compared to traditional materials whose ferroic properties can be tuned by its conjugate field, multiferroic materials feature the ability to manipulate one ferroic property via the others, as all these parameters are coupled together [4,5]. This characteristic provides a range of approaches for tailoring one property, and thus has great potential for application to a range of microelectronics devices—notably sensors, memory technologies, and novel spintronic devices [6].

Ferroelectricity (FE) refers to a group of crystals where spontaneous dielectric dipoles (or electrical polarizations) exist without an external electric field (E), forming FE domains. Such FE domains can further be rotated by E [7]. Similarly, for ferromagnetic materials, spontaneous magnetization (and magnetic domains) is switchable under application of an external magnetic field (H) [8]. In contrast, in the case of ferroelasticity, a spontaneous deformation occurs in response to an applied stress [3]. Finally, ferrotoroidicity, which is a relatively new concept, indicates a stable and spontaneous order parameter that is understood to be the curl of a magnetization or polarization [4,9]. However, given the fact that ferrotoroidic materials are still lack of unambiguous evidence [4], they will not be discussed herein.

The linear coupling between ferroelectricity and ferroelasticity is known as piezoelectricity, which is important for the development of sensors, actuators, and transducers [4]. In comparison, the quadratic coupling between ferromagnetism and ferroelasticity is known as magnetostriction, which has also been exploited in the transducer industry for the production of

magneto-mechanical actuators [7]. Although linear piezomagnetism and quadratic electrostriction also exist, they are usually negligible due to their subtler influences. Importantly, magnetoelectricity (or electromagnetism), which refers to the coupling between the FE and ferromagnetic order parameters, is attracting a great of attentions in recent years due to the fact that it facilitates the direct control of magnetization by E and vice-versa [1,2,4-6,10,11]. In principle, such E-controlled magnetizations in multiferroic materials permit data to be written electrically and read magnetically, which is very energy-efficient and is guiding the way toward achieving ferroelectric random access memory (FeRAM) and magnetic data storage [4].

Magnetoelectric (ME) coupling can be evaluated by the ME coefficient (α_{ij}), which is defined by the following equations [12]:

$$P_i = \alpha_{ij} H_j, \text{ or } M_i = \alpha_{ij} E_j. \quad 1.1$$

Figure 1.1 provides a schematic illustration demonstrating the relationships amongst these various ferroic orders.

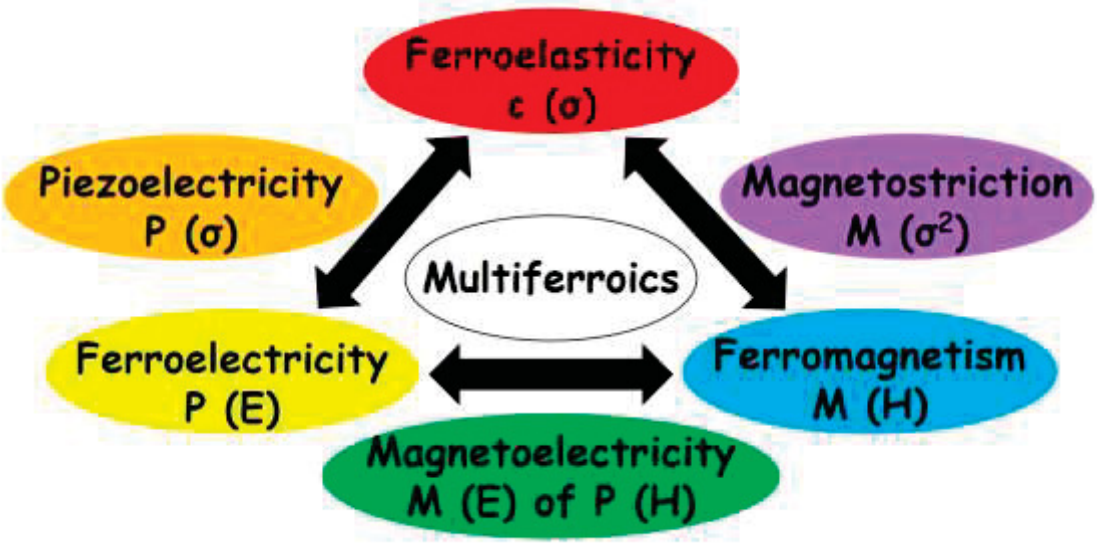

Figure 1.1: Schematic illustration of the coupling of ferroic orders in multiferroics. σ: stress, ε: strain, E: electric field, P: polarization, H: magnetic field, M: magnetization.

Although the terminology associated with multiferroics primarily addresses the coupling amongst primary ferroic orders, it has been extended to include non-primary orders as well (i.e., antiferromagnetism, antiferroelectricity, or ferrimagnetism) [2,13,14]. Thus, in a broad sense, current investigations of ME coupling are also likely to address the interaction between the ferromagnetism (or antiferromagnetism, or ferrimagnetism) and ferroelectricity (or antiferroelectricity). Antiferromagnetism (antiferroelectricity) refers to a kind of materials that possesses ordered magnetic (dipole) moments that cancel each other completely within each unit cell [4]. In other words, antiferromagnetic (antiferroelectric) materials will not display magnetic (ferroelectric) characteristics, even in external magnetic (electric) fields [15]. Unless an external field is sufficiently large to break the antiparallel magnetic (dipole) couplings and realign them in a uniformly parallel configuration, leading to a phase transition from antiferromagnetism (antiferroelectricity) to ferromagnetism (ferroelectricity) [16,17]. Additionally, if the adjacent antiparallel magnetic moments do not completely cancel each other out, it is known as ferrimagnetism [4]. Figure 1.2 exhibits the different moment arrangement patterns discussed above.

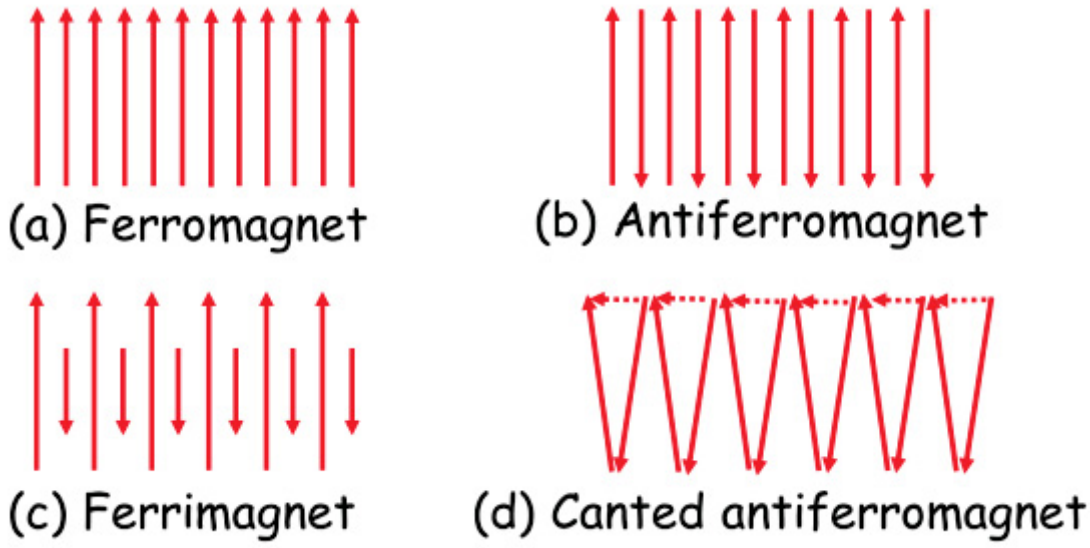

Figure 1.2: Schematic illustration of the moment arrangements of (a) ferromagnetism, (b) antiferromagnetism, (c) ferrimagnetism, and (d) canted antiferromagnetism that generates a non-zero net magnetization (dotted arrows). The dipole moments in FE and antiferroelectric materials arrange similarly to those in (a) and (b), respectively.

Linear ME coupling in a single phase multiferroic can be described using traditional Landau theory by expanding the free energy of the system in terms of the applied H and E [18-20]. The first single phase multiferroic material that showed linear ME coupling was observed in Cr_2O_3 in 1960 [21,22], followed by the identification of several complex compounds thereafter, notably, (1-x)$Pb(Fe_{2/3}W_{1/3})O_3$-x$Pb(Mg_{1/2}W_{1/2})O_3$ in 1961 [23], $Ni_3B_7O_{13}I$ in 1966 [24], $BaCoF_4$ in 1970 [25], etc. However, the ME coupling coefficient ($\alpha \approx 10$ mV·Oe^{-1}·cm^{-1}) in single-phase multiferroics was found to be very weak and only able to exist at very low temperature [7,26]. Moreover, it was theoretically predicted that ferroelectricity and ferromagnetism would be mutually exclusive, based on the incompatible requirement of an empty d shell for the transition metal ion in ferroelectrics and a partially filled d shell for the transition metal magnetic materials [11,27,28].

Therefore, observations of single phase ME materials were relatively rare, which hindered their industrial applications.

One effective way to overcome the contradictory nature of single-phase ME materials is to fabricate ME composites consisting of both piezoelectric and magnetostrictive materials, where the FE and ferromagnetic orders are able to couple together via strains at the interfaces. Such ME composites were firstly achieved in bulk form, with a laminate structure, in which the ME coefficient at room temperature was significantly higher than that of the single phase ones under extreme conditions. For example, an ME coefficient of 52 $V \cdot Oe^{-1} \cdot cm^{-1}$ was reported for the multilayer Metglas/$Pb(Mg_{1/3}Nb_{2/3})O_3$-$PbTiO_3$ single crystal composite bonded by epoxy [29]. These bulk ME composites have already been incorporated in sensors and transducers [30].

With developments in fabrication techniques, spurred on by increasing demand within the microelectronics industry, significant effort has been directed at miniaturizing ME composites at the nano-scale level [2,31]. Since ME nanocomposites are strain-mediated, the actual interface condition between the piezoelectric phase and magnetostrictive phase plays a key role in improving the final ME coupling—that is, how these two phases are combined is crucial. Accordingly, ME nanocomposites can be classified into (0-3), (2-2), and (1-3) type structures, as shown in Figure 1.3 [31]. The structure is determined principally by the fabrication technique, detailed fabrication conditions, crystal structure and lattice parameters of each phase, and the compositional ratio between two phases. The (0-3) type ME nanocomposite can be fabricated relatively easily by sol-gel or other chemical methods [32,33]. For example, the nanoparticulate $Bi_{3.15}Nd_{0.85}Ti_3O_{12}$-$CoFe_2O_4$ composite exhibits 34.5 $mV \cdot Oe^{-1} \cdot cm^{-1}$ at a bias magnetic field of 6.5 kOe [33]. The (1-3) type ME nanocomposites usually feature the largest interface area in comparison, to the other two types. As a result, the ME coefficient in (1-3) type nanocomposites is relatively

stronger—i.e., about 51.8 $mV \cdot Oe^{-1} \cdot cm^{-1}$ in $BaTiO_3$-$CoFe_2O_4$ nanocomposite [34]. However, the self-assembled (1-3) type nanocomposites are restricted within the regions of spinel-type magnetostrictive materials and perovskite-type piezoelectric materials [31,35,36]. Another drawback is that it is hard to control the fabrication process because the driving force behind the forming of self-assembled structures involves the minimization of interfacial energy, which results from the significant difference in surface energy anisotropy between spinels and perovskites [36].

The (2-2) type structure ME nanocomposites, on the other hand, feature significantly more advantages than the other two structures—the main one being the fact the (2-2) type thin films are easy to integrate with currently available microelectronic chips [2,31]. Moreover, with the help of the pulsed laser deposition (PLD) technique, it is possible to grow epitaxial multilayer thin films, whose interfaces are coherent and thus can deliver a great deal of strain due to the lattice mismatch [2]. Thus, for this dissertation, the ME nanocomposites that are utilized are all (2-2) type structure. In the following sections, the details of the related materials are introduced separately.

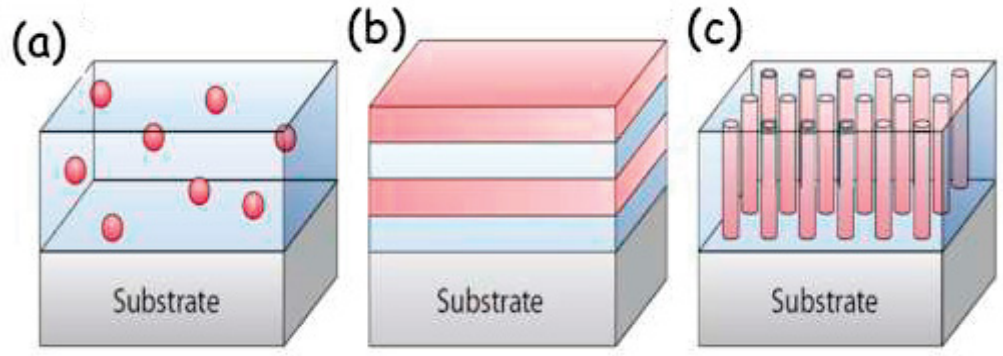

Figure 1.3: Schematic illustration of ME nanocomposites: (a) (0-3) type particulate nanocomposite films with nanoparticles ('0') embedded in a film matrix ('3'); (b) (2-2) horizontal heterostructure with alternating piezoelectric and magnetostrictive layers ('2'), or simply a piezoelectric (or magnetostrctive) thin film grown on a magnetostrictive (or piezoelectric) substrate; (c) (1-3) vertically aligned heterostructure with one phase nanopillars ('1') embedded epitaxially in the other phase's film matrix ('3') [31]*. ([31] Kleemann, W. Multiferroic and magnetoelectric nanocomposites for data processing. Journal of Physics D: Applied Physics 50, 223001, (2017).) Used under fair use, 2019.*

1.2. Bismuth ferrite: the single phase multiferroic material and strain engineering

The bismuth ferrite $BiFeO_3$ (BFO) is classified as rhombohedral (R, point group R3c) at room temperature [37]. It exhibits a typical perovskite structure with the lattice parameter a_{pc} of 3.965 Å (in the pseudocubic index) and rhombohedral angle of 89.3 ° [38], where the Bi^{3+} cation, Fe^{3+} cation, and O^{2-} anions are located at the corner, at the body center, and at the face centers of the unit cell, respectively [15].

To date, BFO is the only known single phase multiferroic material at room temperature [39]. It has coexisting antiferromagnetic (Neel temperature T_N ~ 643K) and FE (Curie temperature T_C ~ 1103K) orders [39,40], which are linearly coupled via the Dzyaloshinskii–Moriya (DM) interaction

[41]. Unlike typical perovskite materials whose FE comes from the displacement of the center ion (B site cation), the polarization in BFO is mostly caused by the long pair (s^2 orbital) of Bi^{3+} (A site cation) [39]. In contrast, the antiferromagnetism stems from the center Fe^{3+} cation [15]. Thus, the difference in origins (A site and B site cations) means that BFO is able to overcome the exclusive nature of the FE and antiferromagneism, making it a promising multiferroic material.

Although BFO was first synthesized in 1957 [42], little progress has been made in elucidating its physical properties. For example, BFO's important FE characteristics could not be proved due to its extremely low resistivity [43]. Furthermore, the neutron diffraction structure analysis claimed that the space group R3c permits weak ferromagnetism, which has yet been observed under experimental conditions [44]. It was at the beginning of the 21st century, however, when the stabilization of BFO in the epitaxial thin film form was achieved by PLD, researchers have again turned their attention to this promising multiferroic material [39,45].

Usually, BFO thin films maintain the R structure, where the FE polarization is along the $<111>_{pc}$ direction [38]. Due to the high quality of epitaxial thin films, the saturation polarization is much larger compared to that in bulk (i.e., ~100 μC/cm^2 for thin films [45] versus ~6.1 μC/cm^2 for bulk [43]), which has remarkable potential for future industrial applications. With the help of piezoresponse force microscopy (PFM), many experiments have been conducted to investigate FE domain characteristics—even involving rotating the polarization by applying a local E [46-48]. Atomic-level transmission electron microscopy (TEM) has also been used to reveal the local ion displacement distribution (and/or oxygen octahedron distortion) in BFO [49,50].

The antiferromagnetic properties of BFO, on the other hand, are strongly related to the epitaxial strain that imposed by the substrate [51]. In principle, the short-range magnetic ordering in bulk BFO should show the G-type antiferromagnetic configuration; that is, each Fe^{3+} spin would

be antiparallel to its six nearest Fe neighbors [52]. However, these spins are not perfectly antiparallel due to the DM interaction with the local polarization, leading to a weak canting moment (see Fig. 1.2d) [41]. Actually, a long-range modulation of G-type antiferromagnetic structure was proposed, suggesting a theoretical model that antiparallel spins were modified into a cycloidal spiral with a long period of 62-64 nm [53,54]. Because the spins should be perpendicular to the polarization direction, the cycloidal plane is defined by the $[10\text{-}1]_{pc}$ propagation vector and the $[111]_{pc}$ polarization vector, as described in Figure 1.4a [54]. However, the epitaxial strain in BFO thin films could break such cycloid structure, releasing the weak canting ferromagnetic moments [45,55]. Recently, strain engineering has been intensively investigated due to its ability to obtain various antiferromagnetic states by epitaxial strains, as predicted in Figure 1.4b [51]. Accordingly, novel functionalities in BFO-related heterostructures, such as photovoltaic effect in BFO/$La_{0.7}Sr_{0.3}MnO_3$ bilayers [56] and exchange bias in $Co_{90}Fe_{10}$/BFO bilayers [57], can be tailored efficiently through the use of epitaxial strain.

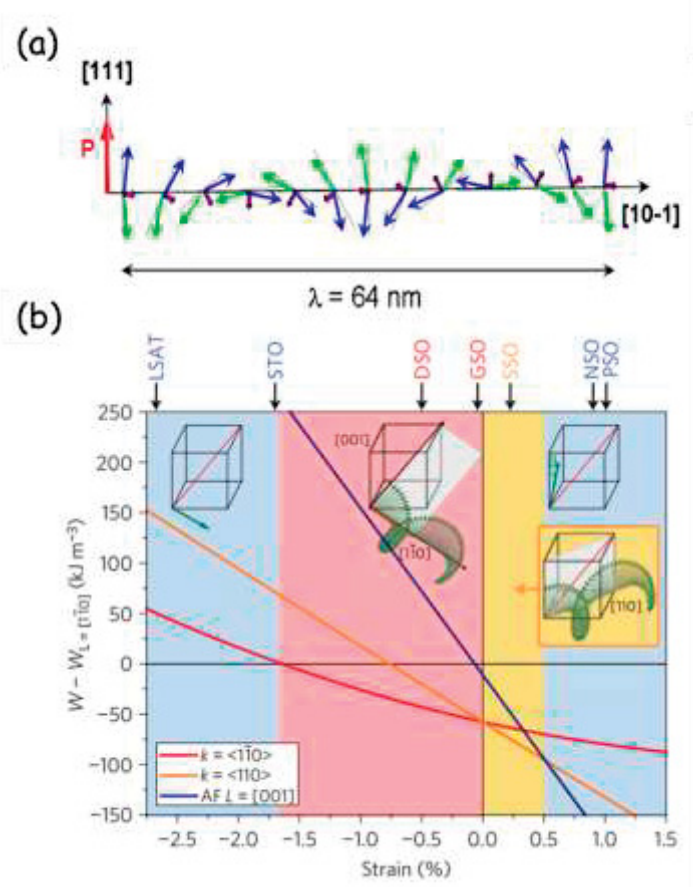

Figure 1.4: (a) Schematics of the 64 nm antiferromagnetic circular cycloid propagating along the [10-1] direction [54]. (b) Magnetic phase diagram of strained BFO films. The energy of different magnetic states and their stable regions are shown as a function of the in-plane strains. Blue: antiferromagnetic state with antiferromagnetic vector close to [001] or [1-10]; red: type-1 cycloid with propagation vector along the <1-10> directions (the cycloid plane is (11-2)), equivalent to that shown in (a); orange: type-2 cycloid with propagation vector along the <110> directions (the cycloid plane is (1-10)). The substrates used are listed on the top at their corresponding strain [51]. ([51] Sando, D. et al. Crafting the magnetic and spintronic response of $BiFeO_3$ films by epitaxial strain. Nature Materials 12, 641, (2013). [54] Lebeugle, D. et al. Electric-Field-Induced Spin Flop in BFO3 Single Crystals at Room Temperature. Physical Review Letters 100, 227602, (2008).) Used under fair use, 2019.

The primary factor determining the internal strain of BFO is its lattice mismatch with the substrate or a buffer layer. Substrate-induced phase transitions have been reported such as from the R phase to the mixed R-tetragonal (T) phase under large (-5%) compressive strain by choosing (001) $LaAlO_3$ (LAO) substrates [58], or to the orthorhombic (O) phase under biaxial tensile strain on (110) $NdScO_3$ substrates [46]. These T or O phases have unique properties that cannot be observed in the bulk R phase BFO. For instance, the T phase BFO thin film exhibits an enhanced polarization of ~150 $\mu C/cm^2$ along the $[001]_T$ direction, and a C-type antiferromagnetic order (i.e., the intra-plane coupling is antiferromagnetic while the inter-plane coupling is ferromagnetic) [59,60]. Although there have been many breakthroughs related to R phase BFO with suitable strain characteristics, investigations on the T phase BFO nanocomposites are currently lacking [2].

While the lattice parameter mismatch, as well as deposition conditions, determine the intrinsic strain state of BFO thin films, people are seeking to extrinsically manipulate the strain state of BFO by applied E, with the goal of achieving the strain-mediated ME effect [1,2,8,31,56,57]. One promising method is using a piezoelectric single crystal as the substrate so that the E applied on the substrate can induce its lattice parameter change, which will affect the strain and further the magnetic state of BFO on the top [8,56,57]. Amongst them, one excellent candidate here is the $Pb(Mg_{1/3}Nb_{2/3})O_3$-x%$PbTiO_3$ (PMN-xPT) single crystals.

1.3. $Pb(Mg_{1/3}Nb_{2/3})O_3$-$PbTiO_3$ single crystals, domain engineering, and adaptive phase theory

PMN-xPT single crystals have been widely investigated due to their exceptional piezoelectric coefficient (d_{33} > 2500 pC/N) and ultrahigh electromechanical coupling coefficient (k_{33} > 94%), especially for compositions near the morphotropic phase boundary (MPB) between

the R and T phases ($30 \leq x \leq 33$) [61-66]. The outstanding performances of these single crystals have enhanced their utility in applications such as transducers and actuators [30]. As to the scientific researches, PMN-PT single crystals have also been used as FE substrates to fabricate ME nanocomposites [7,8,56,57]. Usually, PMN-30PT is considered as an R structure with a pseudocubic lattice parameter of 4.02 Å [57]. Thus, R phase BFO will suffer a tensile in-plane (IP) strain of 1.38% when epitaxially deposited on the top of the (001) oriented PMN-30PT single crystal substrate [39]. Then, on applying E to the PMN-30PT substrate, the strain state of BFO can be further tuned due to elastic coupling at the interface.

In the vicinity of the MPB, intermediate monoclinic (M_A, M_B, and M_C) phases are well-known as a structural bridge, where symmetry allows the polarization vector to rotate in a plane rather than being confined to one direction (i.e. $(110)_{pc}$ for M_A phase, $[111]_{pc}$ for R phase, and $[001]_T$ for T phase) [67,68]. Figure 1.5a illustrates the R (in the pseudocubic form), M_A, and T phase crystal structures, within which the polarization vector is also indexed. The unpoled condition for PMN-30PT is R, and a small E along the $[001]_{pc}$ direction can alter the phase transitional sequence to being either $R \rightarrow M_A \rightarrow M_C \rightarrow T$ or $R \rightarrow M_A \rightarrow T$, where the M_A phase remains stable on removal of E [69,70]. In the domain-engineered condition, not all the possible M phase domain states are present—but only a small subset thereof, which have specific signatures as shown by x-ray diffraction (XRD) mesh scans [71], as illustrated in Figure 1.5b-d. The M_A phase has a doublet splitting along the transverse (H00) direction, whereas the M_c has a signature triplet peak; note that the R phase has just a single peak. Studies have shown that the phase stability depends on temperature, stress, electrical history, and even the direction along which the E is applied. In short, the phase stability of PMN-PT is quite fragile [70].

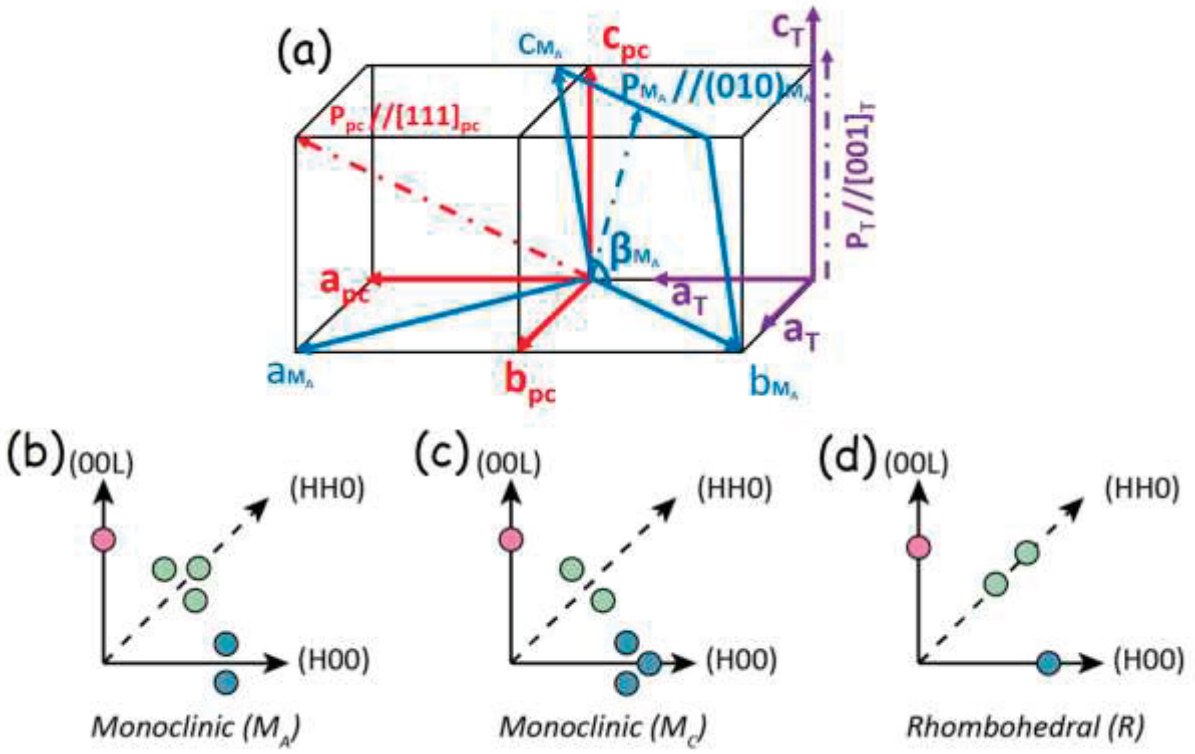

Figure 1.5: (a) Schematic illustration of the R phase (red, in the pseudocubic index), the M_A phase (blue) and the T phase (purple) crystal structures, and the corresponding polarization vector directions. (b)-(d) Illustrations of the mesh scan patterns for the M_A phase, the M_C phase, and the R phase in the $[001]_{pc}$ poled condition, respectively.

A structurally non-uniform model of the nanodomain distribution has been proposed for PMN-PT based on the adaptive phase theory, where particular geometrical invariant conditions determined by the polar nanoregion (PNR) distribution relax the elastic strain energy [72]. General and specific invariant conditions then define these various M phases [72,73]. Researchers initially proposed FE adaptive phase theory in 2000 [74], which is built upon the conformal miniaturization of stress accommodation of the nanotwins and, thus, elastic free energy. This adaptive phase structure is analogous to the case of a martensite transformation, where the hierarchical

arrangement of domains self-organizes into bands to reduce the elastic energy [74,75]. Due to its nanoscale size, which is less than the conventional characteristic length (i.e. the x-ray), the locally spatially inhomogeneous crystal structure may be quite different from the apparent symmetry determined via XRD. With respect to PMN-PT single crystals near the MPB, the PNRs and nanodomains have T or R symmetry [76], although the average crystal structure is M [72,74]. Electron and scanning probe microscopy studies have revealed the existence of PNRs that self-assemble into domain striations along the preferred direction (nanodomains), which are subsequently organized into domain bands (macrodomains) [68,77]. The presence of PNRs and nanodomains demonstrates a high domain wall density, which can increase stored mechanical energy [72,78,79]. This is the origin of the enhancement effect in piezoelectric properties, based on the concept of domain engineering in FE single crystals.

In the domain engineering technique, patterned electrodes have been used during E poling, resulting in an enhancement of the piezoelectric coefficients (d_{33}) in FE single crystals [65,79]. This enhancement results from the combination of reduced domain size and increased domain wall density [72,78,79]. The domain wall density can also be manipulated by doping [80], because surface doping has been shown to enhance the domain nucleation probability, preventing polarization rotation and further increasing the domain wall density in surface regions [77,81]. In a recent study, nanograted titanium/gold/ manganese oxide (Ti/Au/MnO_x) electrodes were fabricated on one side of PMN-30PT single crystal plates, while the other side had a conventional planar Ti/Au electrode. An enhancement of d_{33} and the dielectric constant values is reported by 36.7% and 38.3%, respectively, compared to those crystals with conventional planar gold electrodes [77]. Doping/diffusion with Mn and E-field fringe effect were proposed to explain these findings from the perspective of nanodomain engineering [77].

1.4. Antiferroelectric lanthanum modified lead zirconate titanate, energy storage performance, and ferroelectric relaxors

For FE materials, an applied E can rotate the polarization, stretch the lattice, and most likely eventually induce a structural phase transition, while retaining its FE nature. For antiferroelectric (AFE) materials, since the antiparallel dipoles couple, thereby cancelling each other out, a normal E can barely rotate them. However, if the external E is large enough—namely, exceeding a critical value of $E_{AFE \rightarrow FE}$—it can force the antiparallel dipoles to be parallel, inducing an AFE to FE dielectric phase transition [82,83]. When the external E is reduced to be lower than another critical value of $E_{FE \rightarrow AFE}$, the materials will return to the original AFE phase [83]. As a result, a unique double hysteresis loop is expectable, which is quite different from the normal square-like FE hysteresis loop [82]. Figure 1.6 shows the typical polarization-electric field (P-E) hysteresis loops for paraelectrics (PE), ferroelectrics (FE), and antiferroelectrics (AFE). Experimentally, one can distinguish the different dielectric phases according to the shape of P-E curves.

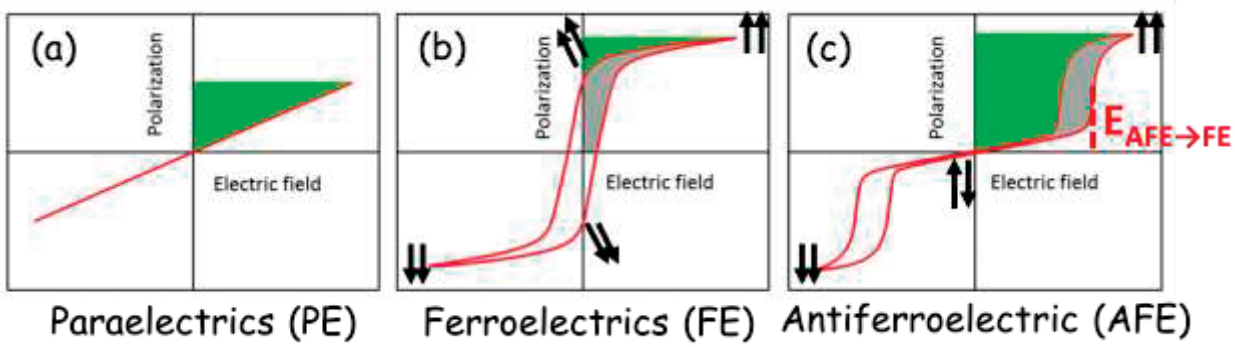

Figure 1.6: P-E hysteresis loops of (a) PE, (b) FE, and (c) AFE materials. The green and gray regions represent the energy storage density and the energy loss density, respectively [82]. ([81] Liu, Z. et al. Antiferroelectrics for Energy Storage Applications: A Review. Advanced Materials Technologies 3, 1800111, doi:10.1002/admt.201800111 (2018).) Used under fair use, 2019.

The induced AFE→FE phase transition is also accompanied by a crystal structure change, usually from the O phase to the R or T phase [83,84]. This process also exhibits a large volume change; thus, an externally imposed stress/strain can offer an additional approach by which to modify the AFE→FE phase transition and transformational pathway [85,86]. Accordingly, the lattice mismatch of AFE films deposited on substrates may impose significant epitaxial strains on the films, changing the AFE→FE transition process [85]. These micro- and/or nano-scale AFE films are ideal for incorporation into current microelectronic devices.

Lead zirconate titanate (PZT) is a well-investigated ABO_3 perovskite system, whose B-site cation ratio (Zr^{4+}/Ti^{4+}) can significantly alter the FE properties from AFE to FE stability [83,87,88]. The Zr^{4+}/Ti^{4+} ratio of 95/5 is desirable as it is close to the MPB between AFE O phase and FE R phase [83,86,89]. La^{3+} doping onto the Pb^{2+} site (A site) is an effective way to stabilize the AFE O phase of PZT to higher titanium content, over the FE R phase [83,90]. Most prior studies of epitaxial PZT and lanthanum modified lead zirconate titanate (PLZT) films have focused on compositions near the MPB between the FE R and T phases ($Zr^{4+}/Ti^{4+}=1$) for actuator/sensor applications [91-93], or on the Ti-rich range (35/65 [94], 20/80 [95,96], etc.) for FE memory. Little is known about the structure and properties of AFE PLZT epitaxial films, especially about how the AFE nature can be tailored by incorporating epitaxial strain.

The AFE PLZT (PZT) is suitable as the dielectric medium in charge energy storage capacitors due to the unique E induced AFE→FE phase transition and small remanent polarization [87,97]. A capacitor is a dielectric medium covered by at least two electrical conductors often in the form of metallic plates. A capacitor can store the potential energy in an E. Since the storage process is related to the rotation of the dipoles within the dielectric medium, its reliability is much better, and the charge/discharge speed is much faster compared to chemical batteries. The energy storage

density (ESD or U_r), energy loss density (ELD or U_{loss}), and total energy density can be determined from the P-E hysteresis loop of the dielectric materials by the following equations:

$$U_r = -2\int_{P_{max}}^{P_r} EdP, \quad 1.2$$

$$U_{loss} = \oint EdP, \quad 1.3$$

$$U_{total} = U_r + U_{loss}, \quad 1.4$$

where P_{max} and P_r are the maximum and remanent polarization, respectively [98,99]. The areas between the vertical axis and the charge and discharge parts of the P-E loops are equivalent to the total energy density and ESD, respectively, whereas the area enclosed by the P-E loop is the ELD (see Fig. 1. 6) [100]. The energy storage efficiency (ESE or η) can be obtained by:

$$\eta = \frac{U_r}{U_r + U_{loss}} \times 100\%. \quad 1.5$$

The PEs have extremely high ESE due to the absence of hysteresis behavior, but the ESD are usually lower than 1 J/cm^3 because of the relatively low dielectric constants [101]. Inversely, FEs possess high dielectric constants but also large remanent polarizations, lowering their ESD and ESE. For the AFE PLZT, the antiparallel dipoles at low E ensure nearly zero remanence, while the AFE→FE phase transition leads to a large dielectric constant at high E. Thus, the AFE PLZT exhibits great potential for the use as the dielectric medium in energy storage devices [82]. For comparison, 10-mm-thick PLZT (8/91/9) ceramics have been reported to have an ESD of 3 J/cm^3, with an ESE of 92% at an E of 180 kV/cm [100]. While 600-nm-thick PLZT (4/98/2) films have been reported to have an ESD of 20 J/cm^3 under E=1200 kV/cm [102]. Such remarkable enhancements of ESD are associated with the fact that thick (or thin) films have much higher dielectric breakdown strength and saturation polarization compared to PLZT ceramics [102,103]. However, most prior studies have focused on polycrystalline AFE PZT films [85,86,89,91,102]. From the perspective of energy-storage capacitor applications, polycrystalline films normally feature a large number of

defects and/or grain boundaries that can reduce the dielectric breakdown strength, and thus decrease ESD [93]. In contrast, epitaxial films with lower concentrations of defects and higher mobility of domain walls can be expected to exhibit improved energy storage capability and thermostability [91].

It is known that La-doping of the PZT system weakens the FE interaction and disrupts the long-range polar order, decomposing the conventional FE domain state into a PNR one, and forming a type of relaxor ferroelectric (RFE) [104,105]. The first significant characteristic of a RFE is a diffuse phase transition that is frequency-dispersive between the FE and PE phases [106]. The dielectric constant peak near T_C is broad and shifts with frequency alterations. The second characteristic is the degeneration of the dielectric hysteresis as the temperature is increased to T_C, resulting in slim and slanted P-E hysteresis loops [107]. The low hysteresis and high saturation polarizations of RFEs reinforce their utility for incorporation in energy storage capacitors [107]. For example, 880-nm-thick relaxor PLZT (8/52/48) thick films have shown ESD of ~31 J/cm^3 with an ESE of 75% at room temperature [93], which is comparable with the AFE PLZT films mentioned above. In addition, these desirable RFE characteristics have also been observed in the PMN-PT single crystals [108,109].

It is also reported a structurally incommensurate AFE phase in the PLZT ceramics system, which reduces the hysteretic loss of the AFE→FE transition [100,102,110]. Incommensuration refers to a state which develops a structural order parameter modulation whose modulation vector is not an integer multiple of the fundamental periodicity of the lattice [83,111]. According to soft mode theory, softening in conventional commensurate structures occur at either the Brillouin zone boundary or a rational fraction of the Brillouin zone relative to the prototype symmetry [111,112]; whereas, in an incommensurate phase, such softening can occur at some irrational positions in the zone [110,113]. It

is believed that the incommensuration can result from a frustrated competition between long-range FE and short-range AFE sublattice interactions [114,115].

1.5. Objectives and significance of the study

This investigation was designed to study the strain-medium couplings between different ferroic materials, as well as to realize E-controlled magnetization manipulation, and vice-versa. This study initially focused on multiferroic BFO thin films. By depositing BFO thin films on (001)-oriented piezoelectric PMN-PT single crystal substrates, the antiferromagnetism of BFO could be tuned by applying an E on the PMN-PT. At the same time, a patterned electrode was used on PMN-PT single crystals to enhance their dielectric performance after poling. On the other hand, to utilize the ferroelectric properties of BFO—and especially in connection with the T-phase BFO (T-BFO)—ferrimagnetic $CoFe_2O_4$ (CFO) was used to deposit CFO/T-BFO nanocomposites on (001)-oriented LAO single crystal substrates. For comparison, CFO/R-BFO nanocomposites were also fabricated on (001)-oriented $SrTiO_3$ (STO) single crystal substrates. Finally, the epitaxial strain effect on AFE properties and energy storage performance was studied by depositing PLZT (2/95/5) thin films on the differently-oriented STO substrates, which represents a prerequisite for extending the traditional strain-medium ferromagnetic-FE coupling effect to the strain-medium ferromagnetic-AFE one.

The specific goals pursued in this investigation are listed below:

(1) To fabricate two modes of BFO/PMN-30PT heterostructures that allow one to apply either in-plane (IP) or out-of-plane (OP) E on PMN-30PT single crystal substrates. A related goal was to demonstrate how the strain in BFO thin films could be manipulated by applied E on PMN-PT [116]. Additionally, this study was designed to monitor how the antiferromagnetic state of BFO

was affected by E-induced strain changes, as well as to understand if the cycloid spins would be broken, or the propagation direction could be adjusted externally.

(2) To understand how patterned nano-electrodes on the surface of the PMN-PT single crystal influence its apparent phase stability and thus enhance the dielectric constant [117].

(3) To fabricate CFO/T-BFO nanocomposites by PLD, and investigate the multiple coupling between the CFO and T-BFO, including the exchange coupling between the ferrimagnetism of CFO and antiferromagnetism of BFO, and the ME coupling between the ferrimagnetism of CFO and FE of BFO [118].

(4) To fabricate PLZT (2/95/5) thin films epitaxially on differently-oriented STO substrates, as well as study how epitaxial strain affects the PLZT thin films' crystal structure, AFE nature, and energy storage behaviors. A related goal was to study the temperature dependent crystal structure stability, dielectric phase evolution, and energy storage stability [119]. Another related goal was to investigate how AFE phase is distributed within the PLZT thin films along the thickness direction [120].

Chapter 2. Experimental Procedures

2.1. Sample preparation

2.1.1. PMN-PT polishing technique

The PMN-PT single crystals used as the substrates in this study were grown by Haosu Luo's group at the Shanghai Institute of Ceramics, China [121-123]. Since the as-grown single crystals featured a rough surface, a surface-polishing process was required prior to use. Prior to the polishing process, a temperature dependent dielectric constant measurement was carried out, from which the T_C was determined. According to our group's prior work, the precise chemical composition of the PMN-PT single crystal could be inferred from the T_C value [8].

Once the composition was confirmed, the silver paste on the surface was removed using sandpapers of differing grits. The thickness of the single crystal substrate was also modified by sandpaper and measured by a vernier micrometer. After the surface of the PMN-PT single crystal substrates were polished using a 1200-grit sandpaper, the substrate was mounted on an adjustable sample holder, which was further mounted onto the polishing head of the Single Sample Polisher (Buehler). An improved four-step-polishing process was used, which was based on our group's prior three-step-relief-polishing method [7]. The details of each step are provided in Table 2.1. An added fourth step was to maximally remove the abrasive silica residuals, although a final water rinse and ultrasonic cleaning step was still required. The ultrasonic cleaning was done in acetone and ethanol, separately.

Step	Process	Base	Abrasive	Grad (μm)	Speed (rpm)	Pressure (lb)	Time (min)
1	Lapping	Chem cloth	Diamond suspension	3	50	5	30
2	Polishing	Nylon cloth	Diamond suspension	1	50	5	15
3	Fine polishing	Final finishing cloth	Colloidal silica	0.04	50	5	2
4	Post-cleaning	Final finishing cloth	DI water	N/A	50	5	2

Table 2.1: Detailed parameters of the four-step-polishing process for PMN-PT single crystals performed in our group.

After each step of polishing, the surface of the PMN-PT was checked by atomic force microscope (AFM, Veeco SPI 3100). Figure 2.1 shows the AFM height and phase images of the polished PMN-30PT at each step. The pits and scratches visible in the first two steps were almost removed completely, and the surface roughness could be reduced to about 2 nm. The mosaic surface morphology represented the unique FE domain structure of PMN-30PT [124].

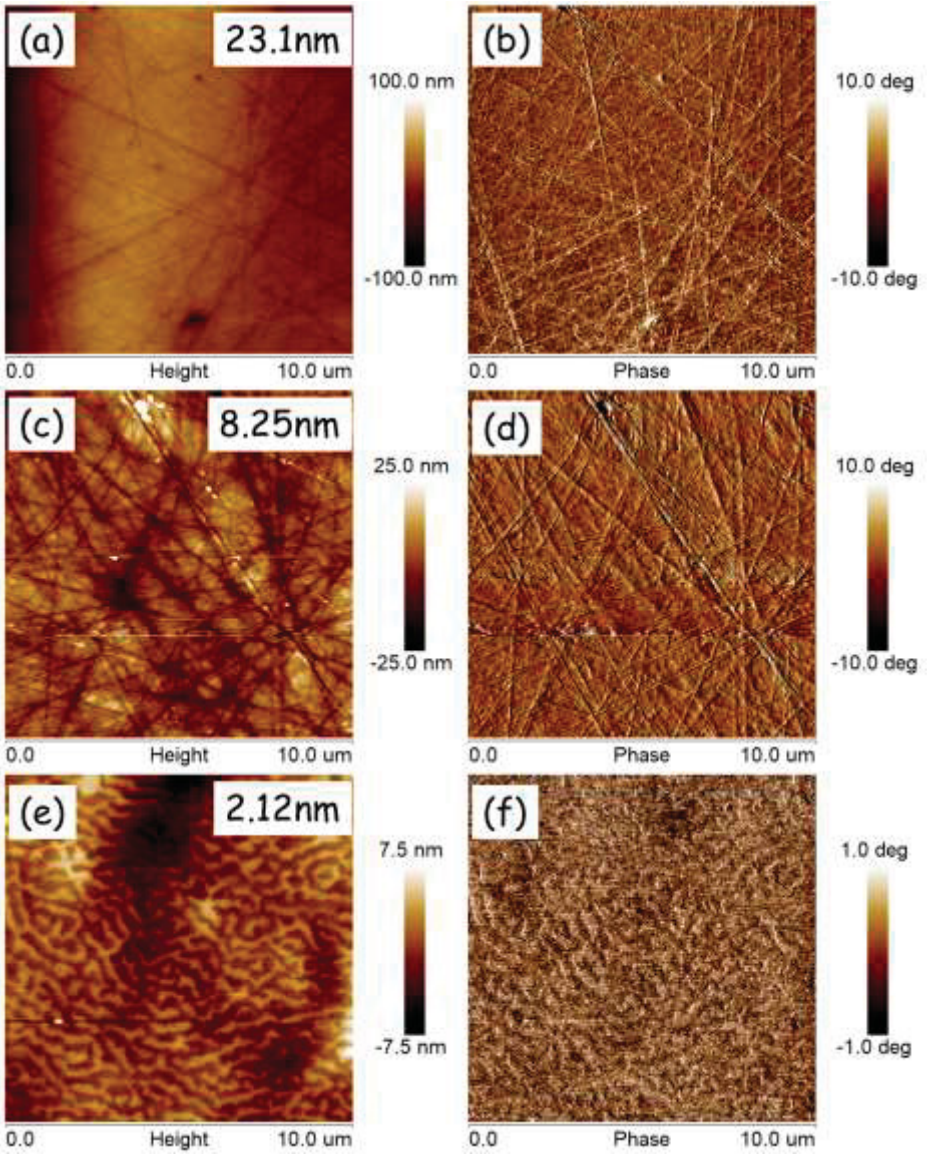

Figure 2.1: AFM height and phase images of a PMN-30PT single crystal substrate after each step of the polishing process. (a) (b) after step 1, (c) (d) after step 2, and (e) (f) after step 4. The surface roughness is listed in (a) (c) and (e).

2.1.2. Pulsed laser deposition

All the thin films described herein were grown using the pulsed laser deposition (PLD) technique. PLD is a type of physical vapor deposition technique that was first used by Smith and

Turner in 1965 for the preparation of semiconductors and dielectric thin films [125]. It has been intensively used for all kinds of oxides, nitrides, carbides, metallic systems, and even polymers and fullerenes [126]. One unique advantage of PLD is the stoichiometry transfer between target and deposited films, which makes it the best way to deposit complex oxides, such as the BFO and PLZT investigated for this study [116,118,119]. Additionally, by identifying optimized deposition parameters, PLD can achieve the literally layer-by-layer growth of thin films, which is very important for fabricating epitaxial thin films on single crystal substrates [126].

Generally, a PLD system includes a high-energy laser (Figure 2.2a), a deposition chamber (Figure 2.2b), and several lenses located between them to direct the focused laser beam onto the targets. The laser source in our group is an excimer laser (LPX305i, Lambda Physik) with KrF radiation. The wavelength of the laser is 248 nm; and the pulse width is around 30 ns. The laser energy and pulsed repetition rate can be set from 45 mJ to 150 mJ and from 1 Hz to 10 Hz, respectively. The deposition chamber is controlled by an ultrahigh vacuum system including both a mechanical pump and a molecular turbo pump. The base vacuum can reach 10^{-6} Torr in hours. Inside the chamber, there are several targets and one substrate holder with the heating system (Figure 2.2c). In addition, a cooling system is used to cool down the laser source and turbo pump.

The working principle of the PLD system is illustrated in Figure 2.2d. During the deposition process, a pulsed and focused laser beam is strikes on the rotated target at an angle of 45 °, the atoms and ions ablated from the target form plasma, and are finally deposited on the heated substrates. Thus, there are three essential physical processes: (a) the ablation process of the target material by laser irradiation, (b) the development of a plasma plume, and (c) the nucleation and growth process of the film on the heated substrates [127-129]. A minimum high temperature is

crucial due to thermal dynamic demands for substrate-thin film interface bonding and crystallization [126,128].

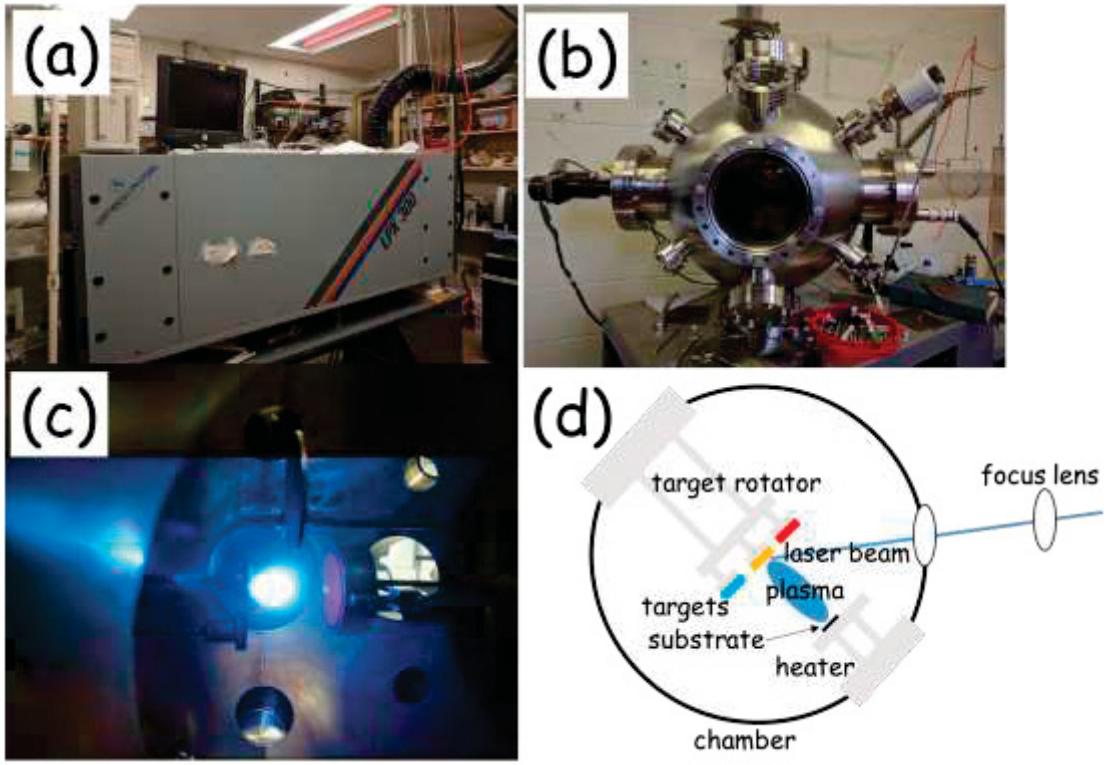

Figure 2.2: Figures of (a) the laser source, (b) the deposition chamber, and (c) a plasma plume ejected from the BFO target. (d) is the configuration of the PLD set-up inside the chamber.

Before the PLD process, the cleaned substrates were attached on the substrate holder with silver paste. The targets were polished using 400-grit, 600-grit, and 1200-grit sandpapers (consecutively), until a mirror-like surface was obtained in order to reduce the formation of large droplets or the tearing-off of target exfoliations [127]. Laser energy and spot size were determined to calculate the exact laser energy density on the target. The target-substrate distance was adjusted so that the plasma plume was tangent with the substrates. Then the chamber was sealed and pumped down to a base vacuum of 10^{-6} Torr by the mechanical pump and turbo pump in turn.

Once the base vacuum was reached, the substrates were heated to the designated temperature, the chamber was filled with an oxygen atmosphere of required pressure. Then, the laser beam with desired energy and pulse repetition was directed to the target, which was rotating during the entire deposition process. By controlling the deposition time and repetition, the thickness of the thin films could be determined. With the appropriate selection of target and substrate materials, as well as suitable deposition parameters, thin films featuring consistent orientations were epitaxially grown on single crystal substrates. After the deposition, the samples were annealed *in-situ* under specific oxygen atmosphere pressure and temperature to (a) relax the residual internal stress, (b) reduce any oxygen vacancies, and (c) improve crystallinity. Finally, the temperature was gradually decreased to room temperature at a rate of 5 °C/min.

2.2. Characterization methods

Once the thin film samples were fabricated, a series of standard tests were conducted to determine epitaxial quality, including checking the surface morphology by atomic force microscope (AFM), examining crystal structure by x-ray diffraction (XRD), and conducting specific property tests in sequence.

2.2.1. Atomic force microscopy

The surface topography of the thin films was analyzed using atomic force microscopy (AFM, Veeco SPI 3100). The surface morphology and smoothness reflects the epitaxy of the thin films on single crystal substrates. Typically, a step-and-terrace surface morphology with a roughness of approximately 1 nm indicates layer-by-layer growth with good epitaxy [130] [131]. The surface morphology is also very important for the self-assembled (1-3)-type nanocomposites

because it provides direct evidence whether the (1-3) structure had formed or not [132]. Therefore, AFM was utilized as a standard first step in determining sample quality.

Figure 2.3 demonstrates the simplified schematic of the AFM configuration. A sharp tiny tip was mounted at the end of the cantilever that was programmed to oscillate up and down near its resonance frequency. The height of the tip (z) responded to the surface smoothness due to the interaction force like Van der Waals forces, dipole-dipole interaction, etc., which can further bend the end of the cantilever up or down. A laser beam was reflected by the end of the cantilever to a sensitive photo-detector, which was able to determine the bend of the cantilever and recorded the height information of the sample's surface. Note that the position of the tip (x, y) was controlled precisely by a piezo-ceramic tube, enabling the sample surface to be mapped with a nanometer-scale resolution [133,134].

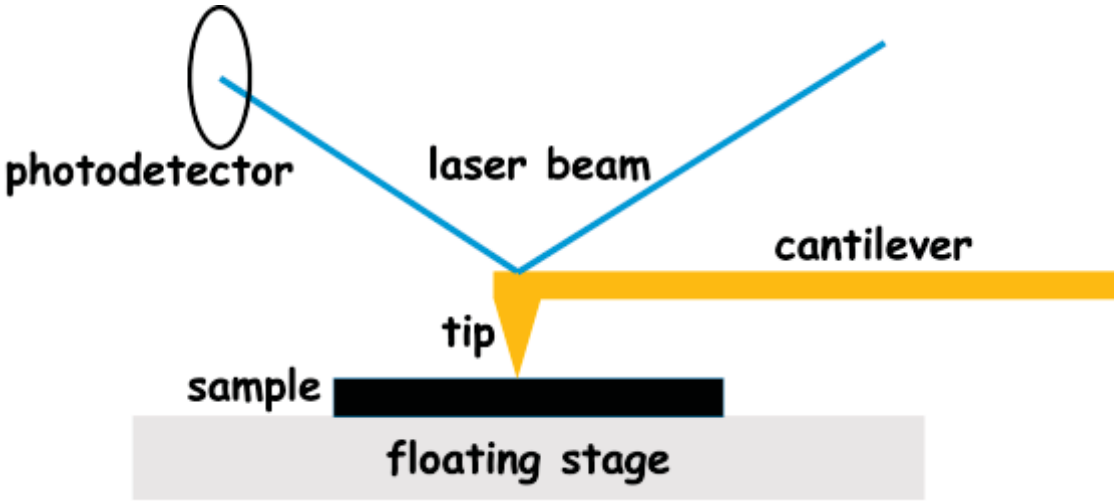

Figure 2.3: Simplified configuration of an AFM system.

By changing the tip type and scanning mode, AFM can be modified to piezoresponse force microscopy (PFM) or magnetic force microscopy (MFM), which are used to detect ferroelectric domain structure or ferromagnetic domain structure, respectively [135]. In this study, PFM or MFM

were employed to image and manipulate the surface ferroelectric/ferromagnetic domain structures of thin film materials, respectively.

PFM works in piezo-response mode [136]. The bottom electrode of the sample is connected to the chuck with silver paste, and a conductive tip is used as the top electrode in the contact mode. When an AC or DC voltage is applied, the piezoelectric sample generates a strain related-piezo-response signal. Thus, for PFM, the tip responds to both the height and piezo-response signals [137]. By using two internal lock-in amplifiers working at two different frequencies, these height and piezo-response signals can be measured and recorded separately [138]. Additionally, a DC voltage applied by the tip in the contact mode can rotate and pole the ferroelectric sample locally, which is of great importance for the study of ME effect in thin film materials [31,40,47,48].

MFM works in an interleave mode—that is, the tip first scans the surface in tapping mode (similar to AFM), then scans the same region in lift mode [139]. By subtracting the topography information, the magnetic signal is recorded in the lift mode. Since the magnetic response from the magnetic material can change the vibrational frequency of the tip, phase mapping in the lift mode reflects the magnetic signal (such as magnetic domain structure) of a magnetic thin film [135,139].

2.2.2. X-ray diffraction technique and reciprocal space mapping

X-ray diffraction (XRD) is the most basic technique for investigating a material's crystal structure, symmetry, and precise lattice parameters. In our group, a Philips X'pert high-resolution XRD system equipped with a two-bounce hybrid monochromator and an open three-circle Eulerian cradle was employed. The analyzer was a Ge (220) cut single crystal providing a 2theta resolution of 0.0068 ° [116]. The x-ray tube worked at 45 kV and 40 mA with a Cu K_α wavelength

of 1.5406 Å. Our system could be tilted (psi or ψ) by ±90 ° and rotated (phi or φ) by 360 ° to obtain the specific crystal orientation of our samples. Also, a heat stage and power supply were available to conduct *in-situ* temperature dependent and E dependent XRD measurements, respectively.

In crystallography, atoms are periodically arranged and form a series of parallel planes separated from one another by a distance (lattice spacing or d). As shown in Figure 2.4, when a monochromatic x-ray beam of wavelength lambda (or λ) is projected onto a crystalline material, at an angle omega (or ω), diffraction occurs only when the distance traveled by the x-ray reflected from successive planes differs by a positive integer number of λ, and can be detected at an angle 2theta (or 2θ). For a symmetric scan, ω is usually equal to θ. By varying the 2θ angle, Bragg's Law conditions can be satisfied by different d-spacing. This 2θ line scan was used in this study to check the orientation and epitaxy of the thin films as well as to calculate the lattice parameters.

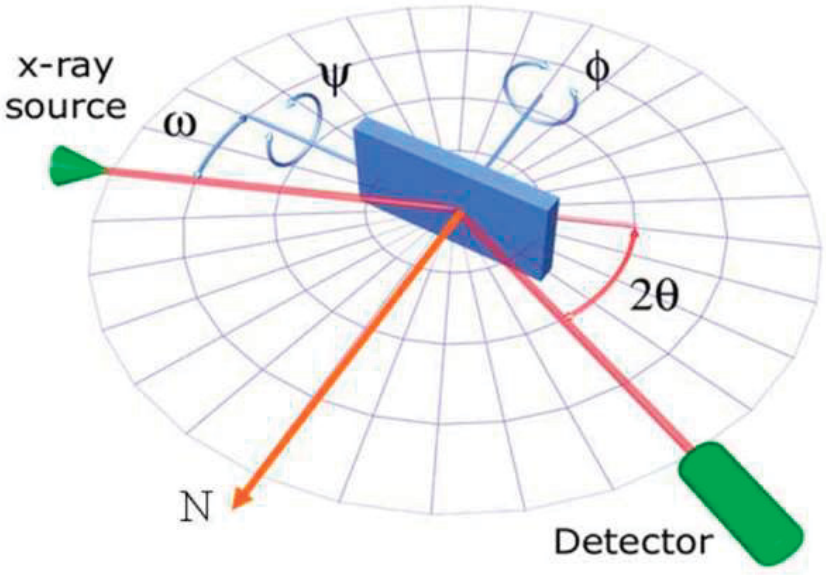

Figure 2.4: Schematic illustration of our XRD system. Different angles like ω, 2θ, ψ, and φ are indexed in the figure [140]. ([130] Yan, L. Two phase magnetoelectric epitaxial composite thin films, Virginia Tech, (2009).) Used under fair use, 2019.

The lattice parameters were calculated using the Bragg's Law as following:

$$n\lambda = 2d \sin\theta, \quad 2.1$$

where n is a positive integer, λ is the x-ray wavelength, θ is the diffraction angle, and d is the lattice spacing that can be used to calculate the exact lattice parameter [141]. For a cubic (or a pseudocubic) system, the relationship between lattice spacing and lattice parameter is given:

$$d = \frac{a}{\sqrt{h^2 + k^2 + l^2}}, \quad 2.2$$

Where a is the lattice parameter of a cubic crystal, and h, k, l are the Miller indices of the Bragg plane.

Another kind of line scan, the ω scan (rocking curve), was used in this study to distinguish multiple equivalent domain variants [15]. It was fixed the 2θ value based on the lattice parameter but rocked about the ω. In this case, one can distinguish multiple sets of planes with the same lattice spacing d that have different tilting angles.

Combining the 2θ line scans with the ω scans, the two dimensional mesh scan was obtained. This approach is known as reciprocal space mapping (RSM), which is a kind of area scan covering a reciprocal space region defined by 2θ and ω. An RSM will contain comprehensive information that may be missed in individual line scans. Thus, in this study, 2θ line scans were used as a second standard test method to determine sample quality, including the epitaxy, crystal structure, and epitaxial strain conditions. If necessary, however, ω line scans and mesh scans were conducted to obtain more detailed crystalline information.

2.2.3. Ferroelectric property measurements

The ferroelectric property measurements obtained in this study can be classified into two categories: the first for single crystal samples, and the second for thin film samples. Both of them

include a polarization hysteresis(P-E) curve measurement. In addition to that, the former also includes temperature dependent dielectric constant measurements; Whereas the latter contains a PFM measurement is detailed in Section 2.2.1.

The P-E curve measurement was based on a modified Sawyer-Tower circuit [142], including signal generator (Tektronix, AFG320), voltage amplifier, oscillography, and reference capacitor. As shown in Figure 2.5, AC voltage signals (in the triangle wave form) were supplied and amplified by the signal generator and amplifier, consecutively, which were then applied to the samples and to the reference capacitor in series. The capacitance of the reference capacitor should be 100 times larger than that of the sample. The voltage signal on the sample, V_{sample}, was monitored via Channel 1 on an oscillograph, while that on the reference capacitor, V_{ref}, was measured via Channel 2. According to Equations 2.3 and 2.4, the capacitance of the sample was calculated by Equation 2.5, and the polarization value was the capacitance normalized by area. Adding the E, which was the sample voltage V_{sample} divided by sample's thickness, the full P-E curves could be plotted.

$$Q_{sample} = Q_{ref} = C_{ref} \times V_{ref} \quad 2.3$$

$$Q_{sample} = C_{sample} \times V_{sample} \quad 2.4$$

$$C_{sample} = \frac{C_{ref} \times V_{ref}}{V_{sample}} \quad 2.5$$

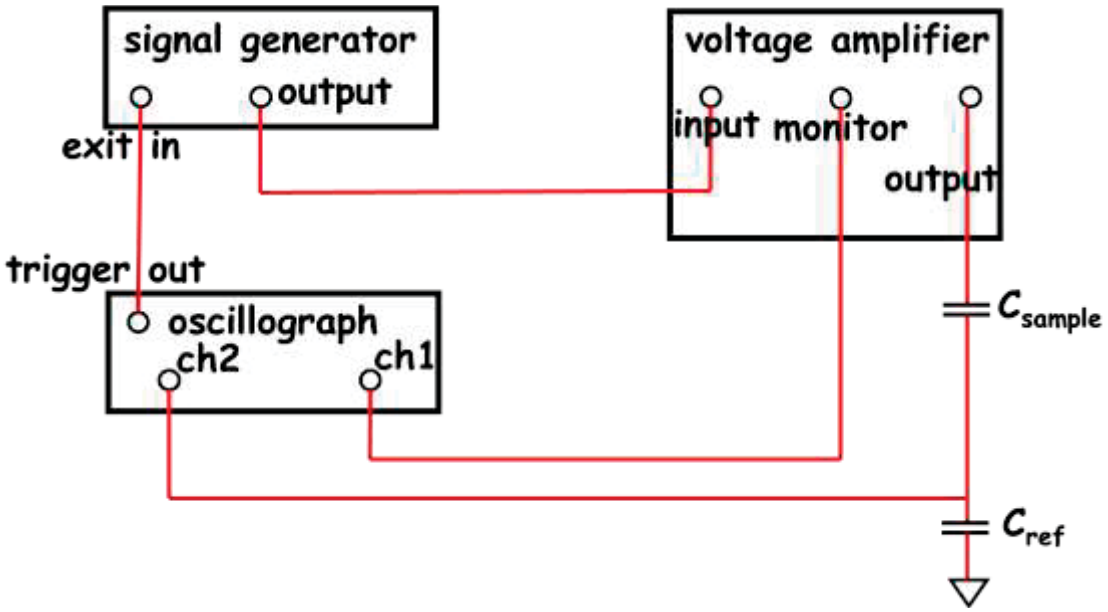

Figure 2.5: Schematic illustration of P-E curve measurement.

For the thin film samples, a probe station was used to apply voltage signals. In contrast, a sensitive clamp was used for the single crystal samples, which in tandem with a linear variable differential transducer driven by a lock-in amplifier (Stanford Research, SR850), was able to measure the strain-E-field (ε-E) curves simultaneously.

The temperature dependent dielectric constant measurements were obtained using a multi-frequency LCR meter (HP 4284A) while the sample was placed inside the oven whose temperature could be precisely controlled with the help of nitrogen flux.

2.2.4. Ferromagnetic property measurements

Room temperature ferromagnetic property measurements were performed using the vibrating sample magnetometer (VSM, Lakeshore 7300). For thin film samples, both the in-plane (IP, the magnetic field was parallel to the surface of thin films) and out-of-plane (OP, the magnetic

field was perpendicular to the surface of thin films) magnetic field dependent magnetization (M-H) loops were measured.

Figure 2.6 shows the basic setup of the VSM. During measurement, the sample was attached on the sample holder and was vibrating perpendicularly to the uniform magnetic field that was generated by the electromagnets [143]. This vibration was controlled by piezoelectric materials and was conducted at certain amplitudes and frequencies. The vibration of magnetic thin films induced a magnetic flux change, which resulted in a voltage signal in the pickup coils. With the help of a lock-in amplifier, the induced voltage was measured precisely, as the vibration frequency served as a reference signal. Since the voltage signal was proportional to the sample's magnetic moment, the resulting M-H curves could be plotted [143].

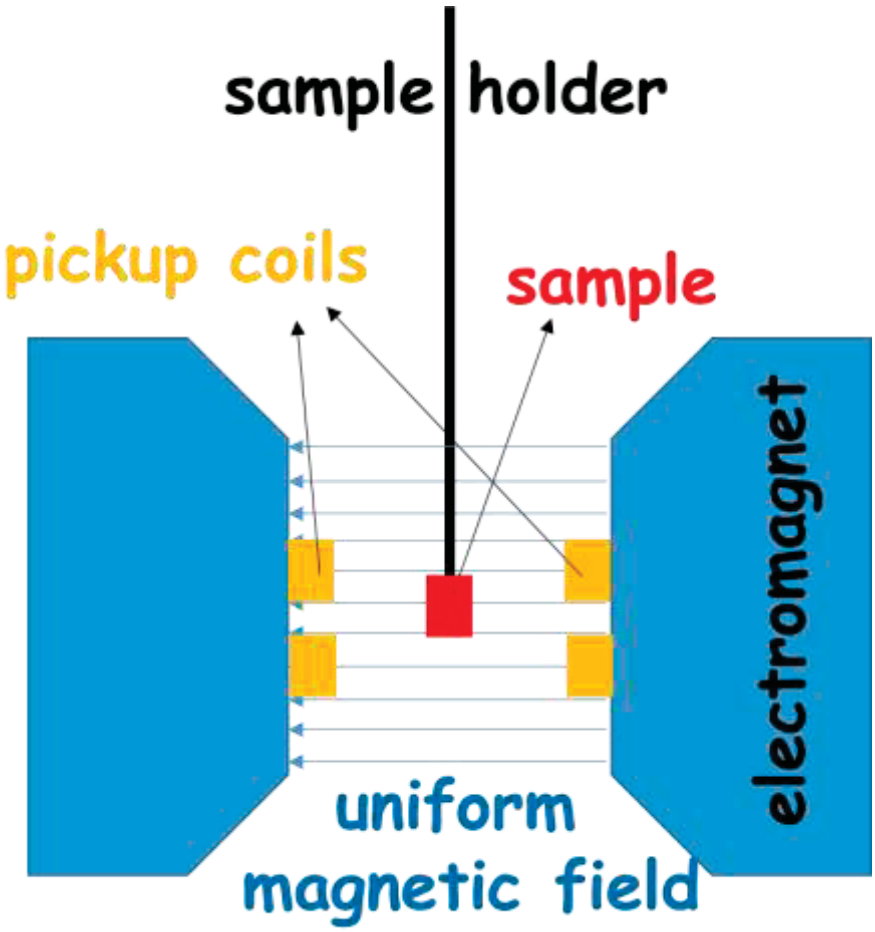

Figure 2.6: Basic setup of the VSM measurement system.

In order to measure magnetic properties at low temperature, we utilized the superconducting quantum interference device (SQUID, Quantum Design MPMS). The SQUID is very sensitive to magnetic flux with a resolution at about 10^{-15} Tesla [144]. It used superconducting loops containing Josephson junction to detect the magnetization of the sample [145]. With the help of liquid helium, SQUID is able to measure M-H loops at very low temperature (i.e., 4K), as well as field cooling curves.

MFM was used to map the surface magnetic domain structure, as described in Section 2.2.1. In order to assess the antiferromagnetic properties of BFO, we used the neutron diffraction technique, which will be introduced in Section 2.2.6.

2.2.5. Scanning electron microscope and transmission electron microscope

A field emission scanning electron microscope (FESEM, LEO 1550, Zeiss) was used to measure the thickness of the thin film samples. Since epitaxial strain is strongly dependent on a film's thickness, it is important to precisely design and control thickness during the deposition process [48,56,57,102]. Thus, the growth rate of one material was always calculated according to the thickness observed from the FESEM and the deposition time and repetition in advance.

The FESEM uses a high-energy beam (5 kV) of electrons to scan the surface of a sample, especially the cross-sectional area for measuring thickness. When the electrons interact with the surface atoms of the sample, signals are generated relating to the electrons emitted from those surface atoms, which contain information about the surface morphology and local elemental ratio [146].

A transmission electron microscope (TEM, JEOL 2100) was used to study the details of the thin film nanocomposites. First, TEM facilitates the acquisition of the exact structure of a nanocomposite by generating bright field/dark field (BF/DF) images. Second, by careful corrections, TEM can even provide atomic-level-resolution images (0.2 nm point-to-point imaging), from which one can observe the crystal lattices and measurement the lattice spacing directly. Third, TEM is able to measure selected area electron diffraction (SAED), which is useful for determining the lattice parameter and crystalline symmetry. Fourth, scanning TEM (STEM)-

based energy-dispersive x-ray spectroscopy (EDS) is capable of mapping elemental distribution within a nanocomposite.

For this investigation, the JEOL 2100 used a beam of high-energy electrons (working at 200 kV) transmitted through ultra-thin specimens, which generated images on a CCD array detector based on the interactions between the electron beam and specimen atoms [146]. Considering that high-energy electrons are also treated as wave-like, rather than particle-like, with a wavelength of a few thousandths of a nanometer, SAED was expected because the spacing between atoms is about a hundred times larger than the electron wave [147]. To obtain high-quality TEM images, an ultrathin specimen was preferred. Thus, precise specimen preparation was vital for this study.

One common process for preparing cross-sectional TEM specimens is hand polishing followed by the ion milling. The sample was firstly cut in half and attached face-to-face by epoxy to protect the thin film material. Then the sample was mounted on a tripod polisher (South Bay Technology, MODEL 590) by Crystalbond. A series of six diamond lapping films (30 μm, 15 μm, 6 μm, 3 μm, 1 μm, 0.5 μm) and a soft cloth were used in turn to mechanically polish the sample on both sides. The thickness of the specimen was measured by a micrometer, which turned out to be about 30 μm. After the specimen was cleaned with acetone and ethanol (separately), it was moved to the ion milling machine (Fischione Model 1010) where it took several hours to get a desired hole. The thickness around the hole would remain only about 100 nm, which was the observation area for TEM imaging. The specimen was transferred to a double-tilt sample holder to access various zone axes during TEM testing. However, in the case of nanocomposites, since it is often desirable to observe the specific region of a nanostructure, this polishing technique could not be used. Instead, a high-resolution SEM assistant focused ion beam (FIB, FEI Helios 600

NanoLab) was used to observe the nanocomposite's surface and conduct the lift-out process to directly get the TEM specimen.

2.2.6. Neutron diffraction

Neutron diffraction is a comprehensive and powerful technique to investigate the atomic and/or magnetic structure of a material. In this study, neutron diffraction was used to measure the magnetic state of the BFO thin films in order to verify whether the spin cycloid state had been broken by the strain or not. The experiments were carried out using the HB-1A triple-axis-spectrometer (FIE-TAX) at the High Flux Isotope Reactor (HFIR) at Oak Ridge National Lab (ORNL), and BT-4 thermal triple-axis instrument at the Center for Neutron Research, National Institute of Standard Technology (NIST).

Both instruments were operated using fixed incident energy of 14.6 meV (equivalent wavelength λ of 2.36 Å. HB-1A employs a double pyrolitic graphite (PG) monochromator system with PG filters mounted after each monochromator to significantly reduce the higher order contaminations of the incident beam. Collimations of 40'-20'-sample-20'-80', and 40'-40'-sample-40'-80' downstream from the reactor to the detector were used for the HB-1A experiment. For the experiment at BT-4, PG filters were placed both before and after the samples, and collimations of 40'-S-40' were used. The first monochromator unit is flat, while the second one is vertically focused. A highly-oriented pyrolytic graphite filter is mounted after each monochromator to reduce λ/2 contamination [148]. This setup provides a very clean beam nearly free of higher-order contamination neutrons. Thus, it is able to detect the small magnetic signals from thin film materials. Studies have been done by both HB-1A and BT-4 on the spin cycloid state of BFO thin films, separately [149,150]. In this study, OP E was applied during neutron diffraction measurements.

Chapter 3. Electric field controlled phase transition in $BiFeO_3$ thin films on PMN-PT single crystal substrates

This section describes the fabrication of $BiFeO_3$ (BFO) thin films by PLD on PMN-30PT single crystal substrates in both the IP and OP modes (see Figure 3.1), by which either IP or OP E was allowed to apply on PMN-30PT. E-modulated strain changes/phase transformations were observed and analyzed by high-resolution XRD. E-induced antiferromagnetic state changes were also observed by neutron diffraction spectroscopy.

3.1. Fabrication of the BFO/PMN-30PT heterostructures in both IP and OP modes

The IP and OP modes both have advantages. The IP mode does not require an inset conductive buffer layer to facilitate electrical contact, which makes the fabrication process simpler than the OP mode. The lack of an inset layer also ensures that less strain imposed on the BFO by the substrate is relaxed. On the other hand, the OP mode requires a much lower voltage to realize the same E, because the substrate's thickness is generally much smaller than the dimensions of the other two directions, being more energy-efficient than the IP mode. Furthermore, with the help of photolithography, the OP mode will allow application of local E distribution using diverse electrode patterns. Therefore, from an applications perspective, the OP mode is the more practical approach [116].

A schematic illustration of both modes of BFO/PMN-30PT heterostructures are shown in Figure 3.1. For the IP mode, BFO thin films were directly deposited on single crystal (001) PMN-30PT substrates. The BFO thickness was set at 50 nm, offering an epitaxial strain that was close to the magnetic state transition boundary predicted in the magnetic phase diagram of BFO [51]. For the OP mode, an additional 6 nm $SrRuO_3$ (SRO) buffer layer was deposited between the BFO layer and the substrate. The laser energy density (LED) during the deposition of the SRO layer was fixed

at 1.5 J/cm^2, whereas during the deposition of the BFO layer, the LED was varied from 1 J/cm^2 to 3 J/cm^2 by tuning the laser beam energy. The deposition time was adjusted to keep the thickness of the BFO layer constant using different LEDs. In order to prevent Bi evaporation, the deposition temperature was maintained at 650 °C. The oxygen partial pressure was fixed at 90 mTorr for the deposition of BFO and at 150 mTorr for SRO. After deposition, the as-deposited thin films were *in-situ* annealed in a pure oxygen atmosphere of 100 Torr at 650 °C for 30 min and then cooled to room temperature at a cooling rate of 5 °C/min. Gold electrodes were sputtered on top of the OP mode heterostructures. Silver electrodes were placed on the bottom and sides using silver paste.

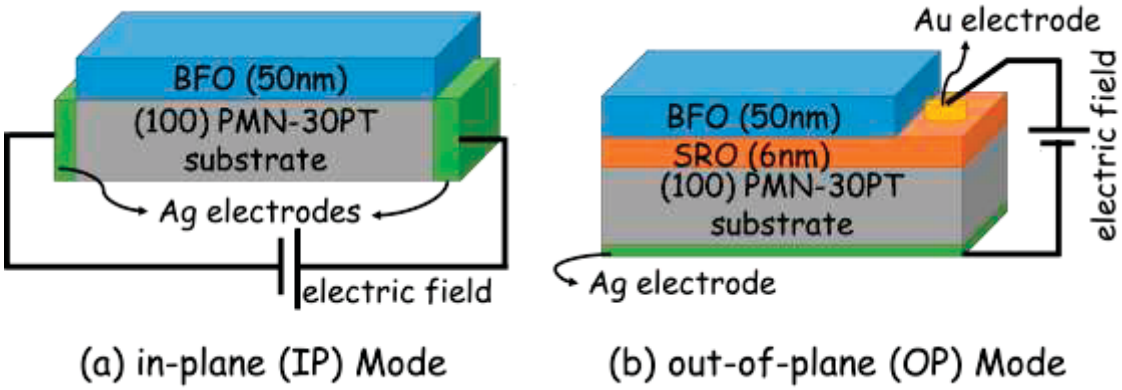

Figure 3.1: Schematic illustration of BFO/PMN-30PT heterostructures whose structures allow application of either IP or OP E. (a) the IP mode, and (b) the OP mode.

3.2. Characteristics of (001) PMN-30PT single crystal substrates

The PMN-30PT substrates in this study were provided by the Shanghai Institute of Ceramics, China. The hand polishing process was necessary for achieving a smooth surface for deposition. Before polishing, the temperature dependent dielectric constants and P-E/ε-E curves were measured to characterize its quality. The T_C value in Figure 3.2a was about 139 °C, which ensured the correct composition [8]. The P-E and ε-E curves (Figure 3.2b) confirmed the FE volatile

nature of PMN-30PT [151]. After polishing, the crystalline quality was checked by XRD 2θ line scans, where only the (00l) peaks could be observed. The surface morphology was measured by AFM. The mosaic surface with a roughness of 1.7 nm was obtained.

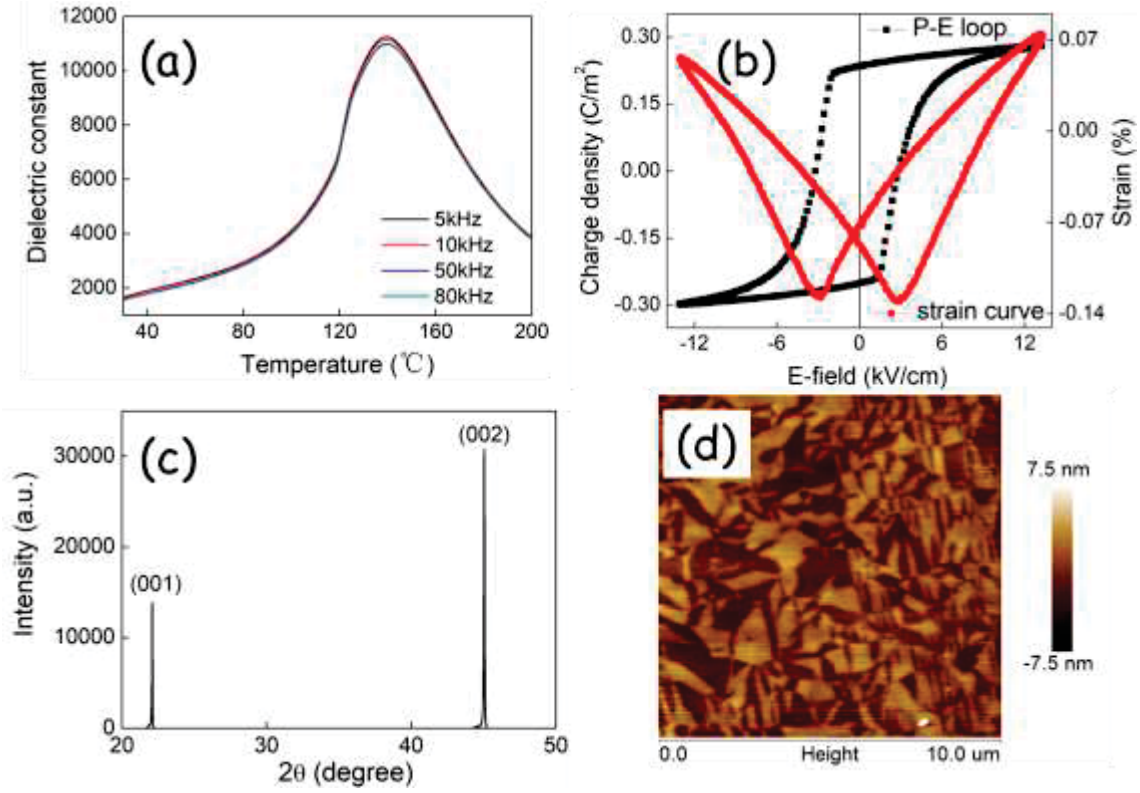

Figure 3.2: (a) Temperature dependent dielectric constant, (b) P-E/ε-E curves, (c) XRD 2θ line scan, and (d) AFM height image of the (001) PMN-30PT single crystal substrates.

3.3. Laser energy density effect on BFO thin films' quality

Although the lattice mismatch with the substrates is the primary factor determining internal strain in BFO, subtle differences in deposition conditions can influence the final strain as well. Amongst these factors, laser energy density (LED) is an important parameter. However, the scholarly literature from different research groups has reported a wide range of LEDs for BFO between 1 J/cm^2 and 3 J/cm^2 (e.g., 1 J/cm^2 [57,62], 2 J/cm^2 [152], 2.5 J/cm^2 [40,153], 2.6 J/cm^2 [154], and 3

J/cm^2 [56]). Thus, the effect of LED was first studied in order to optimize the strain state of the heterostructures.

The AFM height images of the BFO thin films in the both modes are shown in Figure 3.3. In the OP mode, the BFO thin film deposited at 1 J/cm^2 had a roughness of 1.9 nm (Fig. 3.3a), which was similar to that of the polished PMN-30PT substrate. The gentle ridges were caused by the corresponding domain structures on polished PMN-30PT. The BFO thin film deposited at 3 J/cm^2, on the other hand, had a higher surface roughness of 5.8 nm. There were also some square particles found on the surface, which might result from larger pieces of the target material being ablated by the higher LED [155]. Note that AFM provides images of only surface morphology, and it is reasonable to suspect that such particles might exist inside the entire film which would impair its density. A similar morphology was observed for the IP mode BFO/PMN-30PT sample, where, under 3 J/cm^2, BFO displayed more impurity particles on the surface. However, when prepared under an LED of 1 J/cm^2, IP mode BFO featured a higher roughness of 7.9 nm due to its maze-like morphology, which is usually seen for BFO/$SrTiO_3$ heterostructures and indicates better epitaxy [131]. Thus, based on surface morphology studies, one can infer that a lower LED results in higher BFO thin film quality.

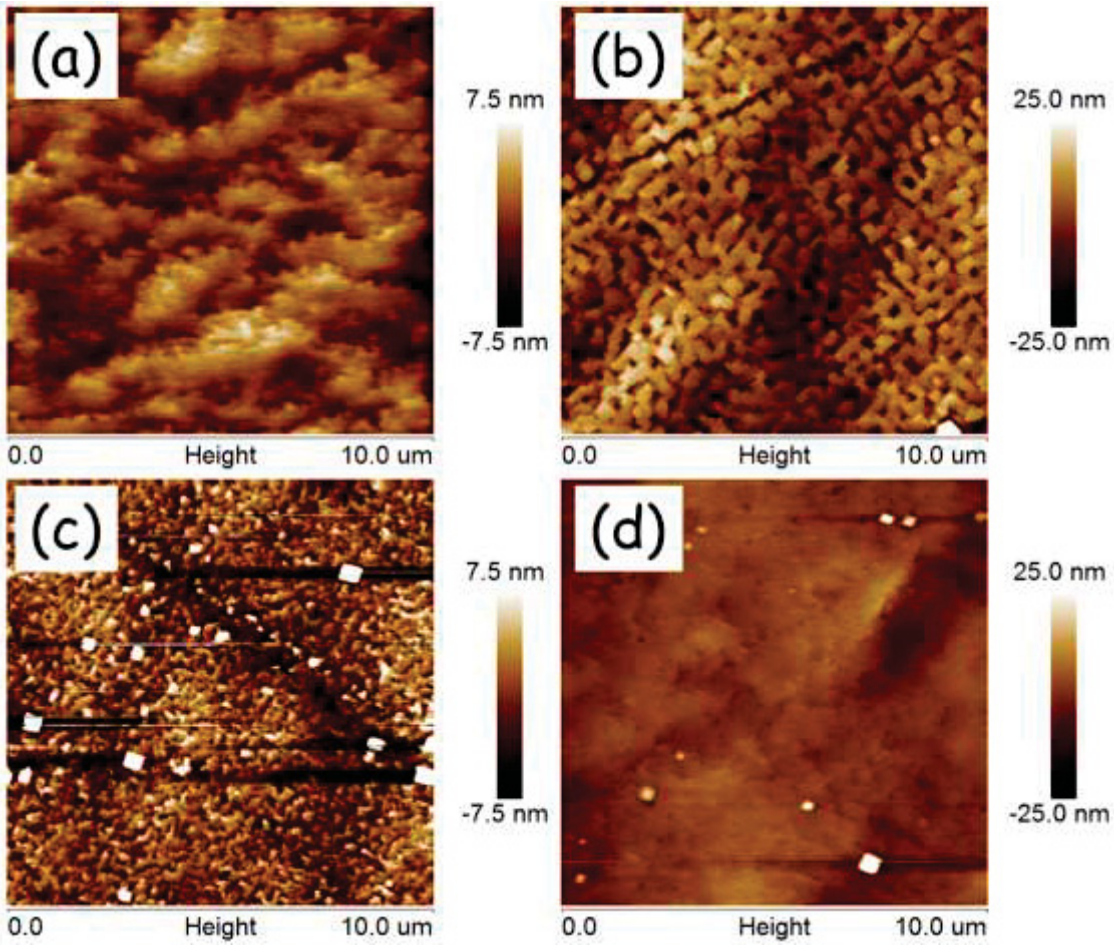

Figure 3.3: AFM height images of (a) (b) BFO(50)/SRO(6)/(100) PMN-30PT, and (c) (d) BFO(50)/(100) PMN-30PT. The LEDs for BFO was 1 J/cm^2 for (a), (c), and 3 J/cm^2 for (b), (d).

For the OP mode of BFO thin films, the ferroelectric P-E loops were measured, and the results supported this assumption. As shown in Figure 3.4a, the BFO prepared at 1 J/cm^2 exhibited normal ferroelectric loops with a saturation polarization of 70 μC/cm^2. In contrast, the BFO prepared at 3 J/cm^2 had a rounded loop indicating current leakage. PFM was also measured for the 1 J/cm^2 BFO thin film in the OP mode, as shown in Figure 3.4b. The clear box-in-box phase images confirmed the ferroelectric nature of the BFO thin film.

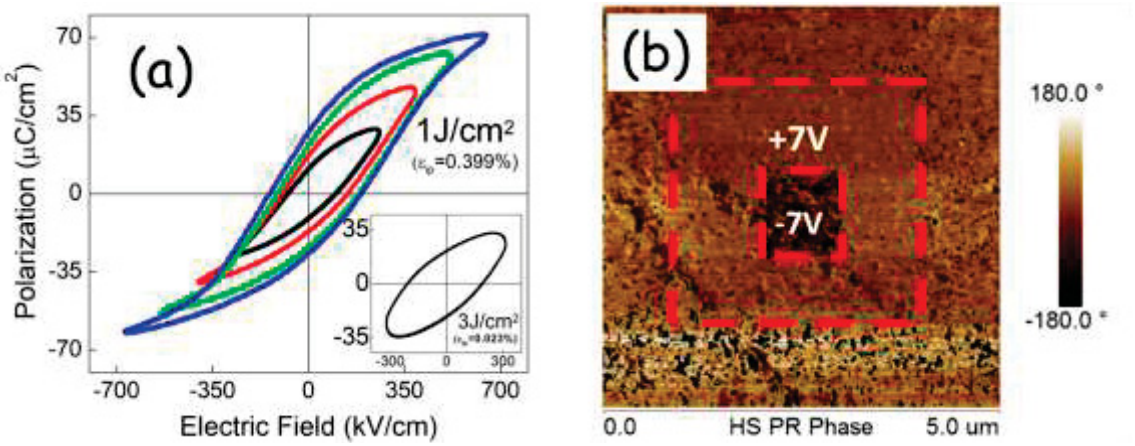

Figure 3.4: (a) Ferroelectric P-E loops for the BFO(50)/SRO(30)/(100) PMN-30PT heterostructure prepared using a LED of 1 J/cm^2. The insert shows corresponding measurement for a BFO deposited at 3 J/cm^2. (b) PFM phase image of the BFO(50)/SRO(30)/(100) PMN-30PT sample. The red squares indicate regions poled by a ±7 V tip bias.

Figure 3.5 shows the corresponding XRD patterns of BFO films on (001) PMN-30PT substrates, in IP and OP modes. A Gaussian Function was used to fit the peaks and the lattice parameters were calculated based on Equation 2.1. The strain states were calculated by the following equations:

$$\varepsilon_{op} = (c_{real} - c_{BFO})/c_{BFO} \times 100\%, \quad 3.1$$

$$\varepsilon_{ip} = [(\nu - 1) \times \varepsilon_{op}]/2\nu, \quad 3.2$$

Where c_{real} is the lattice parameter along the OP direction of BFO calculated from the XRD patterns, c_{BFO}=3.965 Å is the bulk BFO's lattice parameter [57], and υ=0.49 is Poisson's ratio of BFO [156,157]. A positive sign indicates a tensile strain, whereas a negative sign indicates compression.

In both modes, the peaks of BFO layers deposited at 1 J/cm^2 were located at higher angles, compared to those deposited at 3 J/cm^2. The calculated IP strains of BFO in the OP mode decreased

from 0.4% for 1 J/cm^2 to 0.02% for 3 J/cm^2, indicating a significant relaxation of BFO's strain in the latter condition, which may be due to the square particles observed in the AFM images [155]. The calculated IP strain of BFO in the IP mode was initially 0.55% for 1 J/cm^2, which was slightly larger compared to corresponding data for the OP mode. This confirms that more strain is imposed on BFO thin films from the PMN-PT substrates than from the SRO buffer layers. As the LED decreased, the IP strain was reduced and even became compressive at 3 J/cm^2. Combining the AFM, P-E, and XRD data, it can be concluded that a lower LED favors better BFO thin films with larger IP strain. However, it should also be pointed out that PLD can be sensitive to subtle changes in deposition conditions, which can result in significant variations in film quality. Thus, all the BFO thin films discussed herein were prepared at 1 J/cm^2.

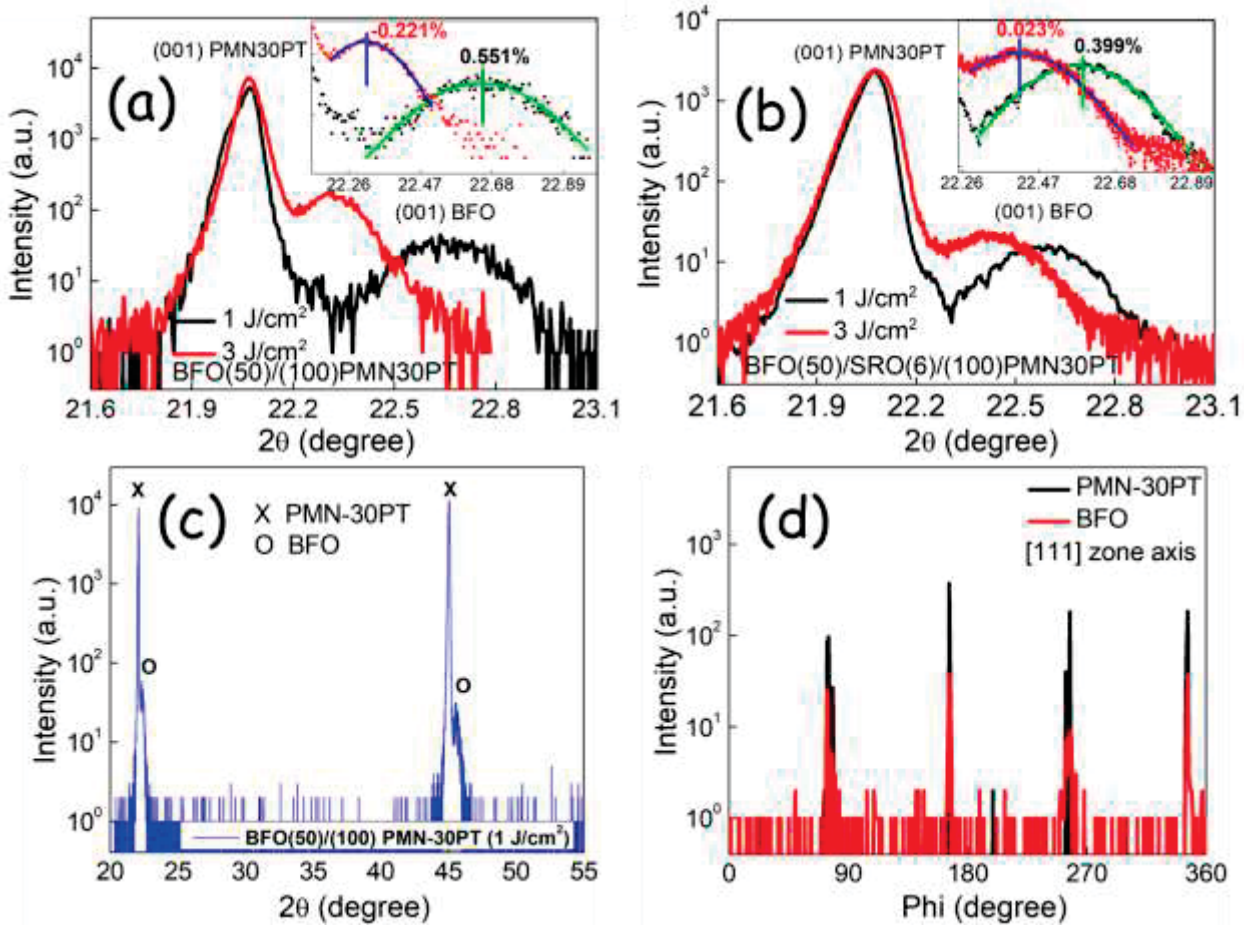

Figure 3.5: (a) (b) XRD patterns of (a) IP mode BFO(50)/(100) PMN-30PT and (b) OP mode BFO(50)/SRO(6)/(100) PMN-30PT. The blue and green curves in the insets of (a) and (b) are the Gaussian Fit results that located the position of the peaks. The corresponding IP strains of BFO are also provided in the insets. (c) Full XRD 2θ line scan that showed pure BFO peaks beside the PMN-PT's. (d) 360° φ scan that confirmed the BFO thin film had the same four-fold symmetry as the PMN-PT substrate.

3.4. E-controlled strain changes and structural phase transformation

Next, E was applied to the PMN-30PT substrates, and the change in strain on the BFO in both modes was calculated and studied. As the dimensions of the PMN-30PT substrate were 5 mm

× 2.5 mm × 1 mm, the maximum voltages applied were 1250 V and 1000 V in the IP and OP modes, respectively. These levels facilitated the maximum E of 5 kV/cm and 10 kV/cm, respectively. Since the maximum voltage is limited by the dielectric strength of PMN-30PT, the OP mode can sustain a significantly larger E compared to the IP mode, because it is much easier to reduce the thickness of PMN-PTs.

As shown in Figure 3.6, the BFO layers had butterfly-like strain curves for both modes, whose trends were opposite to the lattice parameter changes in the PMN-30PT substrate. Considering that BFO's IP strain is tensile, the trends for BFO are consistent with that of the PMN-30PT in the OP direction. Since the piezoelectric constant of PMN-30PT is positive, as the E-field was increased in the IP mode from 0 to +5 kV/cm (-5 kV/cm), the lattice parameter of PMN-30PT decreased by 0.002 Å and the IP strain of BFO increased from 0.55% to 0.57% (0.60%). In the OP mode, when E was increased from 0 to +10 kV/cm (-10 kV/cm), the lattice parameter of PMN-30PT increased by 0.006 Å (0.010 Å), which was about 0.24% in strain and was consistent with the ε-E curve in Fig. 3.2b. The IP strain of BFO decreased from 0.41% to 0.33% (0.35%). The opposite trends between the two modes can be attribute to the orthogonal direction of the applied E. Additionally, the coercive field of PMN-30PT was about 3 kV/cm in the OP mode, which was similar to that of the substrate without a BFO layer (see Fig. 3.2b). However, from the shape of the strain curve for BFO in the IP mode, it was hard to distinguish the coercive field, whereas those for the OP mode were more obvious. This difference may be due to the OP E being more uniform in comparison to the IP ones, as the interfaces between PMN-30PT and the electrodes had been polished for the OP mode.

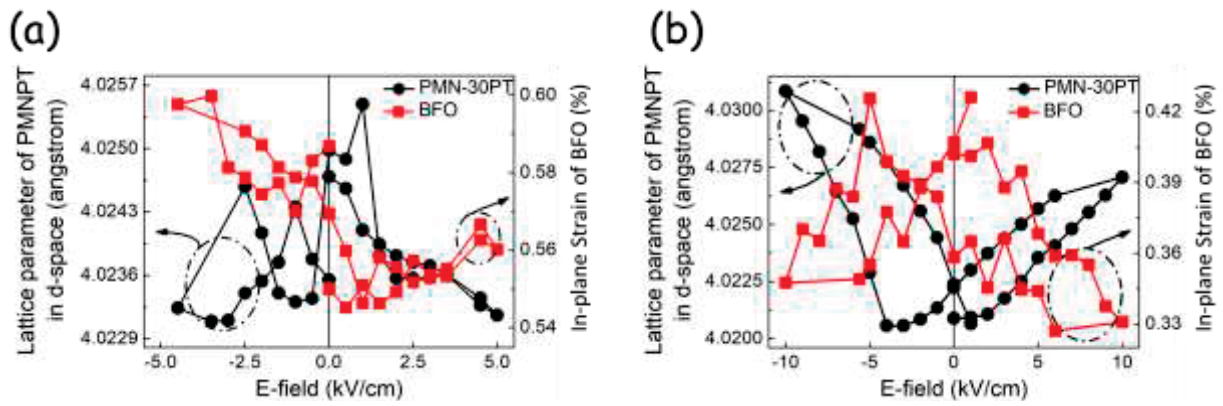

Figure 3.6: Lattice parameters of PMN-30PT in the OP direction and IP strain of BFO vs E curves. (a) IP mode, and (b) OP mode.

Figure 3.7 shows RSM images taken around the [011] zone axes of BFO/PMN-30PT heterostructures in both modes, which reveal a structural transformation under E=3 kV/cm. As mentioned in Section 1.3, the composition of PMN-30PT was near the MPB between the R and T phases, where intermediate monoclinic phases have been observed as structural "bridges" [68,70,158]. A small E can alter the phase transformation sequence to being either $R \rightarrow M_A \rightarrow M_C \rightarrow T$ or $R \rightarrow M_A \rightarrow T$, where the M_A phase remains stable after E is removed [69,70]. In this study, the PMN-30PT substrates exhibited a M_A phase structure on removal of E. As shown in Fig. 1.5a, the M_A unit cell (space group Cm) has a unique b_{MA} axis along the [110] direction with respect to the pseudocubic cell, and due to a tilt angle of the c_{MA} axis, b_{MA} and a_{MA} are not equivalent [70]. Accordingly, as indicated in Fig. 3.7, the (011) peaks of PMN-30PT were split into a doublet, reflecting b_{MA} and a_{MA} (i.e., b* and a* domains, respectively). The formation of domains lowers the energy of a system by relaxing parts of the elastic energy, which is the reason why M_A remains stable on removal of E instead of reverting to R [15]. Similarly, a peak split of BFO existed along the [011] zone in the IP modes. However, in the OP mode, due to the SRO buffer layer releasing

part of the elastic energy, such doublet splits were notably less obvious, indicating that BFO in the OP mode may be R rather than M_A [15,157].

Furthermore, in the IP mode, the dominant domain state of PMN-30PT was switched from a* (or b*) to b* (or a*) by application of 3 kV/cm. The BFO domain structure was also simultaneously changed. In contrast, in the OP mode, the a* and b* domains remained unchanged. We attribute this to the fact that, in the OP mode, E was applied along the c axis, which would stretch the axis along the OP direction and compress them biaxially in the IP direction. On the other hand, in the IP mode, E was applied along either the b or a axis, making it the preferred dominant domain state. In addition, the splitting along Qx in the peak of PMN-PT was caused by the less uniform IP E. The RSM images in Fig. 3.7 demonstrate a promising way for controlling structural transformations in BFO via the application of IP E-fields.

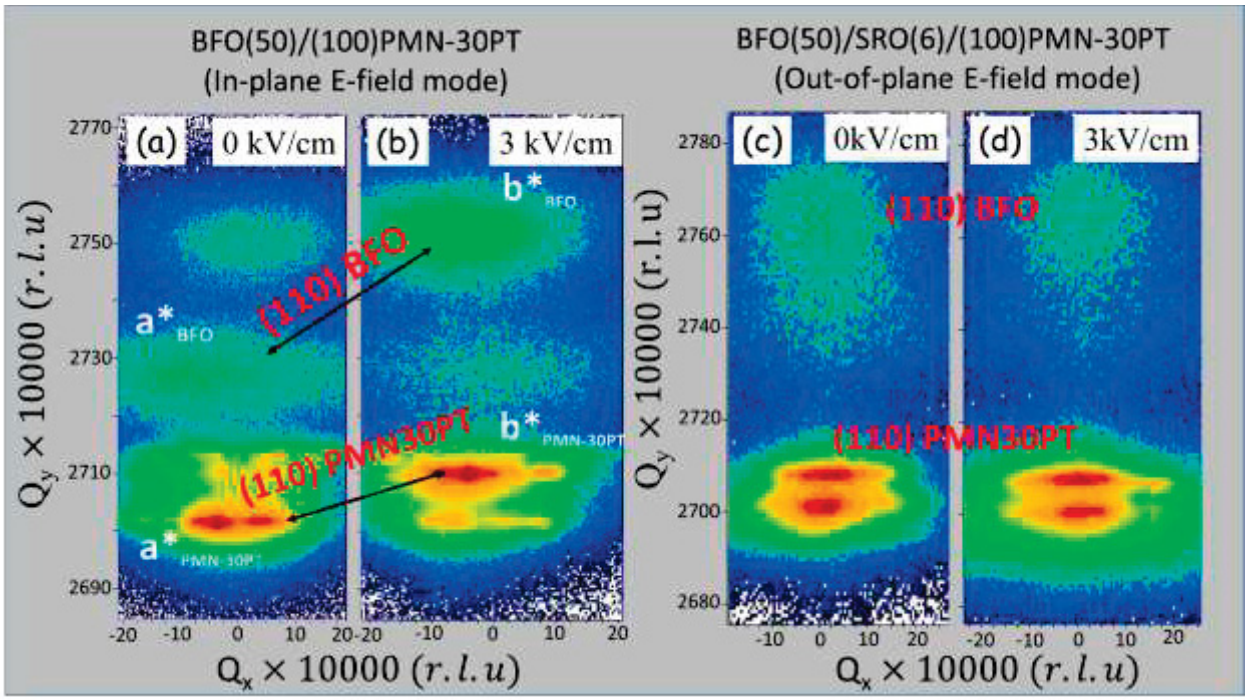

Figure 3.7: The (011) oriented RSM images for (a) (b) the IP mode of BFO(50)/(100) PMN-30PT, and (c) (d) the OP mode BFO(50)/SRO(6)/(100) PMN-30PT. (a) (c) under 0 kV/cm E, and (b) (d) under 3 kV/cm E. The arrows in (a) and (b) point out the switching of the dominant domain structures (a and b*) of PMN-30PT and BFO. The contour lines in this figure are given on a logarithmic scale.*

3.5. Strain-mediated E-controlled manipulation of the antiferromagnetic state

For epitaxial thin films of BFO, strain engineering has been shown to be effective in tailoring the antiferromagnetic characteristics, and thus the related physical properties [51,159-161]. For example, by selecting different substrates to impose suitable epitaxial strain, the cycloidal modulation can be modified [51,55,162]. In the above section, we demonstrated the feasibility of controlling the strain changes in BFO thin films epitaxially deposited on a piezoelectric PMN-30PT single crystal substrate by E. This approach offers the possibility of adjusting the spin state stability of epitaxial BFO films via E. In other words, E applied to the substrates might tune the

strain states of BFO films, and consequently adjust the antiferromagnetic properties. Yet, direct observations of antiferromagnetic changes induced by E in BFO have not yet been reported.

Neutron diffraction is a proven powerful technique for studying antiferromagnetic states, even for thin films of BFO [149,150,162]. When measured from the HHL zone, the ordered Fe^{3+} ions in BFO contribute to the neutron signal near the (0.5 0.5 0.5) reflection [54,150,163]. For a collinear G-type antiferromagnetic state, a single peak is expected due to the elastic scattering of neutrons from a magnetically ordered lattice [150,164]. If the antiferromagnetic structure is a cycloid as observed in bulk BFO, multiple peaks will appear, from which the propagation direction and period can be calculated [149,150,165]. In this section, we report an *in-situ* neutron diffraction study investigating the antiferromagnetic state changes in BFO films under E applied to the PMN-PT substrates.

3.5.1. Experimental details

To gain sufficient neutron scattering counts, 200-nm-thick thin films of BFO were deposited on (001)-oriented PMN-30PT (surface area of 10×10 mm^2). The deposition parameters were identical to those described in Section 3.1. To apply E along the OP direction, a 30-nm-thick SRO buffer layer was deposited between the BFO layer and the substrate by PLD as the top electrode, whereas a 100-nm-thick Palladium layer was sputtered on the back of the PMN-PT as the bottom electrode. Two BFO/SRO/PMN-30PT heterostructures were fabricated, labeled as Sample #1 and Sample #2.

To investigate the antiferromagnetic state of BFO, neutron diffraction measurements were then performed on two BFO films (Sample #1 and Sample #2). Studies were conducted around the (HHL) scattering plane, accessing the (0.5 0.5 0.5) reflections. Due to beamtime limitations, the two heterostructures were measured at different facilities. Sample #1 was measured using the HB-1A triple-axis spectroscopy located at the High Flux Isotope Reactor (HFIR) at Oak Ridge

National Laboratory (ORNL), and Sample #2 was measured on the BT-4 thermal triple-axis instrument at the Center for Neutron Research, National Institute of Standard Technology (NIST). Due to the fact that the lattice parameters of BFO and PMN-PT tend to be very close to each other, the nuclear peak of BFO film appeared at the tail of that from the PMN-PT substrate. The intensity of the nuclear peak from the PMN-PT substrate was much stronger than those from BFO film, making it difficult to index the BFO peak accurately. Therefore, the samples were aligned using the PMN-PT substrate as a reference and all results are given in units of the PMN-PT's lattice parameter.

3.5.2. Crystal structure and induced strain

The quality of the epitaxial BFO films was characterized by full XRD 2theta scans, as shown in Figures 3.8a and 3.8b. Only (00L) peaks for BFO films were found, in addition to the corresponding peaks for the PMN-PT substrates. The results demonstrate good epitaxy without any notable second phases. The insets show the AFM height images of the films. The surface roughness was about 1.8 nm for Sample #1, and 4.3 nm for Sample #2.

Enlarged XRD patterns in Figures 3.8c and 3.8d confirm that the peaks of both the PMN-PT and BFO shifted to lower angles under applied E. This trend demonstrates that with E applied along the OP direction of PMN-PT, the lattice elongates along that direction and compresses along the IP directions, consistent with previous reports [57,116,166,167]. This compression is transferred to the BFO layer through the interface, inducing a strain change along its IP. On removal of E, the peaks shifted back towards higher angles, demonstrating that the IP strain is reversible for BFO.

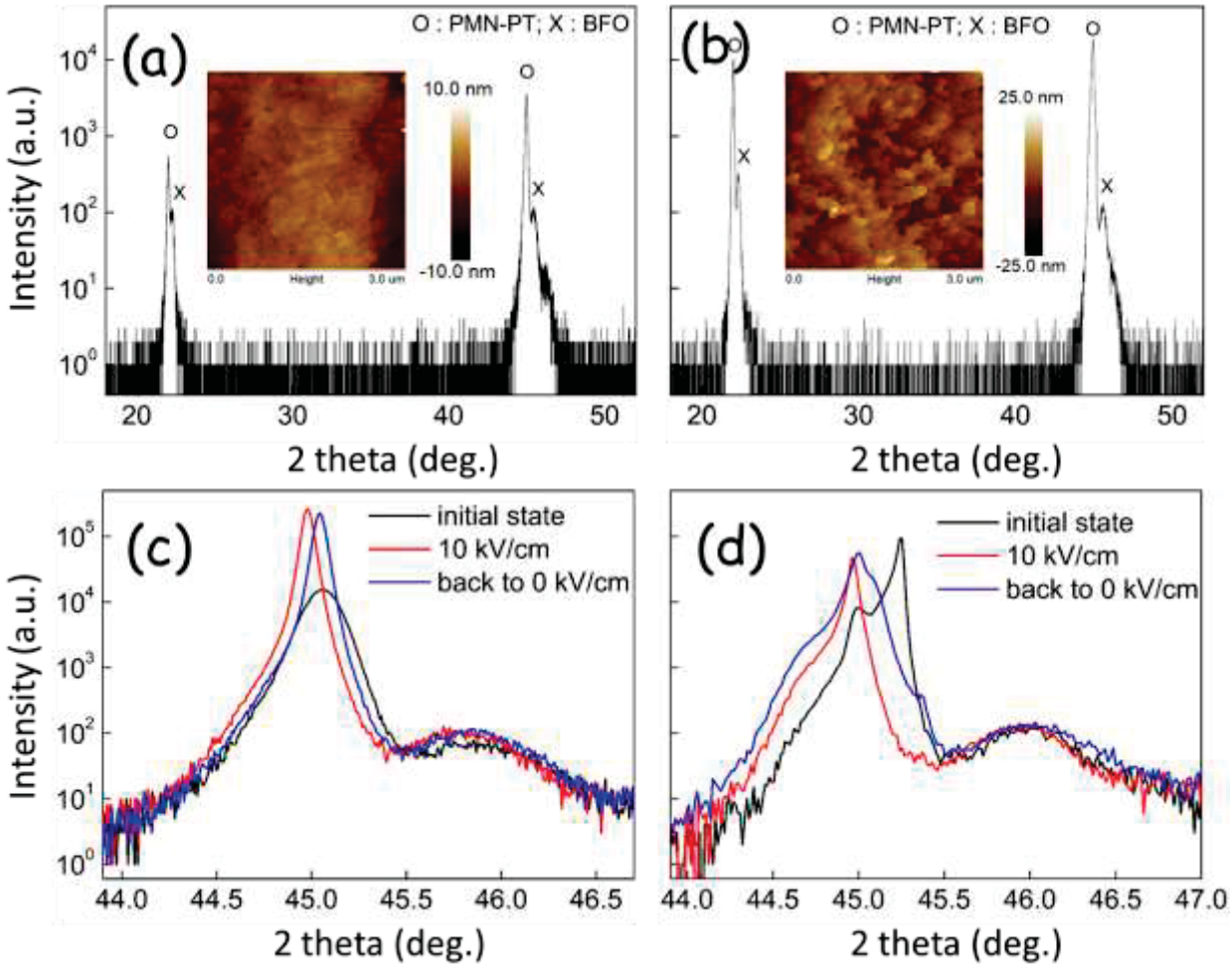

Figure 3.8: XRD patterns of (a) (c) Sample #1, and (b) (d) Sample #2. (a) (b) Full 2theta scans. (c) (d) (002) peaks under 0 and 10 kV/cm E-fields. The insets in (a) and (b) are the AFM height images of the BFO films.

Careful examination of the XRD patterns indicates differences in the peaks of the different PMN-PT substrates. Sample #1 exhibited a single peak indicative of a stable rhombohedral (R) phase for the PMN-PT substrate; in contrast, Sample #2 showed multiple PMN-PT peaks, indicative of phase transitions under E. In the initial state, the doublet peak of PMN-PT indicated a tetragonal (T) phase, which changed to a R phase under E=10 kV/cm. On removal of E, it mainly remained in the R phase, although a small volume fraction of the T phase was evidenced by the

shoulder peaks in Figure 1d. Such differences in the PMN-PT structure may be caused by compositional fluctuations during crystal growth, which in particular may be very sensitive for PMN-30PT due to it is proximity to the morphotropic phase boundary (MPB) [62,168]. In our case, differences in the PMN-PT substrate enriched the possible strain conditions of BFO films.

Figure 3.9 shows the lattice parameter changes for PMN-PT and IP strain changes for BFO as a function of E. The butterfly-like curves evidence that the strain of BFO can be reversibly changed by E for both samples. Despite the fact that the PMN-PT substrate of the two heterostructures had different phase transition sequences and hysteresis with electrical history, the IP strain change of the BFO films had a similar trend, except for the magnitude of strain values. For 0<E<10 kV/cm, the IP strain change in the BFO layer was from 0.14% to 0.06% (Sample #1) and from 0.33% to 0.22% (Sample #2).

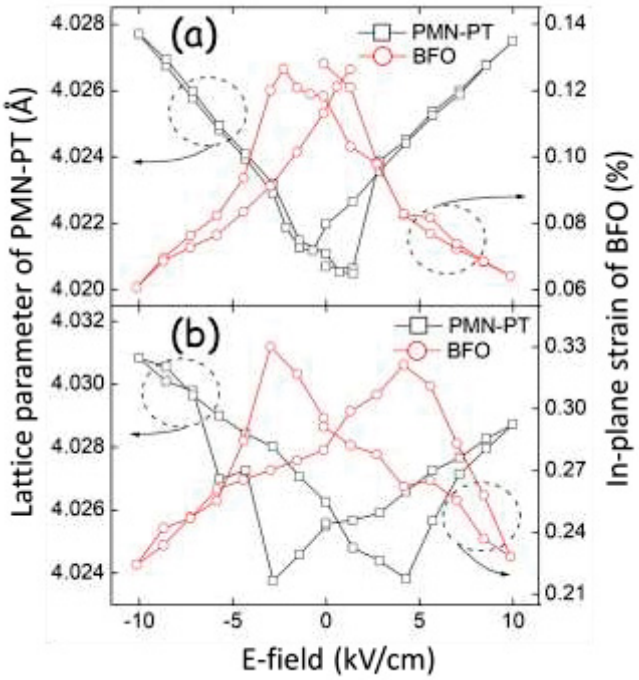

Figure 3.9: Lattice parameter of PMN-PT and IP strain of BFO as a function of applied E-fields. (a) Sample #1, and (b) Sample #2.

3.5.3. Neutron diffraction studies

Figure 3.10 shows neutron diffraction mesh scans for Sample #1 taken around the (0.5 0.5 0.5) reflection in the (HHL) scattering zone. As can be seen in Figure 3.10a, initially for E=0 kV/cm, the BFO film exhibited only a single reflection peak, which suggests a collinear G-type antiferromagnetic state [150,169]. When E was increased to 4 kV/cm (Figure 3.10b), two reflections were found, with a spacing of 0.0050(5) reciprocal lattice units (r.l.u.), indicative of a corresponding spin modulation period of 651 Å. An enlargement of the cycloid period with respect to that of bulk materials may be induced by the epitaxial tensile strain [51,149]. Note that the propagation vector of this cycloidal modulation is along the [110] direction, which is unlike that along the $[1\bar{1}0]$ direction for bulk BFO [53,54,170] and for BFO films under a compressive IP strain [149]. This observation is consistent with previous predictions based on Landau-Ginzburg theory, where in order to minimize the free energy, the spin modulation propagated along the [110] direction when the BFO film was subjected to a proper tensile IP strain [51].

On removal of E (Figure 3.10c), the doublet peaks remerged together, indicating that the BFO film returned to the collinear G-type antiferromagnetic state. However, due to the hysteresis in the ε-E response of the PMN-PT substrate, the IP strain of BFO was only partially recovered, which resulted in a modified antiferromagnetic configuration with a notably larger cycloid period of 1126 Å. Furthermore, as shown in Figure 3.10d, when E was increased to 9 kV/cm, the BFO thin film appeared to exhibit two reflection peaks, which indicated a $[11\bar{2}]$ propagation vector, rather than the [110] one. The data demonstrate that epitaxial IP strain can gradually tailor the propagation direction and the period of spin modulation.

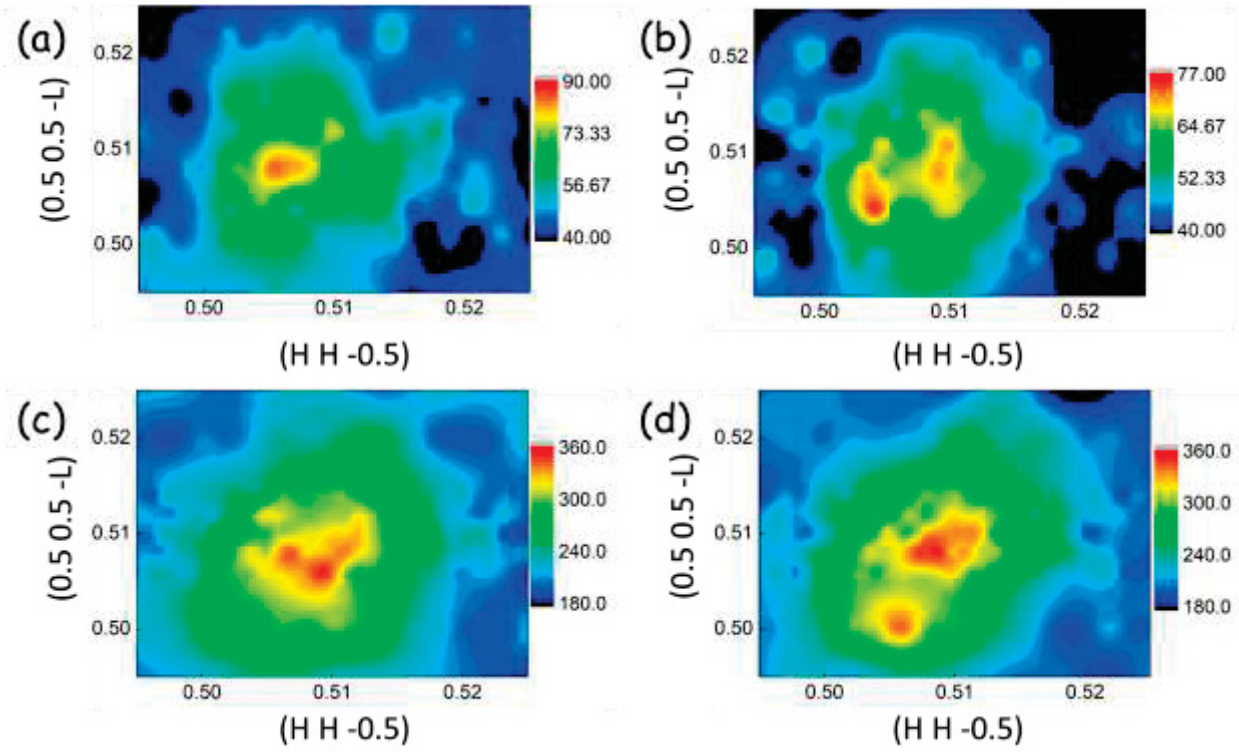

Figure 3.10: Neutron diffraction mesh scans of Sample #1 taken in HH-L zone. (a) initial state (0 kV/cm), (b) under an E of 4 kV/cm, (c) on removal of E, and (d) under an E of 9 kV/cm.

Next, we investigated the neutron results for Sample #2 whose BFO layer had a larger IP strain. As shown in Figure 3.11, Sample #2 did not exhibit any peak splitting around (0.5 0.5 0.5) under various E. We checked the lattice parameter of PMN-PT using its (111) nuclear peak, which indeed changed under E. This observation indicates that E was successfully applied onto the substrate during the neutron diffraction measurements. Additionally, the (0.5 0.5 0.5) peak of BFO had slightly shifted under E to the left side, showing that its IP strain condition was altered by E. The constant single peak evidences that for E≤10 kV/cm, Sample #2 exhibited a stable collinear G-type antiferromagnetic state, which may be attributed to the sufficient strain from the T phase of PMN-PT.

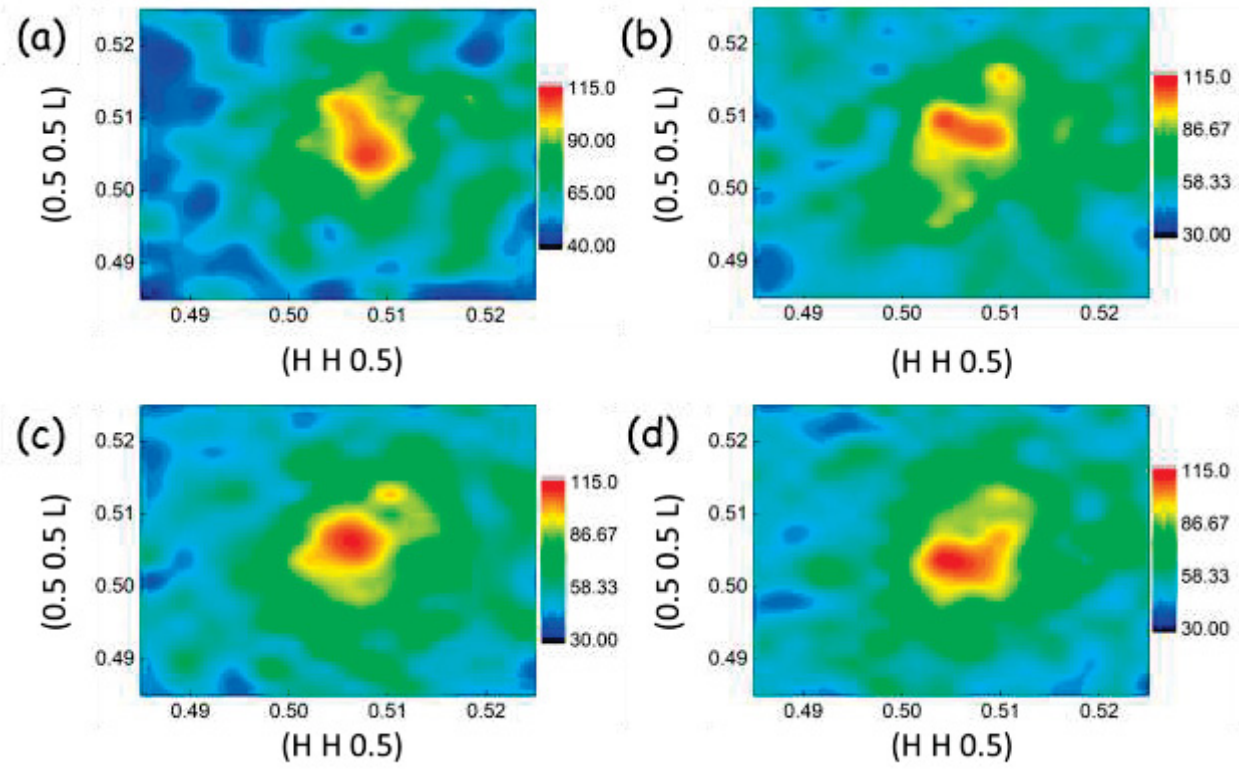

Figure 3.11: Neutron diffraction mesh scans of Sample #2 taken in HHL zone. (a) initial state (0 kV/cm), (b)-(d) under an E of 4 kV/cm, 6 kV/cm, and 10 kV/cm, respectively.

3.5.4. Discussion

We summarize our observations in the antiferromagnetic state diagram for BFO films as a function of IP tensile strain, as shown in Figure 3.12. Different antiferromagnetic states are distinguished based on their cycloidal structure and propagation vectors. Please note that due to the limitation of the measurement step size, the boundaries in the figure are estimates.

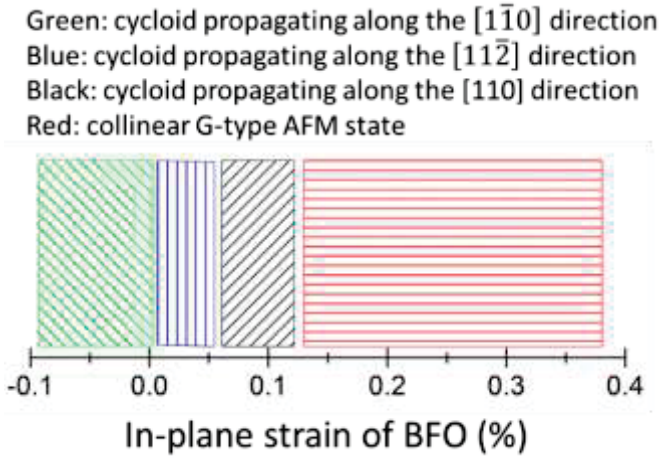

Figure 3.12: Antiferromagnetic state diagram of the BFO thin films as a function of the IP tensile strains.

According to the literature ,when the IP strain was zero, a cycloidal spin structure that propagates along the $[1\bar{1}0]$ direction should be stable, similar to bulk BFO [51,149]. The propagation vector should then change to being along the $[11\bar{2}]$ and [110] directions in turn with increasing IP tensile strain [51], during which the period of the cycloid should gradually enlarge. Finally, the cycloidal should be destroyed when the IP strain is sufficiently large, resulting in a collinear G-type antiferromagnetic state. Our results are consistent with these prior reports, where the IP strain was controlled by E applied to the PMN-PT substrate.

Cycloid propagation along the $[11\bar{2}]$ has never been reported for bulk BFO. However, it has been reported for 1-μm-thick BFO films on (110)-oriented $SrTiO_3$ (STO) substrates with a modest epitaxial strain [150]. For Sample #1 under E=9 kV/cm, a small epitaxial strain of ~ 0.07% may similarly result in a propagation vector change from $[1\bar{1}0]$ to $[11\bar{2}]$. A number of reports of BFO on STO with thicknesses between 200 nm and 800 nm (i.e., slightly larger epitaxial strains) have confirmed a propagation vector along the $[1\bar{1}0]$ [51,149,162]. Similarly, our results for Sample #1 under E=4 kV/cm showed a propagation vector along the [110]. We also noted that on subsequent

removal of E=9 kV/cm, the $[11\bar{2}]$ propagation vector reversed to [110]. Thus, the cycloid state with the $[11\bar{2}]$ propagation vector could be induced by a properly small magnitude of either the compressive or tensile strain, which then changed back to being along the <110> directions when the epitaxial strain increased.

In comparing the results between Samples #1 and #2, we confirmed that the initial strain condition determines the initial antiferromagnetic state of BFO thin films, which in turn plays an important role in the further tunability of the antiferromagnetic state with E. If the initial strain was large, the antiferromagnetic state was in the collinear G-type antiferromagnetic region, which remained stable on application of E. Clearly, the PMN-PT substrate is an important factor, as different crystal structures can significantly alter the strain condition of deposited BFO films. We note that the film thickness, buffer layers, as well as other deposition parameters, can also contribute to the initial strain state of the films.

The strain required for our sample (~0.15% for #1) to break the cycloid and stabilize the collinear AFM state was notably smaller than the theoretical predicted value of 0.5% [51]. This difference may reflect a strain gradient within the BFO film. The interface region of the film may experience a notably larger IP tensile strain (~1.5% according to the lattice mismatch between BFO and PMN-PT), which subsequently relaxes near the surface region. It is quite possible that the BFO film has multiple stable antiferromagnetic states throughout its thickness. Our XRD and neutron diffraction data only provide information about the average structure [150]. The neutron diffraction data for Sample #2 show an apparent collinear G-type antiferromagnetic phase, but cycloidal structures may exist within the average structure that was detected. One could reduce film thickness to obtain a more uniform BFO layer with a single stable antiferromagnetic state, however there is a trade-off, as the neutron signal needs volume to be detectable.

3.6. Summary

In summary, BFO/PMN-30PT heterostructures in both IP and OP modes were fabricated by PLD. The LED effect on BFO's intrinsic strain was investigated by AFM and XRD analyses. Electric fields were then applied on the piezoelectric PMN-30PT substrates to induce reversible strains. RSM scans along the (011) zone axis revealed that a M_A phase was induced in both PMN-PT and BFO, where the dominant domain state could be switched between biaxial directions by E in the IP mode.

In the OP mode, neutron diffraction was used to investigate the apparent antiferromagnetic states of 200-nm-thick BFO thin films deposited on piezoelectric PMN-PT substrates. By choosing suitable thin film conditions (deposition parameters, composition of PMN-PT, and film thickness), the initial antiferromagnetic state of BFO (e.g., the cycloidal propagation vector and period, etc.) could be altered, which was further adjusted by applying E to the PMN-PT substrate. The tunability with E was partially reversible on removal of E, reflecting the hysteresis of PMN-PT. These results illustrate the feasibility of controlling the antiferromagnetic states of BFO thin films by external E. Such capability may be applicable to the development of advanced sensors, magnetic memory devices, and spintronics. An antiferromagnetic state diagram for the BFO thin films under IP tensile strains was also constructed, based upon strain conditions of the film.

Chapter 4. Apparent phase stability and domain distribution of PMN-PT single crystals with nanograted electrodes

As demonstrated in the prior section, piezoelectric PMN-30PT single crystals can help tune the strain state, phase transformation process, and even the magnetic state of BFO thin films by E. The efficiency of this tunability is strongly related to the piezoelectric capacity of PMN-30PT. Our cooperators, Xiaoning Jiang's group at North Carolina State University (NCSU), reported a ~30% enhancement in the piezoelectric properties of PMN-30PT single crystal with nanograted electrodes, which they attributed to doping/diffusion with Mn and E fringe effects [77]. However, the domain distribution near the surface region and how it is influenced by non-uniform E remains unclear. In this section, a high-resolution XRD RSM technique was used to monitor *in-situ* changes in the apparent phase stability and domain distribution in the near-surface region under E.

4.1. Fabrication of nanograted electrodes on PMN-PT single crystals, experimental setup, and simulation method

Detailed fabrication information can be found in ref. 76 and 170 [77,171]. For this phase of the investigation, [001]-grown PMN-30PT single crystals with electrodes on the (001) plane were prepared by the CTS Corporation. The crystals were polished to desired thicknesses of 200 μm and 600 μm. Lloy's mirror interference lithography (LIL) was used to fabricate nanograted electrode patterns on one side (marked as the front side) of the crystal, parallel to the [100] direction. The grating size was equal to the distance between grates, set as either 500 nm or 1000 nm. A regular planar electrode was deposited on the opposite side (marked as the back side). For the front side, a 100-nm-thick layer of manganese was deposited by heat evaporation, followed by an annealing process (800 ℃, 3 hours, in air) to form semiconductive MnOx electrodes, while letting Mn diffuse into the PMN-PT surface regions. After the photoresist was removed, 100-nm-

thick Au layers were deposited by electron-beam evaporation, with a 5-nm-thick Ti protective layer on the entire front and back sides of the PMN-PT crystals. To clarify the discussion, crystals with different configurations are summarized in Table 4.1.

#	1	2	3	4
Thickness	200 μm	200 μm	600 μm	200 μm
Grating size	1000 nm	500 nm	1000 nm	Planar Au electrodes on both side

Table 4.1: Configurations of different PMN-PT crystals numbered as #1 to #4.

After electrode deposition, copper wires were attached by silver epoxy so that an E could be applied. The crystals were then studied using our XRD system under various E levels from 0 to 10 kV/cm, applied *in-situ* by a DC power supply. Both XRD line scans and RSM mesh scans were measured along the [002] and [022] zone axes (the index in this chapter was in a pseudocubic system), after fine calibrations were performed. Both the front and back sides of the crystals were measured, and the lattice parameters were calculated from the 2θ values of the XRD line scans, according to Equation 2.1. The units in RSM images were normalized using the lattice parameters. Assuming the initial strain of each crystal to be zero, the strain conditions under various applied E were also obtained based on the lattice parameters calculated above.

It must be noted that, the reason the [022] zone axis was chosen, instead of the [200] or [220] as customary in single crystal studies, was because our crystals were too thin to accommodate scans along these zones. The [022] mesh contains information about the [020] zone (equivalent to the [200] due to symmetry) and the [002] one. Considering that the peak along the [002] zone exhibited only a single peak along the (00L) direction, the splitting of the (022) peak along the (0LL) direction represents the peak-splitting pattern for the (0L0)/(H00) zone, from

which one can distinguish the structure. Accordingly, the mesh scan patterns for M_A and R along the [022] zone are illustrated in Figure 4.1.

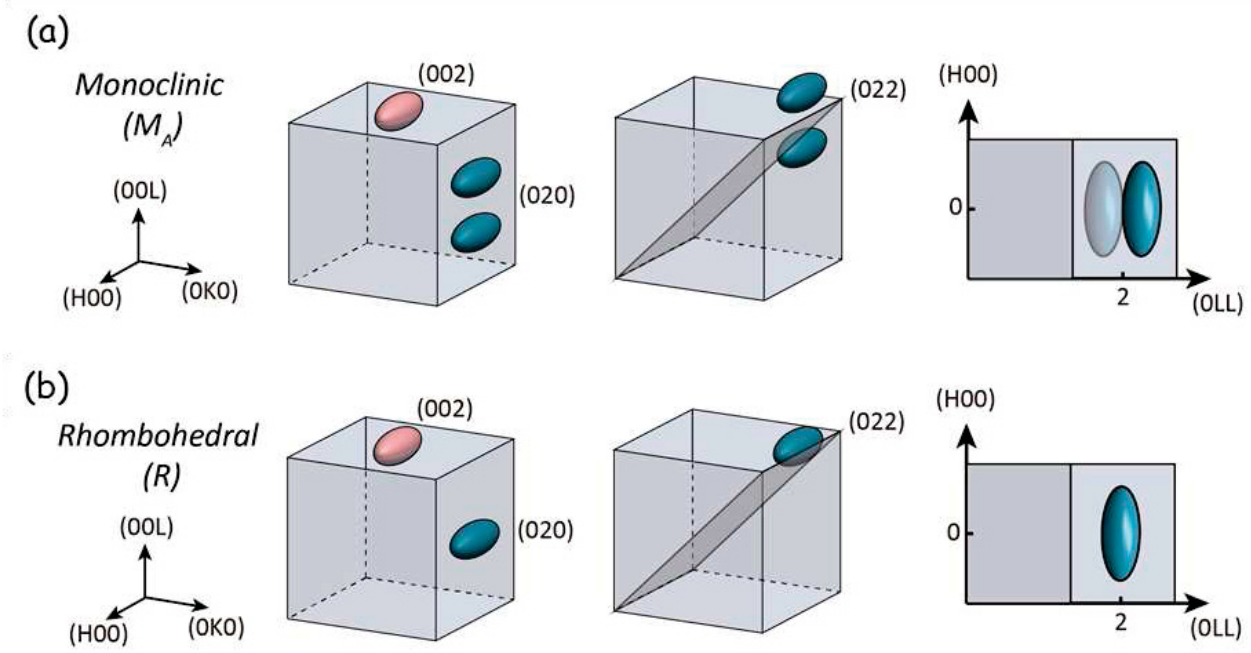

Figure 4.1: Illustration demonstrates how the M_A (or R) domain distributions along the (020) and (002) zones contribute to shaping the doublet (or single) domain along the (022) zone, which exhibits a doublet (single) peak when projected into the (HLL) plane. The ellipse broadening domains in (d) and (e) are caused by the nanograted electrodes.

The dielectric constant was measured from 0.1 kHz to 10 kHz by a precision impedance analyzer (Agilent, 4294A). The samples were poled under $0 \leq E \leq 10$ kV/cm in advance. After each test, the crystals were annealed at 250 °C for 2 hours to return them to their initial state.

Simulations of the electric field distribution beneath the nanograted electrodes were also performed using COMSOL multiplhysics finite-element analysis. The finite-element model was composited of a PMN-PT crystal and periodical MnO_x electrodes. The width and thickness of the MnO_x were 1000 nm and 100 nm, respectively, and the thickness of the PMN-PT was 100 μm. In

the electrical boundary condition, the bottom conductive electrode was assigned as the ground condition and the electric field of 2 kV/cm was applied across the PMN-PT crystal. The simulation was performed in two-steps. (1) A dielectric constant of 4000 was assigned to the whole crystal and an electric field distribution was obtained by numerical simulation. (2) According to simulation results from Step (1) and the dielectric measurement, a dielectric constant of 7000 was assigned to the edges of the electrodes (black circle parts) and the simulation was performed again. The increased dielectric-constant effect made the non-uniform electric field generated by the fringe effect stronger.

4.2. Experimental results

Figure 4.2 provides RSM scans taken from the Crystal #4 with conventional planar electrodes. The single (002) peak of PMN-PT became sharper along both longitudinal (00L) and transverse (H00) directions with increasing E, and remained sharp even upon removal of E. The doublet (022) peak under E indicated the phase transition from R to M_A, which also remained after poling. Our RSM results of PMN-PT with planar electrodes are consistent with other reports.

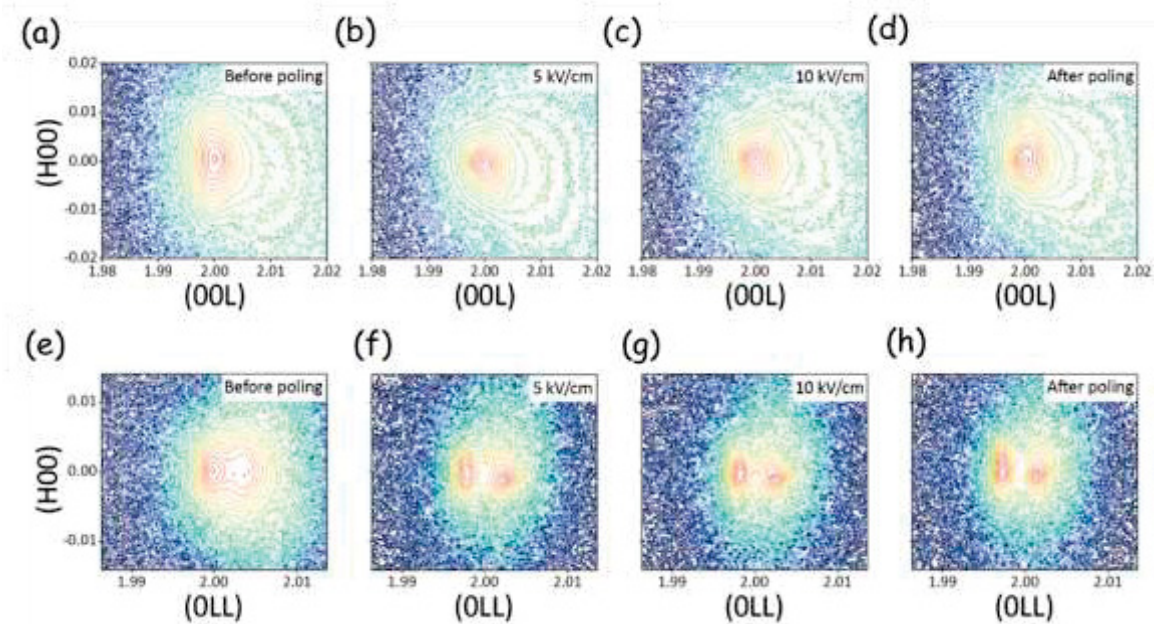

Figure 4.2: RSM scans of Crystal #4 (T=200 μm, conventional planar electrodes). (a)-(d) along the [002] zone axis, (e)-(h) along the [022] zone axis. (a) (e) 0 kV/cm (before poling), (b) (f) 5 kV/cm, (c) (g) 10 kV/cm, and (d) (h) back to 0 kV/cm (after poling).

Figure 4.3a-d provides RSM scans taken from the front side of Crystal #1 with nanograted electrodes. Line scans (ω scans) along the transverse extracted from the RSM are given in Figure 4.3e-i. As shown in Fig. 4.3a, the (002) peak corresponds to the initial unpoled condition, where the line scan (Fig. 4.3e) revealed a single sharp peak. Under application of 2 kV/cm, this peak became sharper along the (00L) direction (2θ scan), but broader along the (H00). The corresponding line scan in Fig. 4.3f revealed multiple peaks along the (H00) direction. With increasing E to 10 kV/cm, the peak became narrower along the longitudinal (00L), but much broader along the transverse (H00). In fact, line scans along the (H00) direction revealed numerous peaks, which are different from that associated with PMN-30PT with conventional planar electrodes (Fig. 4.2). For the nanograted crystals, once E was removed, these unique changes in the RSM and line scans were retained, exhibiting a multitude of transverse peaks (see Fig. 4.3d

and Fig. 4.3i). Comparison of these data to the schematic in Fig. 1.5b-d will demonstrate that the crystal with nanograted electrodes exhibits peak splitting unlike the single peak of either M_A or R (which has a single peak tilted from the pseudocubic by α_R). Our results demonstrate numerous peaks with a wide distribution of tilt angles, which were not distinctly split from each other.

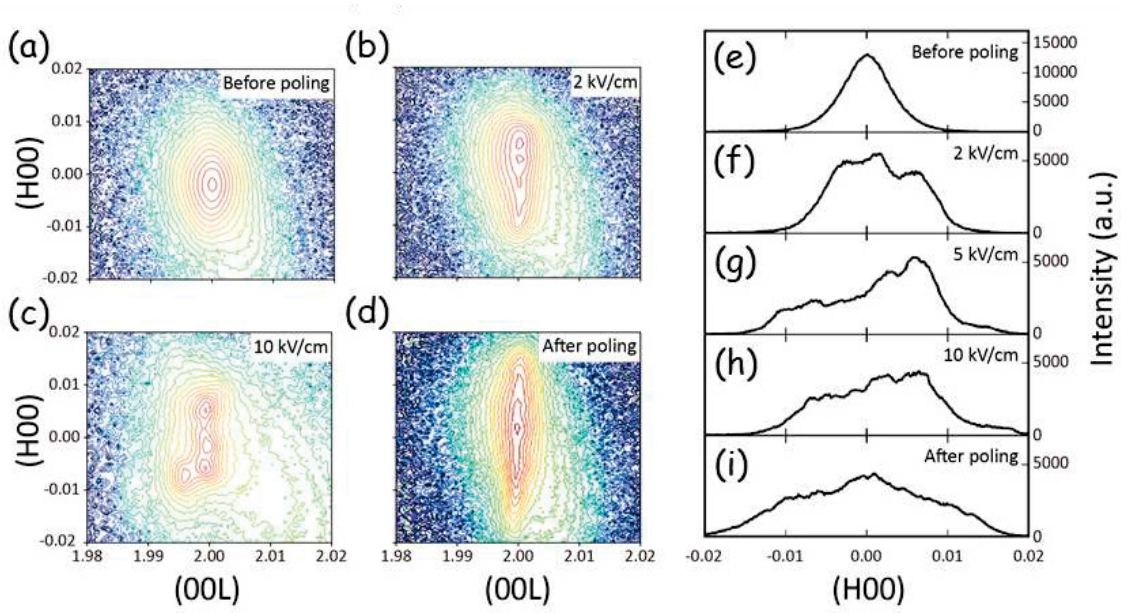

Figure 4.3: (a)-(d) RSM scans and (e)-(i) profile (H00) line scans taken from the front side of Crystal #1 (T=200 μm, P=1000 nm) around the (002) peak under different E-fields. (a) (e) 0 kV/cm (before poling), (b) (f) 2 kV/cm, (g) 5 kV/cm, (c) (h) 10 kV/cm, and (d) (i) back to 0 kV/cm (after poling).

Figure 4.4 provides RSM scams taken from the back side of Crystal #1 featuring a planar electrode. Unlike the results from the front side, the (002) peak on the back did not split into multiple peaks. Rather, the peak became somewhat sharper with increasing E, although a weak shoulder was found along the transverse (H00) direction.

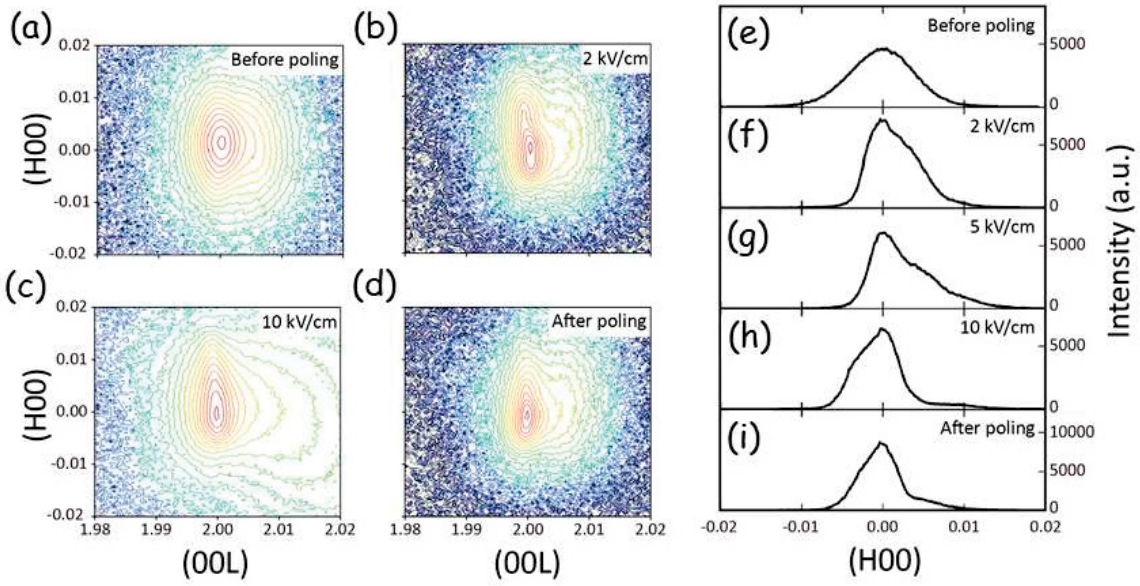

Figure 4.4: (a)-(d) RSM scans and (e)-(i) the profile (H00) line scans taken from the back side of Crystal #1 (T=200 μm, P=1000 nm) around the (002) peak under different E-fields. (a) (e) 0 kV/cm (before poling), (f) 2 kV/cm, (b) (g) 5 kV/cm, (c) (h) 10 kV/cm, and (d) (i) back to 0 kV/cm (after poling).

Similar RSM scans were obtained for Crystal #2, which had a smaller grating size, as shown in Figure 4.5. A doublet peak splitting along the (H00) direction was eventually found for the back side of Crystal #2 with increasing E to 15 kV/cm (see Fig. 4.5h). However, the peak splitting was non-remanent on removal of E. Differences in grating sizes of the nanograted electrodes between 1000 nm and 500 nm did not have a notable effect on the RSM scans.

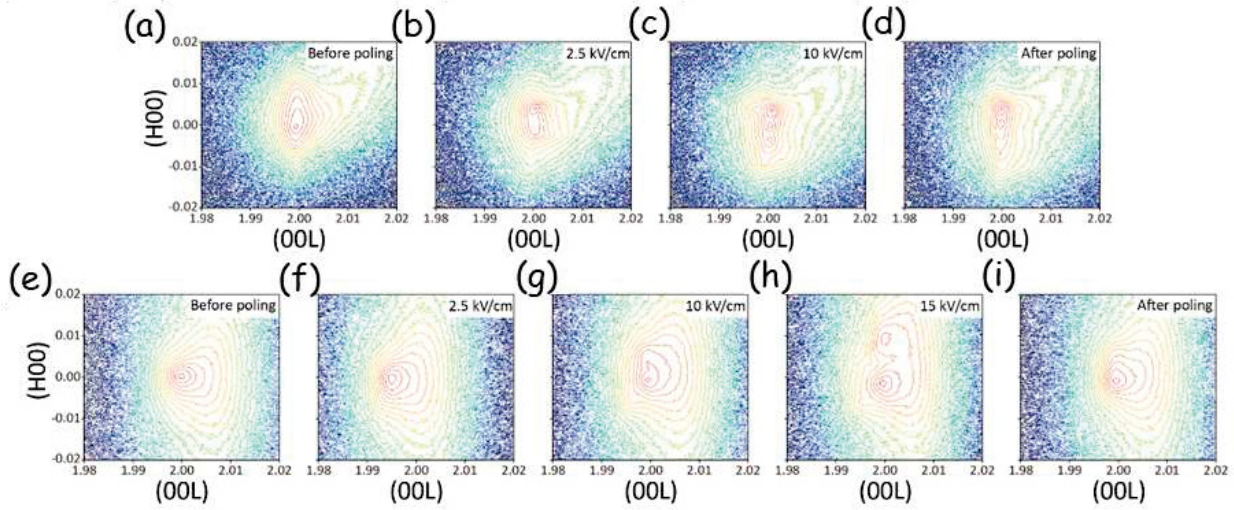

Figure 4.5: RSM scans of Crystal #2 (T=200 μm, P=500 nm) along the [002] zone axis. (a)-(d) front side, (e)-(i) back side. (a) (e) 0 kV/cm (before poling), (b) (f) 2.5 kV/cm, (c) (g) 10 kV/cm, (h) 15 kV/cm, and (d) (i) back to 0 kV/cm (after poling).

Next, the effect of crystal thickness on the RSM scans was studied. The (002) peaks were scanned on both the front and back sides of Crystal #3, as shown in Figure 4.6. The data demonstrate that with increasing thickness from 200 μm to 600 μm, the effects of nanograted electrodes became less pronounced. It can be seen that the (002) peak on the front side slightly split into multiple peaks along the transverse (H00) direction with E, although the peaks were much narrower than for the thinner crystal (see Fig. 4.3). At the same time, the (002) peak on the back side changed with E in a manner similar to that for PMN-30PT with conventional planar electrodes (see Fig. 4.2).

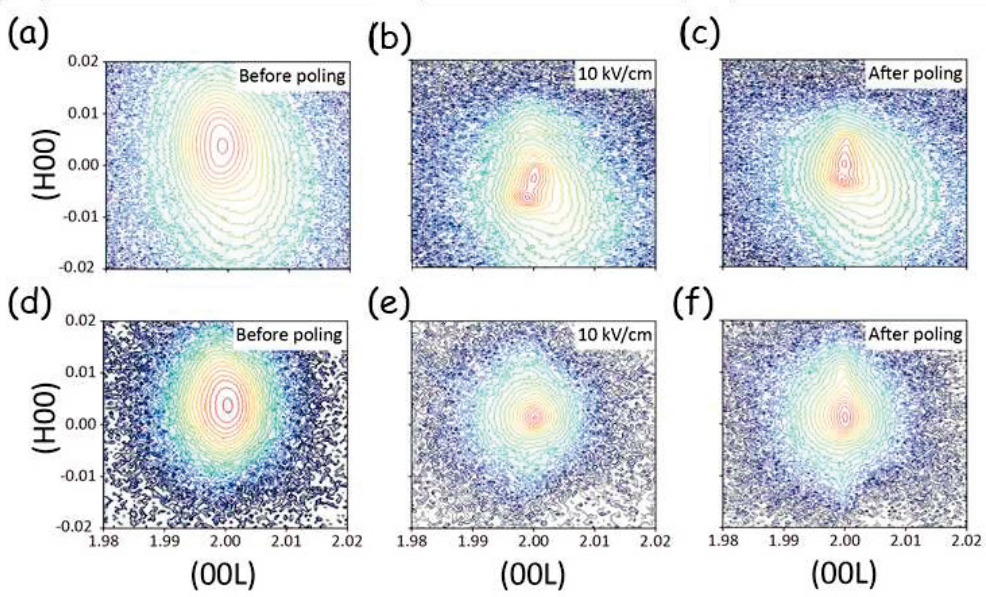

Figure 4.6: RSM scans of Crystal #3 (T=600 μm, P=1000 nm) around the (002) peak. (a)-(c) front side, (d)-(f) back side. (a) (d) 0 kV/cm (before poling), (b) (e) 10 kV/cm, and (c) (f) back to 0 kV/cm (after poling).

The [022] scans taken from the front sides of Crystals #1 and #3 are shown in Figure 4.7 and Figure 4.8, respectively. Doublet peak splitting was found along the (0LL) direction when E reached 2 kV/cm, indicating a R→M_A phase transformation. But unlike the normal R→M_A, splitting was also identified along the transverse (H00) direction, which had a specific orientation, as indicated by the red dashed lines in Fig. 4.7. These results are different from the broad multiple peak splits along the (002) results, which did not have a distinct preferred value.

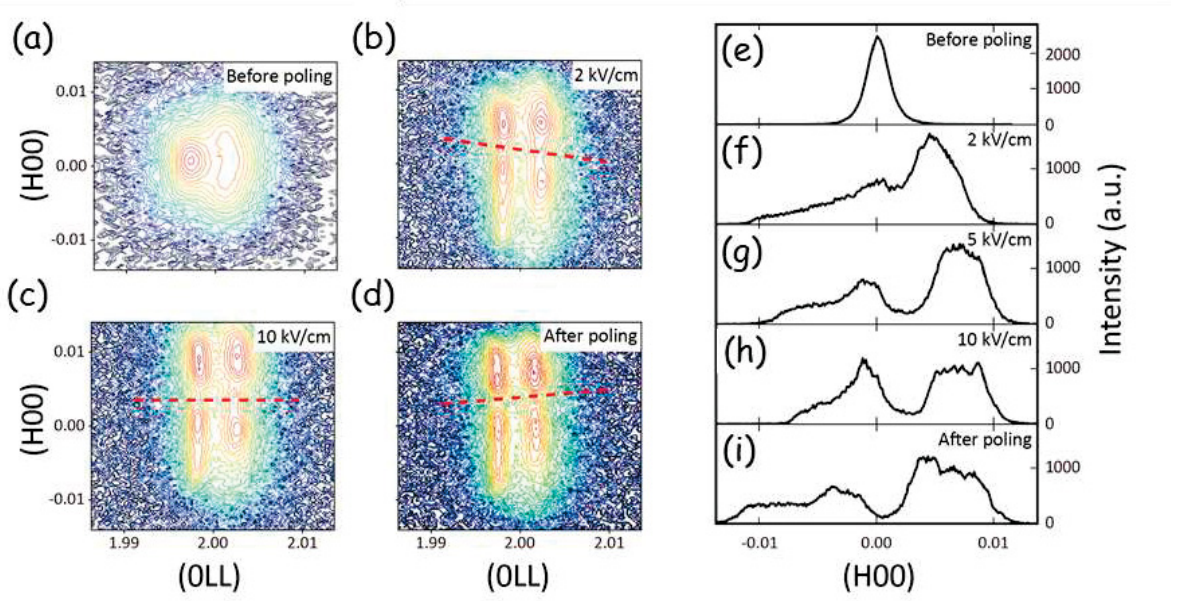

Figure 4.7: (a)-(d) RSM scans and (e)-(i) profile (H00) line scans taken from the front side of Crystal #1 (T=200 μm, P=1000 nm) around the (022) peak under different E-fields. (a) (e) 0 kV/cm (before poling), (b) (f) 2 kV/cm, (g) 5 kV/cm, (c) (h) 10 kV/cm, and (d) (i) back to 0 kV/cm (after poling).

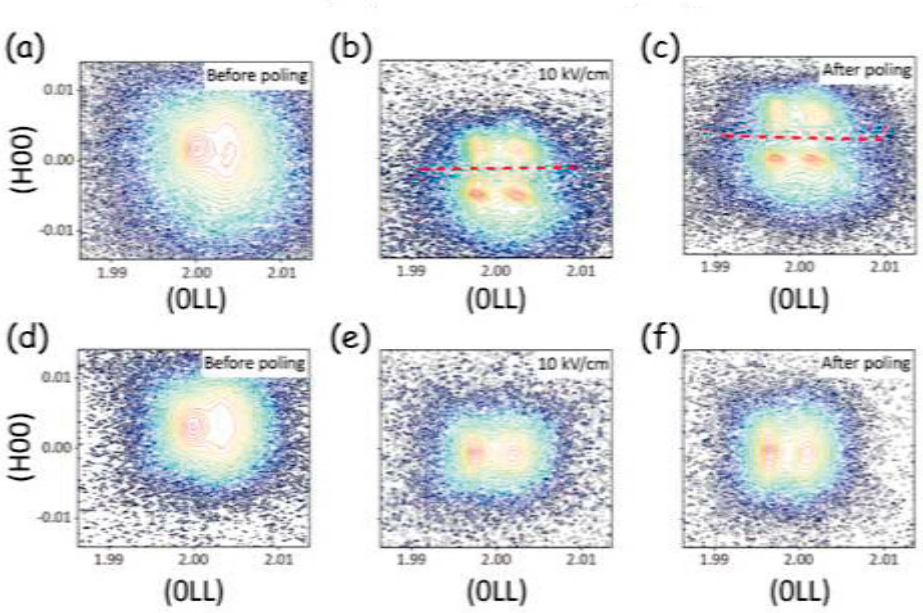

Figure 4.8: RSM images of Crystal #3 (T=600 μm, P=1000 nm) around (022) peak. (a)-(c) top side, (d)-(f) back side. (a) (d) 0 kV/cm (before poling), (b) (e) 10 kV/cm, (c) (f) back to 0 kV/cm (after poling).

The dielectric constants of Crystals #1, #3, and #4 as a function of poling field (measured at 1 kHz) are shown in Figure 4.9a. The PMN-30PT crystals with nanograted electrodes rapidly reached a maximum dielectric constant with increasing E to 3 kV/cm, and remained constant at higher E. The maximum dielectric constant was about 30% higher than the crystal with planar electrodes, which is consistent with prior findings [77]. Note that this field level is similar to that required to induce the M phase in conventional planar electrode crystals [68]. The full frequency dependent dielectric constant results can be found in Figure 4.9b-d, which shows that the dielectric constant was slightly decreased with increasing frequency. This trend is usually observed for the relaxor PMN-PT system in the relaxor state [71].

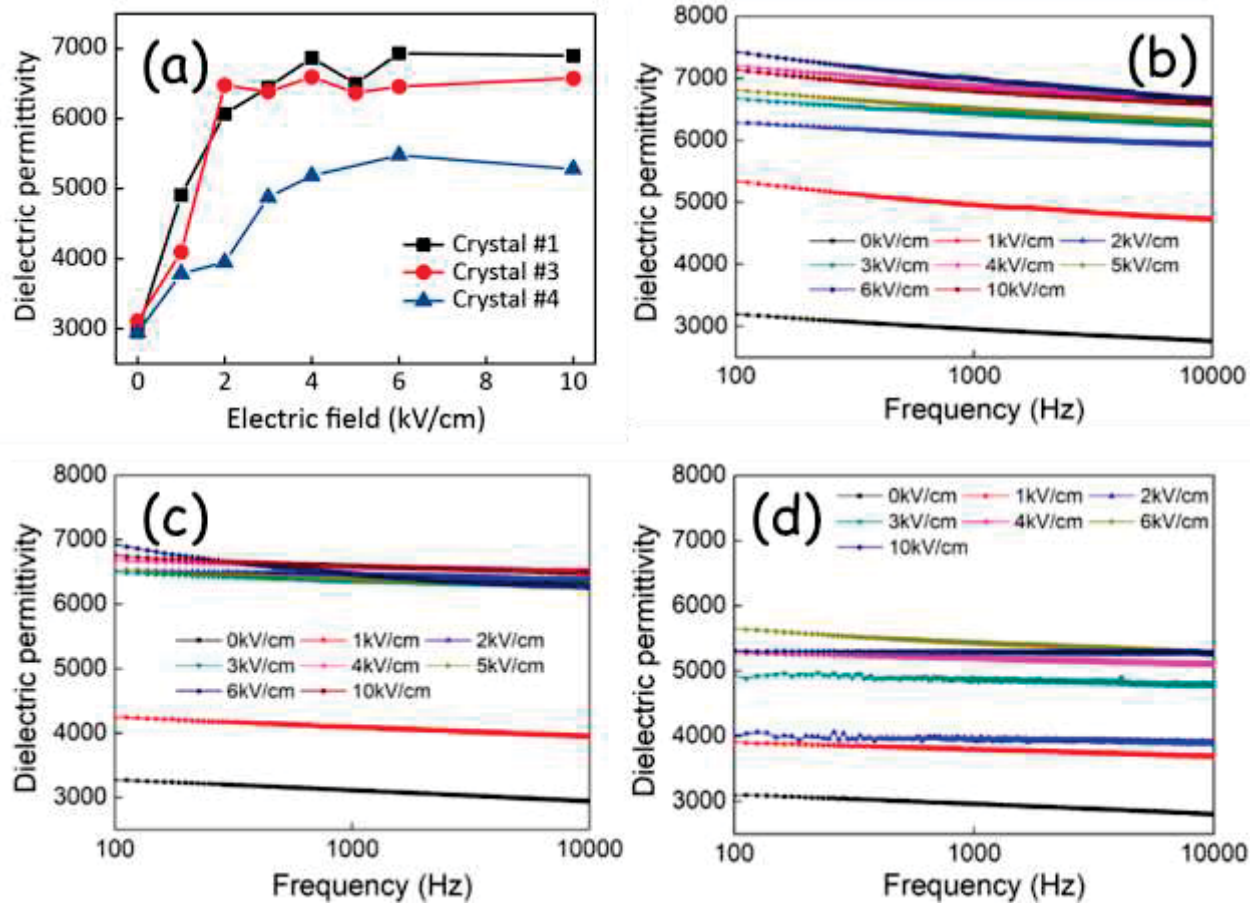

Figure 4.9: (a) dielectric constant of different PMN-PT samples as a function of the poling field at room temperature. (b)-(d) Frequency dependent dielectric constant of different PMN-PT samples under various poling fields. (b) Crystal #1, (c) Crystal #3, and (d) Crystal #4.

Finally, the strain of Crystal #1 and #4 along the [001] direction was calculated from the XRD 2θ scans and plotted as a function of E (Figure 4.10). The strain curves of Crystal #1 exhibited an electrostrictive-like response on both the front and back sides, similar to the slim quadratic ε-E curves previously reported for PMN-PT relaxors at temperature below their freezing transition [172,173]. Similar electrostrictive ε-E responses were found for all crystals with nanograted electrodes. An important difference of our ε-E curves for the nanograted crystals compared to previously reported electrostrictive PMN-PT is that the slope around E=0 was much sharper. In

contrast, Crystal #4 with conventional planar electrodes had typical butterfly-like hysteresis curves, consistent with traditional poled piezoelectric single crystals and ceramics [172,174,175].

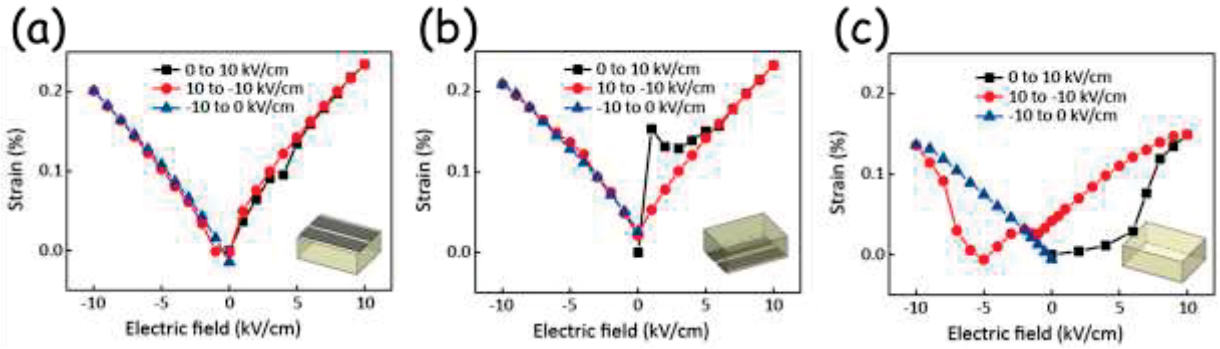

Figure 4.10: Strain of the crystals along the [001] zone axis as a function of the applied E-field: (a) the top side for Crystal #1, (b) the back side for Crystal #1, and (c) the top side for Crystal #4.

4.3. Discussion and domain distribution analysis

The R phase of PMN-xPT features four equivalent polarization variants that are oriented along the (111) directions, which has been designated as the '4R' domain configuration if poled along the [001] direction [71]. Noted that a '2R' domain configuration arises in the actual poled condition; further, they conjectured that the poling field cannot be perfectly aligned to the [001] of the single crystal, and thus an applied E breaks the degeneracy of the '4R' configuration, causing a '4R'→'2R' domain transition [71]. The stable phase in this '2R' domain configuration was M_A (with a similar '2M' domain configuration). This '2M' domain configuration is schematically illustrated in Figure 4.11a for a PMN-xPT crystal with conventional planar electrode, where the domain platelets of PMN-PT are along a single tilting angle α, and the nano-twin distribution within (as shown in the expanded circle) is quite regular and elastically relaxed.

The unpoled (initial) R phase of PMN-xPT consists of PNRs that lack long-range translational invariance with respect to each other. The presence of these PNRs has been confirmed by transmission electron microscopy [172], piezoresponse force microscopy [175], and diffuse neutron

scattering [174]. Under E, the PNR distribution is significantly altered—developing geometrical arrangements that are invariant with increasing E. In the poled condition, this has been shown to result in a hierarchical domain structure, consisting of nanodomains geometrically tiled within domain platelets, which are the '2R' and/or '2M' domain configurations. This M_A phase has previously been designated as the adaptive ferroelectric state, which is a structurally heterogeneous state consisting of R nanotwins geometrically arranged by invariant conditions that minimize the elastic strain energy. In this case, the '4R'→ 2R'/'2M' domain transition is driven by strain energy minimization.

For the crystals with nanograted electrodes, the transverse (H00) splitting along the (002) peak reveals the presence of multiple domain states that have the same lattice parameter as evidenced by a single peak along (00L). We illustrate the domain distribution of the crystals with nanograted electrodes in the schematic of Figure 4.11b. This schematic demonstrates that the tilting angle between neighboring domains is different—namely, that it is not fixed to α, but rather to a range about α_n (1 to N). In addition, the expanded circle shows a similar type of geometrical arrangement of twins, as shown in Figure 4.11a, except that it is less organized due to unrelaxed internal strain caused by the non-uniform E.

The non-uniform E applied through the nanograted electrode results in an internal strain distribution, along with a maladjustment of the nano-twin distribution. Simulations of the E-field distribution under the nanograted electrode were performed using COMSOL. Fringe field effects that are locally 3-8 times larger than the applied field were found at the edges of MnO_x, as shown in Figure 4.11c. However, the simulation was based on a simplified model that assumed the dielectric constant was indeed constant, which may simply reflect the initial E-field condition. In fact, as demonstrated in Figure 4.11d, the high E of the fringe field can locally pole the crystal,

changing its dielectric constant in that region, and, in turn, propagating such higher fields to nearby region [79]. Furthermore, one cannot neglect the effect of Mn doping/diffusion on altering the local E-field distribution beneath the electrodes. Studies have shown that Mn can diffuse into the near-surface region of PMN-xPT crystals from the MnO_x electrodes, which may alter local domain nucleation [77,79,174]. The Mn-rich regions overlap onto the local high fringe field ones to some extent, and thus these two factors need to be taken into consideration synergistically in understanding surface nanodomain distribution [79].

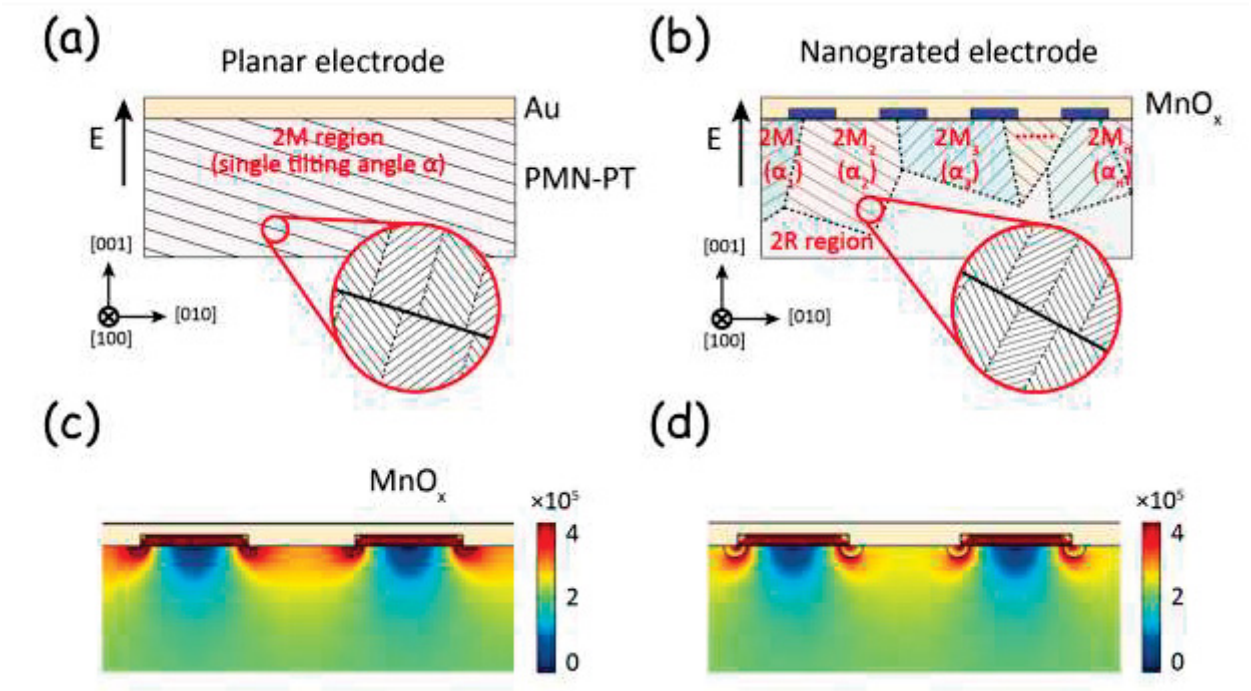

Figure 4.11: Schematic illustrations of the nano-twin domain distributions with (a) planar electrode, and (b) nano-patterned electrode. Distortion angles α_n in (b) have a wide distribution of values, whereas those in (a) have a single regular value. (c) Simulation of the initial E distribution at the near-surface region beneath the nanograted electrodes. (d) Simulation of the E distribution beneath the nanograted electrodes after the local regions (surrounded by the black curves) had been poled.

Starting with the initial condition of E<2 kV/cm, the field beneath the nanograted electrode was insufficient to induce a change in the nanodomain distribution. Thus, the crystal remained in the R or C phase, and there was only a single peak along the transverse (H00) direction. In the case of E≥2 kV/cm, the non-uniform E resulted in a broadening and splitting of the transverse peak. At the same time, the doublet peak along the (0LL) direction revealed a $R \rightarrow M_A$ phase transformation. With increasing E applied to the nanograted electrode, the transverse peak broadening and multiplicity continued to increase. The broadening and multiplicity of the transverse peak was retained upon removal of E—the changes in the nanodomain distributions were remanent. This locked-in maladjusted condition then allowed the ensemble of twins to store excess mechanical energy, which in turn increased its dielectric constant (see Fig. 4.9) and piezoelectric properties [77], which is conceptually similar to outcomes predicted by adaptive phase theory [72]. Note that the dielectric constant in Fig. 4.9a approaches its maximum plateau at E=3kV/cm, which is close to the field required to fully pole a PMN-xPT crystal with a conventional planar electrode beginning from the annealed or zero-field-cooled (ZFC) condition [63].

Simulations of field distribution revealed that E became more uniform with increasing depth beneath the nanograted electrode (see Fig. 4.11c). This trend helps explain the differences in the RSM and transverse line scans between the front and back sides of the crystal. With increasing E, the transverse line scan from the back side became somewhat narrower. A weak tendency to develop shoulders was also found, but a single Gaussian peak was recovered on removal of E. The back side had RSM and transverse line scans similar to that of the R phase.

The differences in transverse splitting between the front and back sides demonstrate a gradient of the structure and nanodomain distribution throughout the crystal thickness, also implying a strain gradient. The nanodomains closer to the front side undergo redistribution under

E, but cannot establish the geometric invariant conditions necessary for the M_A phase. In contrast, the nanodomain distribution on the back side remains close to that of the relaxed M_A phase. This finding is consistent with a very recent report for nanograted PMN-xPT crystals using PFM by Luo et al., where the near top-surface regions consisted of '2R'/'2M' domains, while the deeper regions consisted of '4R' domains. The differences between these domain states is in the relaxation of their nanodomain distributions and their geometrical arrangement within the larger macrodomains.

It is important to note that the RSM scans along the [022] zone axis exhibited a doublet splitting along both (H00) and (0LL) for the nano-pattern electroded crystals. Interestingly, this direction is the habit plane for twinning in rhombohedral and tetragonal structures [176]. It is along this direction where stress accommodation occurs, and where the twins become geometrically stacked into invariant conditions. This (H00) splitting evidences two M_A domain platelets (i.e., '2R' or '2M') that are tilted with respect to each other along the (H00), which then consist of nanotwins. The nanotwin distribution does not achieve the invariant conditions of the M_A phase, but their domain platelets may partially relax their elastic energy by tilting the orientation of the domain bands with respect to each other. It is also interesting to note the simulations of E field distribution around the edges of the MnO_x regions of the nanograted electrode. According to the simulation results, the non-uniform E distribution has a spatial pattern like that of periodic needles. Inspection will reveal a stronger gradient of E along the [011] and [0-11] directions. This directional field gradient may play an important role in establishing two types of R macrodomain platelets that are rotated with respect to each other.

It is also important to note that increasing crystal thickness resulted in significant changes in the RSM scans with E. Thicker crystals that had nanograted electrodes did not exhibit significant

changes in either width or multiplicity with increasing E. Rather, the RSM scans remained typical of that exhibited for the M_A/R phase. With increasing thickness, it becomes more difficult for the near-surface regions to elastically relax their nanodomain distributions; instead, they become mechanically constrained by the elastic boundary conditions of the volume. Accordingly, the enhanced dielectric and piezoelectric properties can be attributed to changes in nanodomain distribution. The strain along the [001] zone as a function of E, measured *in-situ* under E by XRD, are shown in Figure 4.10. The data demonstrates an electrostrictive-like response, unlike the butterfly-like curves of crystals with conventional planar electrodes [72,177]. This electrostrictive behavior is similar to that found in the relaxor ferroelectric state, where nanodomain redistribution under E results in strain, without the presence of macrodomain platelets.

The summation of our findings clearly demonstrate that the nanodomain distribution in PMN-xPT single crystals is most important to its average structure. Readjustments of the nanodomain distribution can impart significant improvements to the unique piezoelectric properties, as well as to the phase transformational sequence and domain transitions that occur with E and temperature. This assertion is evidenced by the slim quadratic (i.e. electrostrictive) ε-E curves of the nanograted crystals being due to the reversible realignment of the nanotwins within domain striations that are unaltered. These findings are consistent with a structurally non-uniform polar state that can undergo a series of adaptations into various related states driven by the minimization of elastic energy [72].

4.4. Summary

X-ray RSM scans were used to study the E-induced changes in the apparent symmetry and domain distribution of near-surface regions for PMN-30PT crystals with nanograted oxide

electrodes. The scans revealed a multitude of splittings under E along the transverse (H00) direction about the (002) peak, which persisted even after the removal of E. The scans along the (022) zone suggested the presence of the M_A phase. Studies of the back surface (which had a planar electrode) revealed a sharp single peak. The data evidence a geometrical stacking of nanotwins along the [011] direction that is inhomogeneous due to the electric field gradient. The excess elastic energy stored in the nanodomain distribution results in enhanced dielectric/piezoelectric properties. Comparisons of scans on the front and back sides revealed a gradient in the apparent crystal symmetry and the domain distribution throughout the thickness of the crystals.

Chapter 5. Magnetoelectricity of $CoFe_2O_4$ and tetragonal $BiFeO_3$ nanocomposites

As detailed in Section 3, the antiferromagnetic nature of BFO has been employed to fabricate ME nanocomposites with ferroelectric (FE) PMN-PT single crystals. The FE nature of BFO can be utilized to make ME nanocomposites with ferrimagnetic $CoFe_2O_4$ (CFO), which is described in this section.

The spinel CFO is a typical ferrimagnetic oxide that features a high saturation magnetization, high Curie temperature, and large magnetocrystalline anisotropy [178-180]. Combined with its large magnetostriction coefficient (λ_{100}: -250×10^{-6} to -590×10^{-6}), CFO is a good choice for the magnetostrictive phase in ME composites [178,181]. Additionally, antiferromagnetic BFO and ferrimagnetic CFO also exhibit exchange coupling at the interfaces [182,183]. Such all-oxide systems have been proposed to overcome the limitations stemming from the incompatibility between dissimilar material types in oxide/metal heterostructures [57,184,185]. Actually, a number of studies have investigated nanocomposites of CFO/BFO that self-assemble into vertically integrated nanopillar structures ((1-3) type), which result from an immiscibility and lattice mismatch between the CFO and BFO phases [180,186]. Similarly, our group has investigated the ME effect of CFO/BFO on PMN-PT single crystals [132,187]. However, all prior investigations have focused on the R-BFO with CFO [132,183,186-188]; in contrast, CFO/T-BFO nanocomposites have not yet been reported. To address this scholarly deficit, CFO/T-BFO nanocomposites were fabricated on (001) LAO substrates by PLD, and its ME properties were compared with that of CFO/R-phase BFO ones on (001) STO substrates.

5.1. Fabrication of CFO/BFO nanocomposites and experimental setup.

CFO and BFO layers were deposited as individual layers on both (001) LAO and (001) STO single crystal substrates. While the CFO thickness was varied from 7 nm to 14 nm, the BFO thickness was maintained at 28 nm. In order to prevent Bi evaporation, the deposition temperature was kept at 650 ℃. The oxygen partial pressure was fixed at 90 mTorr for the deposition of BFO, and at 100 mTorr for CFO. Prior to the deposition of CFO, the as-grown BFO films were *in-situ* annealed in a pure O_2 atmosphere of 100 mtorr at 650 ℃ for 30 min. To investigate the annealing effect on the CFO layer, after the deposition of CFO, the as-grown films were *in-situ* annealed in a pure O_2 atmosphere of 100 Torr at 725 ℃ for 0 min, 15 min, or 30 min.

The crystal structures were characterized using our XRD system, and surface topology was observed by the AFM. Furthermore, PFM and MFM were used to image the ferroelectric and magnetic domains, respectively, as well as to detect the change of magnetic signals under a tip bias. To achieve PFM measurements, a 5 nm SRO buffer layer was deposited between the BFO layer and substrates by PLD. The magnetic hysteresis loops were measured with the VSM system while the field cooling curves were measured by the SQUID system. The surface composition was semiquantitatively analyzed using X-ray photoelectron spectroscopy (XPS, PHI Quantera SXM). A JEOL 2100 TEM was employed to observe the cross-sectional images of the CFO/T-BFO nanocomposites. The EDS line scans were taken by a silicon drift detector-based EDS system integrated in the TEM. The TEM specimen was prepared by FIB.

5.2. Annealing effect on the CFO/BFO nanocomposites

First, the effect of anneal on the CFO/BFO nanocomposite was investigated. Figure 5.1 shows AFM height images of samples having different annealing conditions. The as-grown

CFO/BFO nanocomposites on both LAO and STO substrates exhibited smooth surfaces with a roughness of less than 1 nm. The step-and-terrace surface topography indicated the layer-by-layer growth of the thin films. After 15 min of annealing, the smooth surfaces began to develop into specific topographies that exhibited an obvious increase in roughness. After 30 min of annealing, the surface topography was completely transformed into different morphological patterns. Platform-like structures were observed for CFO/BFO nanocomposites on (001) LAO, and a typical nanopillar structure was found for those on STO [188]. The profile images in Figure 5.2 indicate that there are three distinguishable platform heights for the CFO/BFO nanocomposites on LAO substrates, where each platform displayed a relatively flat surface with a local roughness of less than 1 nm.

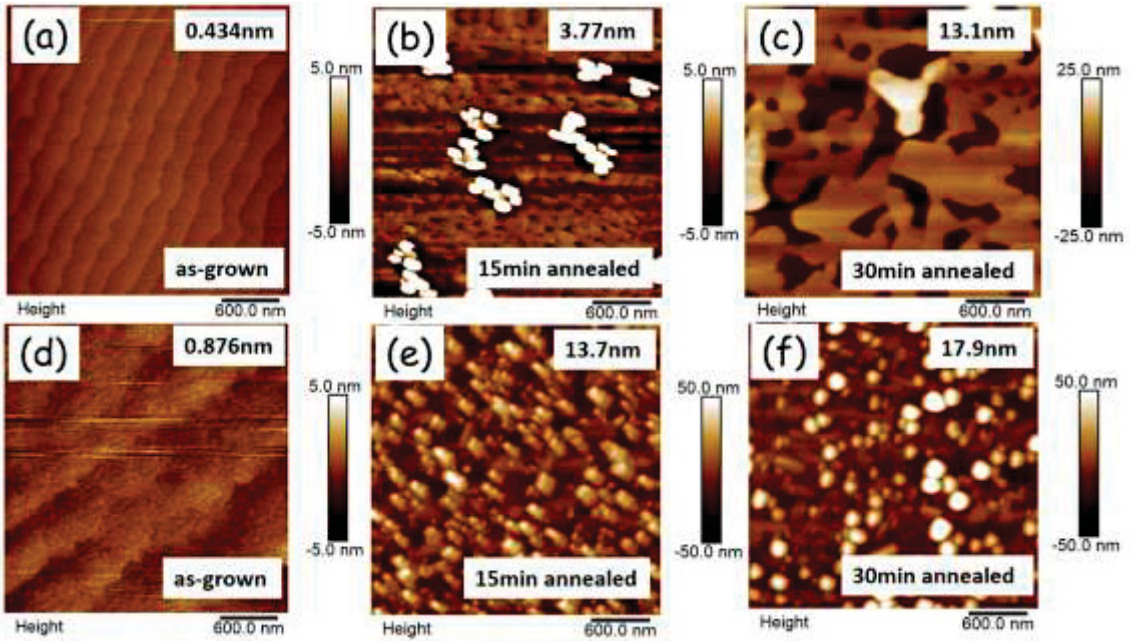

Figure 5.1: AFM height images of (a)-(c) CFO(7)/BFO(28)/(001) LAO, and (d)-(f) CFO(7)/BFO(28)/(001) STO. (a) (d) the as-grown samples, (b) (e) the 15 min annealed samples, (c) (f) the 30 min annealed samples. Surface roughness data are provided in the insets.

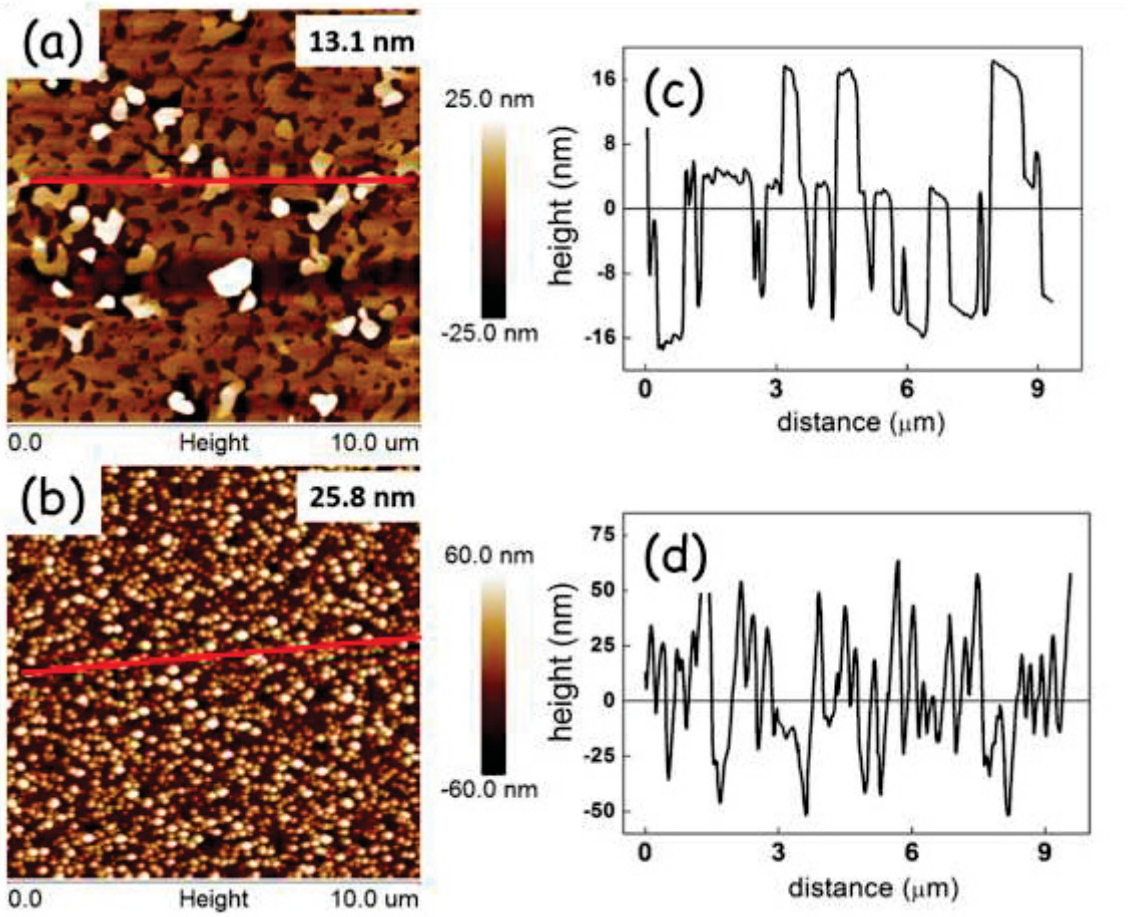

Figure 5.2: AFM height images of (a) CFO(7)/BFO(28)/(001) LAO sample, and (b) CFO(7)/BFO(28)/(001) STO sample. Surface roughness data are provided in the insets. (c) and (d) are the profile images extracted along the red lines of (a) and (b), respectively.

Such differences in surface morphology could be induced by the lattice parameter mismatch between the CFO and BFO phases [189]. The XRD patterns in Figure 5.3a and 5.3b demonstrate that the BFO deposited on LAO and STO substrates had T and R structures, respectively. In both cases, the BFO peaks had a clear shift to higher 2θ values after annealing, indicating a significant strain relaxation due to the formation of self-assembled structures. The (004) CFO peaks were only observed on top of the R-BFO layer, similar to previous structure

studies of CFO/R-BFO nanocomposites [132,183,186]. On top of the T-BFO layer, however, no such (004) CFO peaks were detectable. Considering that the in-plane crystal lattice mismatch between CFO and T-BFO (12%) is much larger than that between CFO and R-BFO (5%), it is reasonable to conclude that the CFO on T-BFO had a lower crystalline quality [188]. However, the XPS patterns shown in Figure 3.20c clearly reveal Co peaks, suggesting that CFO may also exist on the top layers [190,191]. Noting that XPS can only detect the top 10 nm of a sample, the fact that the XPS patterns revealed both Co and Bi peaks confirms that the CFO/BFO samples formed some type of self-assembled structure, despite the fact that CFO and BFO were deposited in separate steps prior to annealing. The difference in morphologies between CFO/T-BFO and CFO/R-BFO could account for the different Co/Bi ratios in the XPS analysis given in Fig. 5.3c.

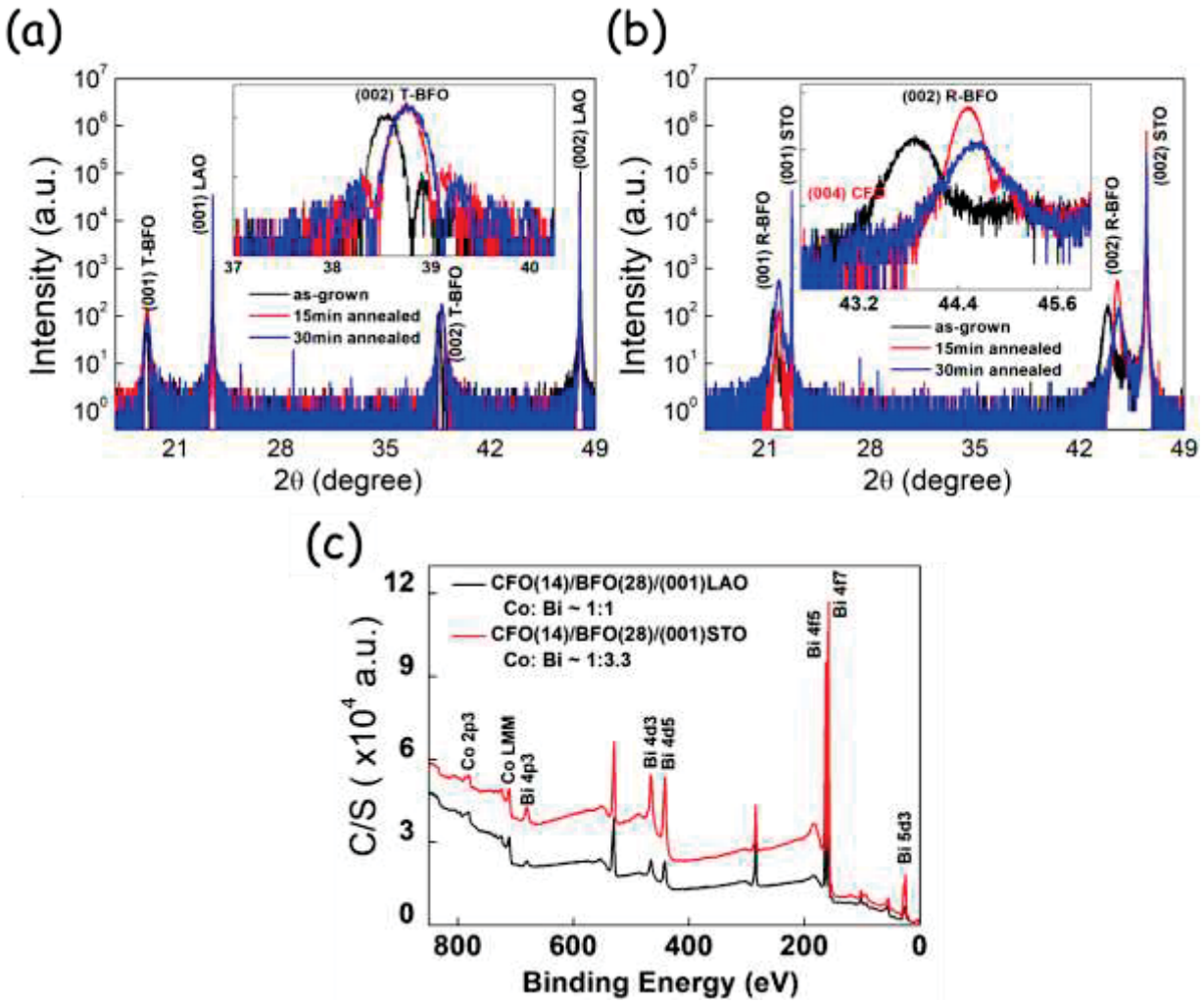

Figure 5.3: (a) (b) XRD patterns of (a) CFO(7)/BFO(28)/(001) LAO, and (b) CFO(7)/BFO(28)/(001) STO samples after different anneal processes. The inset in (a) and (b) shows the peak shifts caused by post-heat treatments. (c) XPS patterns of CFO(14)/BFO(28) nanocomposites.

Cross-sectional TEM images given in Figure 5.4a-c demonstrate that the CFO/T-BFO nanocomposites remained as a bilayer structure after annealing. The platform-like topography resulted from a discontinuity in the CFO phase distribution. Figure 5.4e and 5.4f shows an EDS line scan reflecting the elemental distribution within the nanocomposite. In Figure 5.4d, the SAED

pattern along the [010] zone axis exhibited good epitaxial T-BFO patterns on the LAO substrate. The lattice parameter of the T-BFO along the (001) direction was about 4.65 Å, which is consistent with the XRD results (4.64 Å). Moreover, as shown in the inset of Fig. 5.4d, a triplet splitting was identified, where one peak belonged to the (001) CFO phase. The calculated (001) inter-planar lattice spacing of CFO was about 4.88 Å, which is close to that directly measured in Fig. 5.4c (4.89 Å), but notably larger than that of the cubic CFO's lattice parameter ($\frac{1}{2}a_{CFO}$=4.19 Å). The diffraction pattern of CFO along the (100) orientation was barely distinguishable in these patterns, indicating that the CFO lattice may be under significant in-plane compressive strain that disrupted the periodicity along that direction. Based on these TEM observations, it can be reasonably concluded that the CFO phase on top of the T-BFO also had a T-phase-like structure, which may explain why the CFO phase forms a platform-like phase distribution with BFO on LAO substrates, instead of the previous reported nanopillar distribution when deposited on STO.

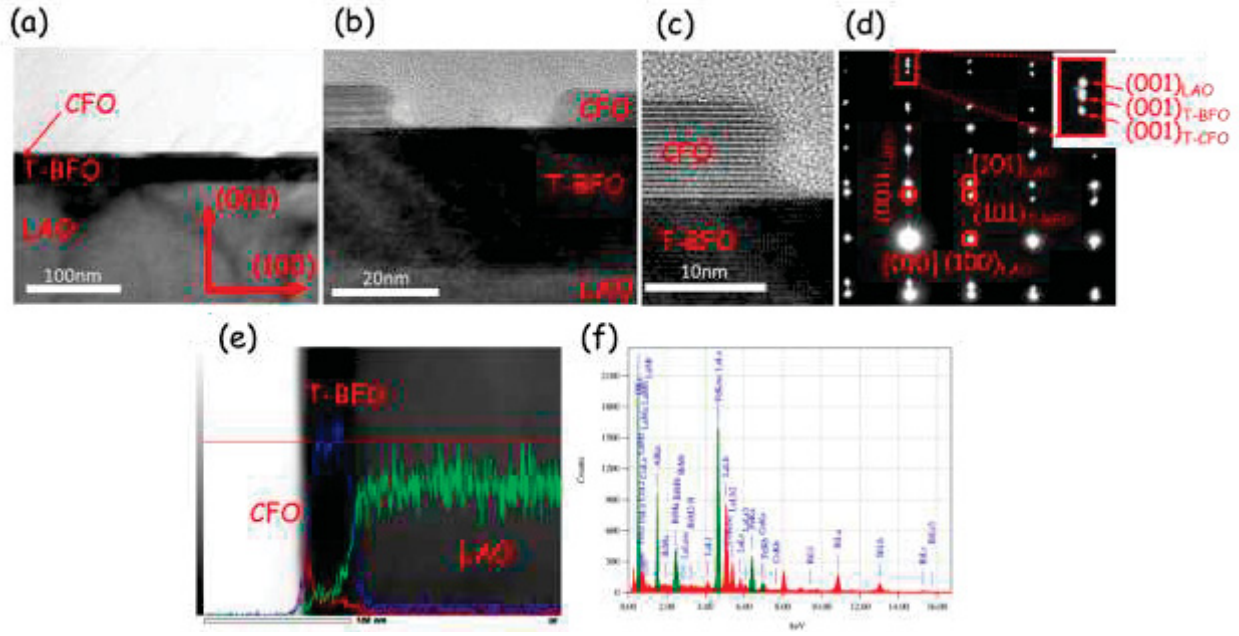

Figure 5.4: (a)-(c) the cross-sectional TEM images of CFO(7)/T-BFO nanocomposite under different scales. The crystal orientation is shown in (a). (d) SAED patterns of (b). The zone axis is along [010] direction. The inset in (d) is the zoom-in image showing a triplet split along (001) orientation. (e) (f) EDS line scan of CFO(7)/T-BFO nanocomposite. The red, blue, and green lines in (e) represented Co, Bi, and Al elements, respectively.

Figure 5.5 shows magnetic hysteresis loops measured by VSM. The magnetization was normalized by the nominal volume of the CFO layer. Since the maximum magnetic field applied was about 5000 Oe, the CFO layers did not reach complete saturation [183]. The as-grown CFO/BFO nanocomposites on either LAO or STO substrates exhibited a similar magnetic isotropy with a small coercivity of less than 120 Oe, indicating that without the post-heat treatment the CFO layer would display poor crystal quality.

After 15 min annealing, as specific surface morphologies began to develop, the two types of nanocomposites trended towards opposite magnetic anisotropies. Specifically, for the CFO/T-

BFO on LAO, the platform-like topography induced an in-plane (IP) magnetic anisotropy; in contrast, for the CFO/R-BFO on STO, the nanopillar morphology resulted in an out-of-plane (OP) magnetic anisotropy [183,188]. In both cases, however, the magnetic coercivity increased to about 800 Oe, indicating an improvement in CFO phase crystallinity.

When the annealing time was further increased to 30 min, the contrasting magnetic anisotropies noted above became even more obvious, consistent with trends of the AFM images in Fig. 5.1, where self-assembled phase distributions became more apparent. In addition, the OP magnetic coercivity of the CFO/R-BFO was significantly increased to 2450 Oe due to a spin-flop coupling at the ferrimagnetic/antiferromagnetic interface [183,184,192]. This coupling effect has been suggested to tilt the antiferromagnetic spins in BFO with respect to the CFO's spins in the interface region between the two phases during field reversal, enhancing the coercivity and introducing an exchange anisotropy energy. However, under the same annealing conditions, the OP magnetic coercivity of the CFO/T-BFO remained low (see Figure 5.6 for a more direct comparison of the IP and OP coercivities of the two types of CFO/BFO nanocomposites under different heat treatments). This low coercivity can likely be attributed to the relatively poorer crystallinity of T-phase-like CFO on T-BFO, as evidenced by the XRD and TEM SAED patterns, compared to the cubic-phase CFO with R-BFO. However, the low coercivity may also indicate a change in the magnetization switching mechanism, given that the antiferromagnetic spin state in the T-BFO is different from that in the R-phase. The much narrower hysteresis loops of the 7 nm CFO on T-BFO demonstrate a much lower energy dissipation on magnetization reversal, which could be beneficial to microelectronic devices.

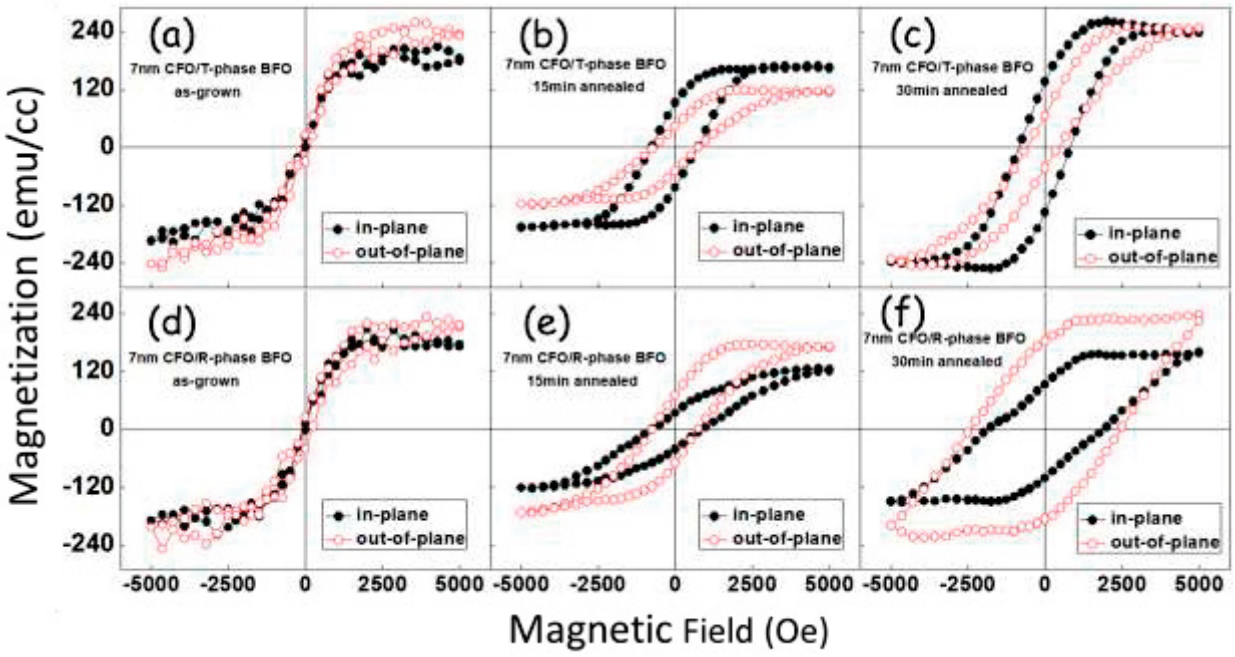

Figure 5.5: Magnetic hysteresis loops of (a)-(c) CFO(7)/BFO(28)/(001) LAO and (d)-(f) CFO(7)/BFO(28)/(001) STO. (a) (d) the as-grown samples, (b) (e) 15 min annealed samples, and (c) (f) 30 min annealed samples.

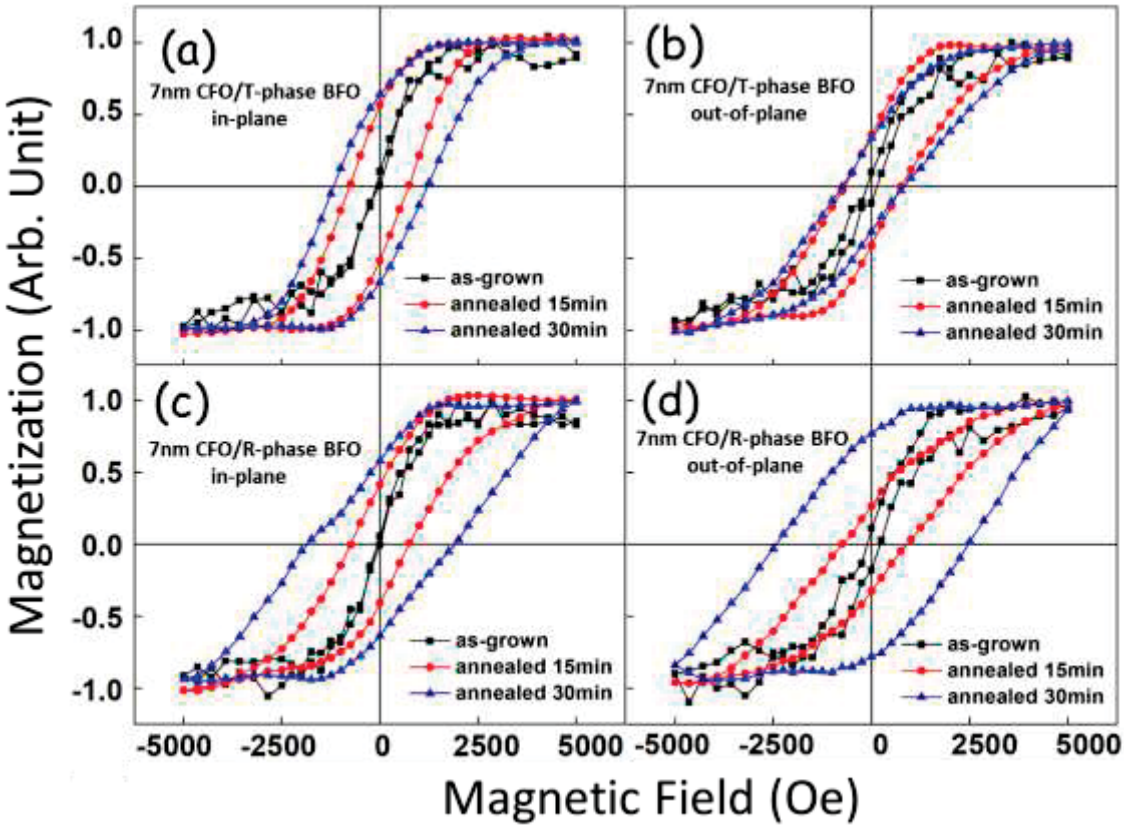

Figure 5.6: Magnetic hysteresis loops of (a) (b) CFO(7)/BFO(28)/(001) LAO, and (c) CFO(7)/BFO(28)/(001) STO samples after different annealing conditions. (a) (c) measurements along IP direction, and (b) (d) measurements along OP direction. The magnetizations were normalized by the maximum magnetization of each loop.

5.3. Thickness effect on the CFO/BFO nanocomposites

Figure 5.7 shows the thickness effect of the CFO layer on the magnetic coercive field, in particular along the OP direction. The CFO/T-BFO had a distinctive enhancement in its OP coercivity, from 710 Oe to 2120 Oe, as the thickness of the CFO layer increased from 7 nm to 14 nm; in contrast, for the CFO/R-BFO, its OP coercivity dropped from 2450 Oe to 2090 Oe. At the

same time, 14-nm thick CFO on either T-BFO or R-BFO featured similar hysteresis loops, with some anisotropic differences due to shape anisotropy.

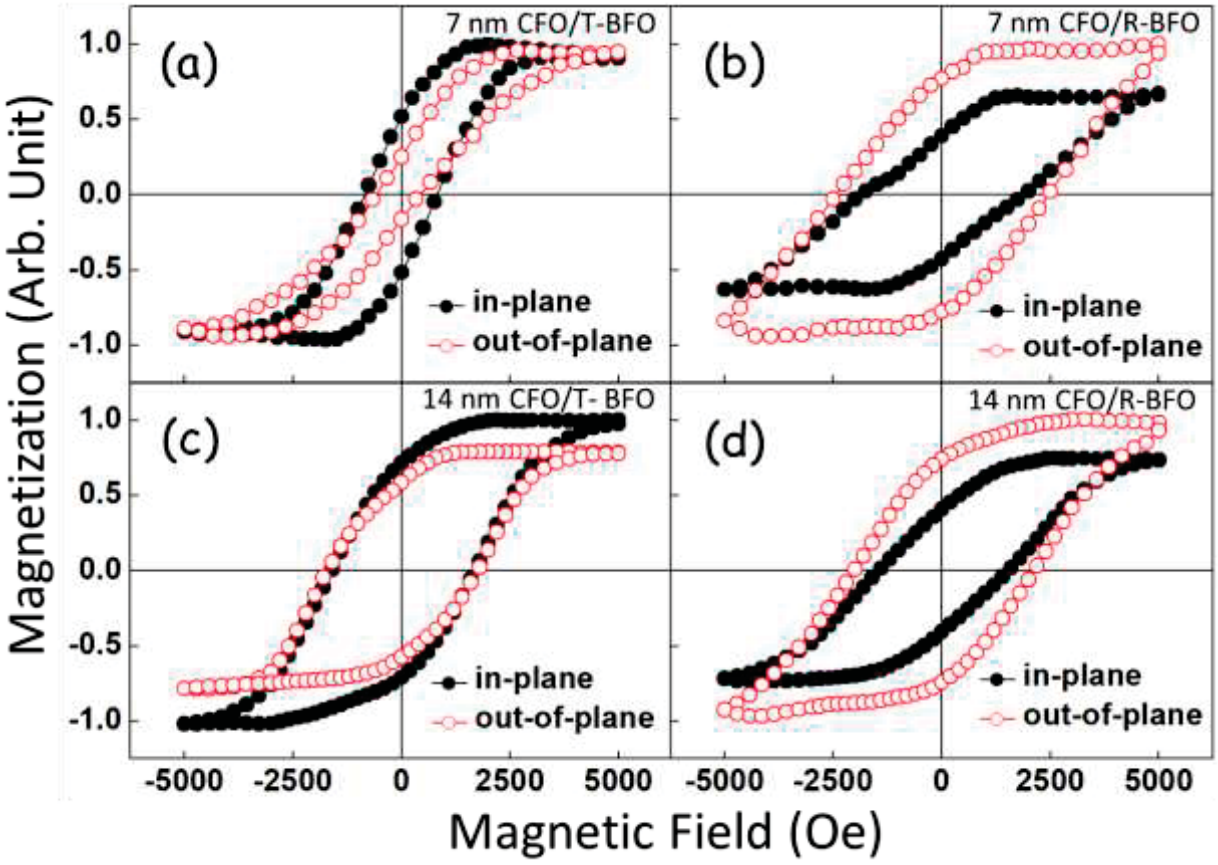

Figure 5.7: Magnetic hysteresis loops of (a) (c) CFO/T-BFO on (001) LAO, and (b) (d) CFO/R-BFO on (001) STO. The thickness of CFO was 7 nm in (a) (b), and 14 nm in (c) (d). The magnetizations were normalized by the maximum magnetization of each loop.

For the CFO/T-BFO nanocomposites, the enhancement in coercivity may be attributed to its improved crystallinity, given that the T-phase CFO peaks can be seen in the XRD patterns of Figure 5.8a when the thickness of the CFO layer was increased to 14 nm. It is important to point out that without the BFO layer, even a 50 nm CFO layer on (001) LAO did not reveal T-phase

peaks. Clearly, in this case, the T-BFO plays a key role as the template for inducing an epitaxial T-phase CFO on top of it.

On the other hand, when considering the CFO/R-BFO, the decrease in coercivity can be explained from the perspective of strain and interface coupling effects. For the strain effect, as the thickness of the CFO is increased, the internal strain of the layer becomes increasingly relaxed. Accordingly, this would decrease the magnetoelastic energy (K_{me}), given as:

$$K_{me} = -\frac{3}{2} \times \lambda_{001} \times Y \times \varepsilon_{001}, \qquad 3.3$$

where λ_{001}, Y, and ε_{001} are the magnetostrictive coefficient, Young's modulus and OP strain of CFO, respectively [183,193]. The insert in Fig. 5.8b shows that the (004) CFO XRD peak shifted for the 14 nm layer, indicating reduced strain in the layer. For the interface coupling effect, because the exchange enhancement mentioned above is an interface, as thickness is increased, it weakens.

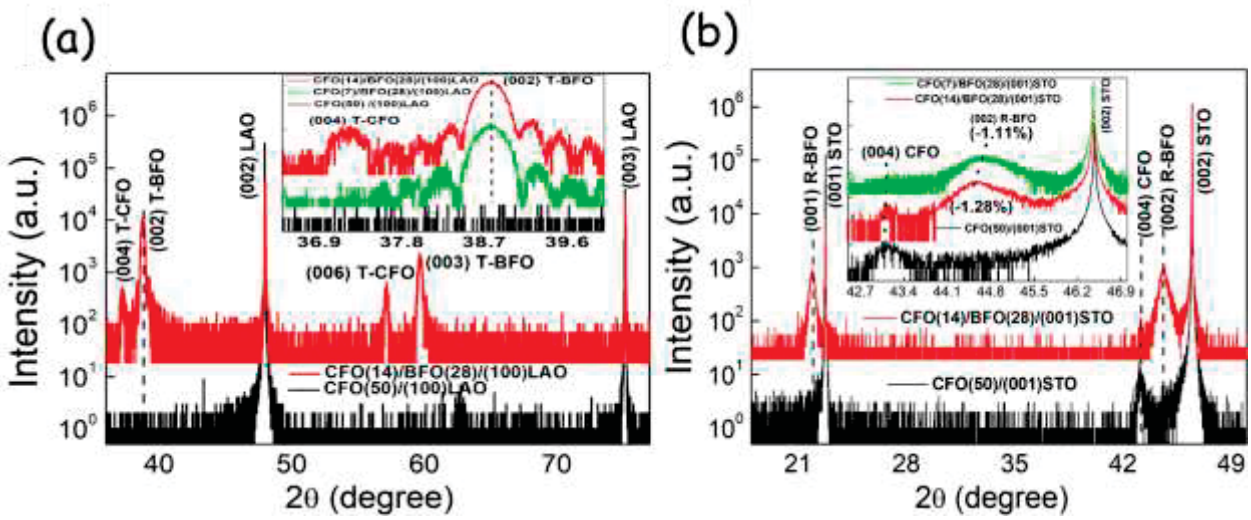

Figure 5.8: XRD patterns of (a) CFO/T-BFO nanocomposites, and (b) CFO/R-BFO nanocomposites. the insets in (a) (b) show the strain changes in CFO and BFO caused by a thickness factor.

5.4. ME effect in the CFO/BFO nanocomposites

Figure 5.9 presents corresponding MFM and PFM phase images of these two different types of CFO/BFO nanocomposites. The bright and dark contrast in the MFM phase images that originate from the stray field of CFO reveals different magnetic domains with opposite spin orientations. Since the samples were pre-magnetized along the OP direction, and MFM images were recorded at a remanent state, the opposite contrast represents the OP magnetization of CFO. In Fig. 5.9a, each nanopillar of the CFO/R-BFO sample contained only a single magnetic domain, which is similar to previous reports for CFO-BFO self-assembled nanopillars [194,195]. This outcome can be link to shape and size effects, where the nanopillar structure restricts the size of the magnetic domains. However, as indicated in Fig. 5.9c, each platform of the CFO/T-BFO sample can be seen to contain multiple magnetic domains. The platforms were larger in size than the nanopillar, thus a multi-domain structure developed to lower the total energy.

The contrast in the PFM phase images confirms the FE nature of BFO. In Fig. 5.9b, the sphere-like patterns were caused by the protuberant CFO nanopillars rather than the actual piezoresponse signal of the R-BFO. This observation may indicate that the BFO matrix was covered by dense CFO nanopillars [194,196], similar to the bilayer structure shown in Fig. 5.4a. However, the inset in Fig. 5.9b reveals a contrast change (see rainbow scaling), indicative of BFO's FE beneath the CFO nanopillars. Fig. 5.9d shows that the CFO/T-BFO sample exhibited a mosaic domain pattern. Although CFO platforms covered part of the surface, small regions of bright and dark contrast represented opposite [001] polarizations of the T-BFO. The box-in-box pattern at the center illustrates the tenability of the FE polarizations within the CFO/T-BFO nanocomposites.

Finally, as illustrated in Fig. 5.9c and 5.9e, MFM scans are shown before and after poling by a +9 V tip bias. The MFM phase profile in Fig. 5.9f confirms that the magnetic phase signal

was tuned by the voltage. This increased phase contrast with some domain pattern changes can be attributed to the ME coupling between CFO and T-BFO at the interfaces [197]. The more highly aligned FE polarization in the T-BFO may result in better spin alignment in the CFO phase via strain, leading to enhancement of the magnetization [198]. An exchange coupling should also be considered, where the reorientation of FE polarization affects the antiferromagnetic spin distribution within the BFO phase, which could influence the ferrimagnetic spin arrangement in the CFO [40,60,199]. Similar enhancements were observed when applying a -9 V tip bias, based on the fact that the [001] and [00-1] FE polarizations of the T-BFO were actually equivalent.

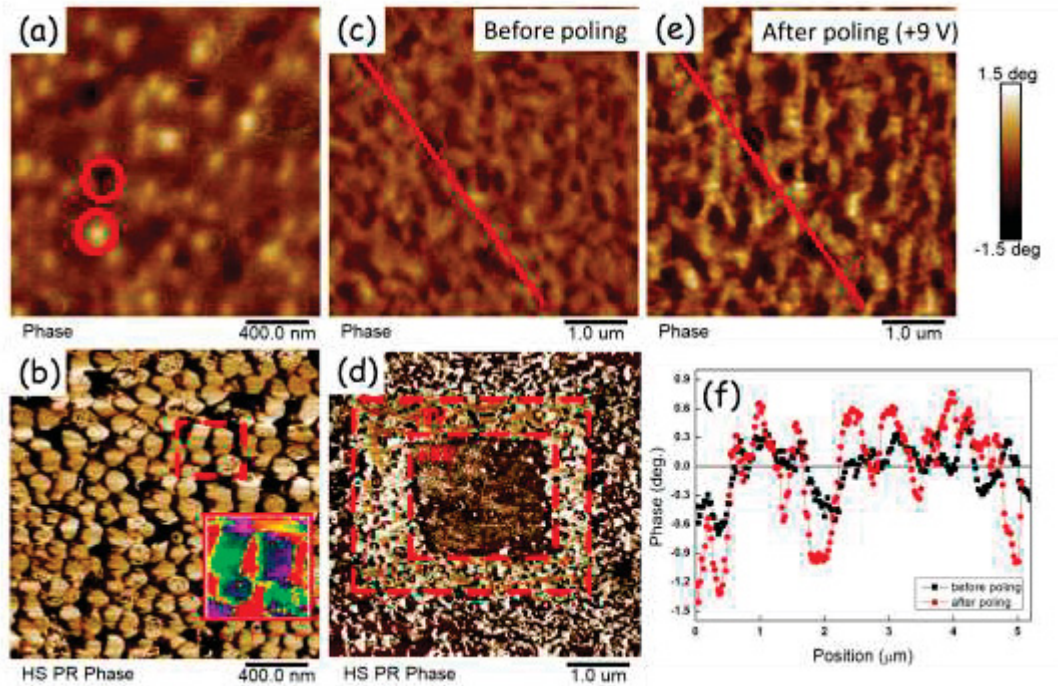

Figure 5.9: (a) (c) (e) MFM and (b) (d) PFM phase images of CFO(7)/BFO(28) nanocomposites. (a) (b) CFO/R-BFO nanocomposite, and (c)-(e) CFO/T-BFO nanocomposite. (f) is the phase profile extract along the red lines in (c) and (e). The inset in (b) is the region in the red box that has a rainbow scale.

5.5. Summary

Epitaxial T-phase CFO/BFO nanocomposites were deposited on (001) LAO single crystal substrates by PLD. Following the post-heat treatment, the nanocomposites developed a platform-like topography, which was different from the CFO/R-BFO nanopillar structure previously reported when deposited on (001) STO. A strong thickness effect of the CFO layer on the coercive field was found, where a 7 nm CFO layer on the T-BFO exhibited a narrow M-H hysteresis loop. The platform T-phase-like CFO contained multiple magnetic domains whose contrast could be tuned by applying a tip bias. These observations can be explained based upon a combination of shape, strain and exchange coupling effects.

Chapter 6. Phase transition and energy storage behavior of epitaxial antiferroelectric PLZT thin films

In the prior sections, different BFO-based ME nanocomposites were investigated. Note that for all nanocomposites, we utilized ferroelectricity (FE) to establish the ME coupling with diverse magnetic kinds (i.e., ferromagnetism, antiferromagnetism, ferrimagnetism). In fact, ME coupling between antiferroelectricity (AFE) and ferromagnetism has been rarely reported, especially as it pertains to thin film (or nanocomposites) [13].

In order to generate the strain-mediated AFE-ferromagnetism ME nanocomposites, epitaxial AFE thin films were required. But little is known about the structure and properties of AFE epitaxial films. To address this scholarly deficit, lanthanum-modified lead zirconate titanate (PLZT) with a composition of 2/95/5 was chosen to fabricate the epitaxial AFE thin films on differently-oriented STO single crystal substrates by PLD. The crystal structure, and phase transition characteristics and pathway from room temperature to 250 ℃ were studied, enabling a more comprehensive understanding of PLZT-based AFE epitaxial thin films. Since AFE materials are useful in the generation of energy storage devices, the energy storage performance of these PLZT thin films was also studied.

In addition, although systematic structural studies of the incommensurate phase in PLZT ceramics of various compositions were reported sometime ago [83,110,111,113,200,201], the effect of epitaxial strain on the incommensurate structure of PLZT thin films has not yet been reported. Given the large c/a ratio difference between the FE and AFE states, one might anticipate significant dependence of the relative AFE/FE stability on epitaxial strain. In Section 6.5, transmission electron microscopy (TEM) was used to study the AFE and FE stability as a function of depth inside PLZT epitaxial thin films. Incommensurate modulations were identified based on various

superlattice reflections in selected area electron diffraction (SAED) patterns, which revealed an orientation-dependent structurally incommensurate distribution.

6.1. Fabrications of PLZT thin films and measurement setup

Thin films of PLZT (2/95/5) were deposited on (100), (110), and (111) STO single crystal substrates by PLD. A hot-pressed PLZT (2/95/5) bulk ceramic disk was used as a target material. Details associated with the hot-press process and the bulk product properties were previously reported [83]. The laser energy density was fixed at 2.25 J/cm^2, and the pulsed repetition rate was fixed at 5 Hz. The oxygen partial pressure was controlled at 150 mtorr, and the deposition temperature was 600 ℃. After deposition, the as-grown films were annealed *in-situ* in a pure O_2 atmosphere of 150 torr at the same temperature for 30 min, and then cooled to room temperature at a rate of 5 ℃/min. The PLZT thin film thickness was set at 300 nm, which was confirmed by cross-sectional SEM measurements.

Surface topology was determined by AFM, and the crystal structure was examined using our XRD system. A pseudocubic index is used when discussing crystal structures in this section. To obtain more structural details of the variously oriented films, RSM was measured along the (002), (022), and (222) zone axes. These XRD and RSM measurements were conducted within a temperature range of 25 ℃ to 250 ℃. The lattice parameters of the films and the substrates were calculated using Equation 2.1. The strain states of the films were obtained by comparing the lattice parameters with those of the bulk.

A homemade Sawyer-Tower system was used to measure the polarization-electric field (P-E) hysteresis loops with increasing temperature from 25 ℃ to 250 ℃. The measurement frequency was 100 kHz. To prevent dielectric breakdown, the maximum E-field was kept below 1000 kV/cm in the low temperature range, and below 780 kV/cm in the high temperature range. The breakdown

E-field was near E=1500 kV/cm at room temperature. To measure the P-E loops, a 30-nm-thick SRO buffer layer was deposited between the PLZT layer and substrate by PLD, which then served as the bottom electrode. Platinum point electrodes (40 μm×40 μm) were sputtered on the top surface using a Leica EM ACE600 sputter coater.

From the P-E loops, the energy storage density (ESD or U_r), energy loss density (ELD or U_{loss}), total energy density, and energy storage efficiency (ESE or η) were determined by Equations 1.2 through 1.5, respectively. To reduce uncertainty, the final P-E loops shown in this section were averaged from 20 continuous loops, among which every individual loop had no notable difference from each other. However, it should be pointed out that losses and efficiencies calculated from P-E loops can be sensitive to measurement conditions to some extent.

The TEM specimens were prepared by a standard mechanical polishing process, followed by argon ion milling (Fischione Model 1010) to perforation. The TEM studies were performed on a JEOL 2100 microscope operating at a voltage of 200 kV. The aperture used for the local SAED was about 100 nm. The selected region was moved perpendicularly from the surface (set as the zero point) to the interface, allowing depth profiling. The lattice parameters were calculated based on the distance between the reflections along the different directions. For reflections exhibiting diffused streaking, measurements were performed between the points with the highest intensity. The superlattice reflections can be expressed as:

$$h\,a^* + k\,b^* + l\,c^* \pm \frac{1}{n}(b^* + c^*), \qquad 6.1$$

where a*, b*, c* are reciprocal base vectors; h, k, l are Miller indices, and the value of n is the modulation period number that can be used to derive the modulation wavelength [202].

6.2. Surface topography

The AFM height images are shown in Figure 6.1a-c, which exhibit relatively smooth and dense surface morphologies with a roughness of ~2 nm. The surface topography indicated a columnar-like growth mode rather than the layer-by-layer mode, which was confirmed by the cross-sectional SEM images in Figure 6.1d-f.

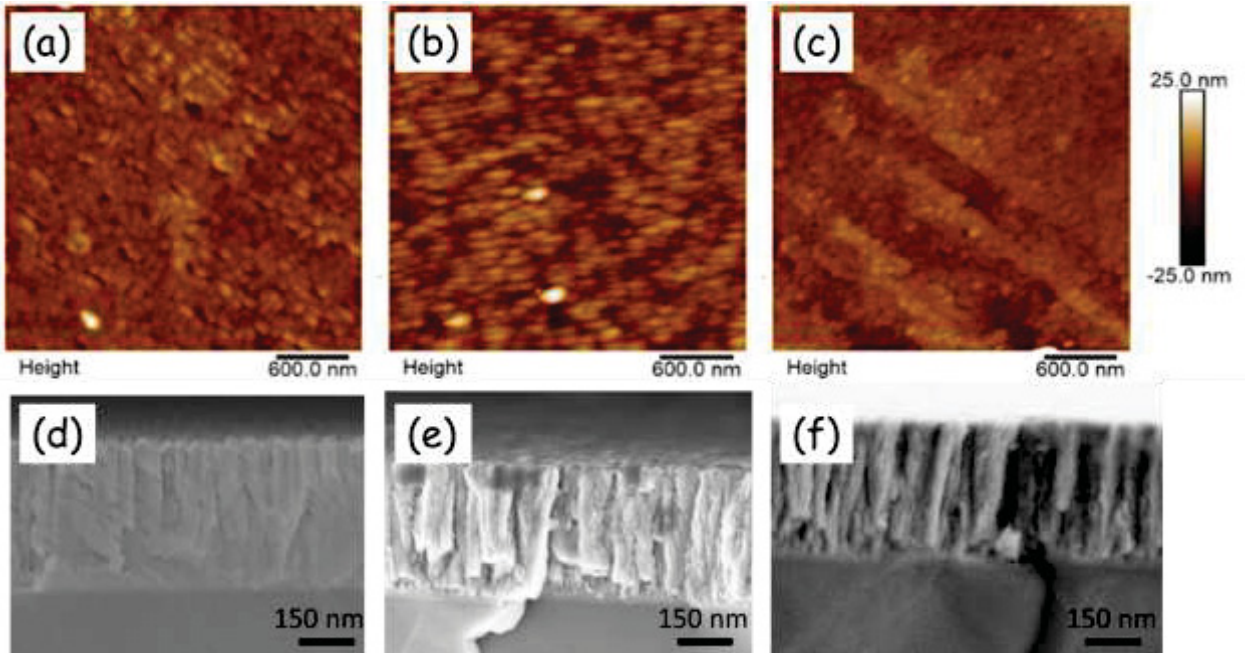

Figure 6.1: (a)-(c) AFM height images and (d)-(f) cross-sectional SEM images of (a) (d) PLZT on (001) STO, (b) (e) PLZT on (011) STO, and (c) (f) PLZT on (111) STO.

6.3. Standard structural studies

Figure 6.2 provides XRD line scans for the PLZT films on (100), (110), and (111) STO substrates. Well-distinguished PLZT and SRO peaks can be seen, indicating good epitaxial quality without any noticeable second phase signals. Figure 6.3 shows 360° phi scans which were taken to determine the in-plane (IP) epitaxial relationship between the PLZT films and the STO substrates. The peaks of the PLZT films were at the same positions as those of the STO substrates,

which also proved the good epitaxy of the films. For the (001), (011), and (111) PLZT films, the epitaxial relation was (001)[100]PLZT//(001)[100]SRO//(001)[100]STO, (011)[100]PLZT//(011)[100]SRO//(011)[100]STO, and (111)[1-10]PLZT//(111)[110]SRO// (111)[1-10]STO, respectively.

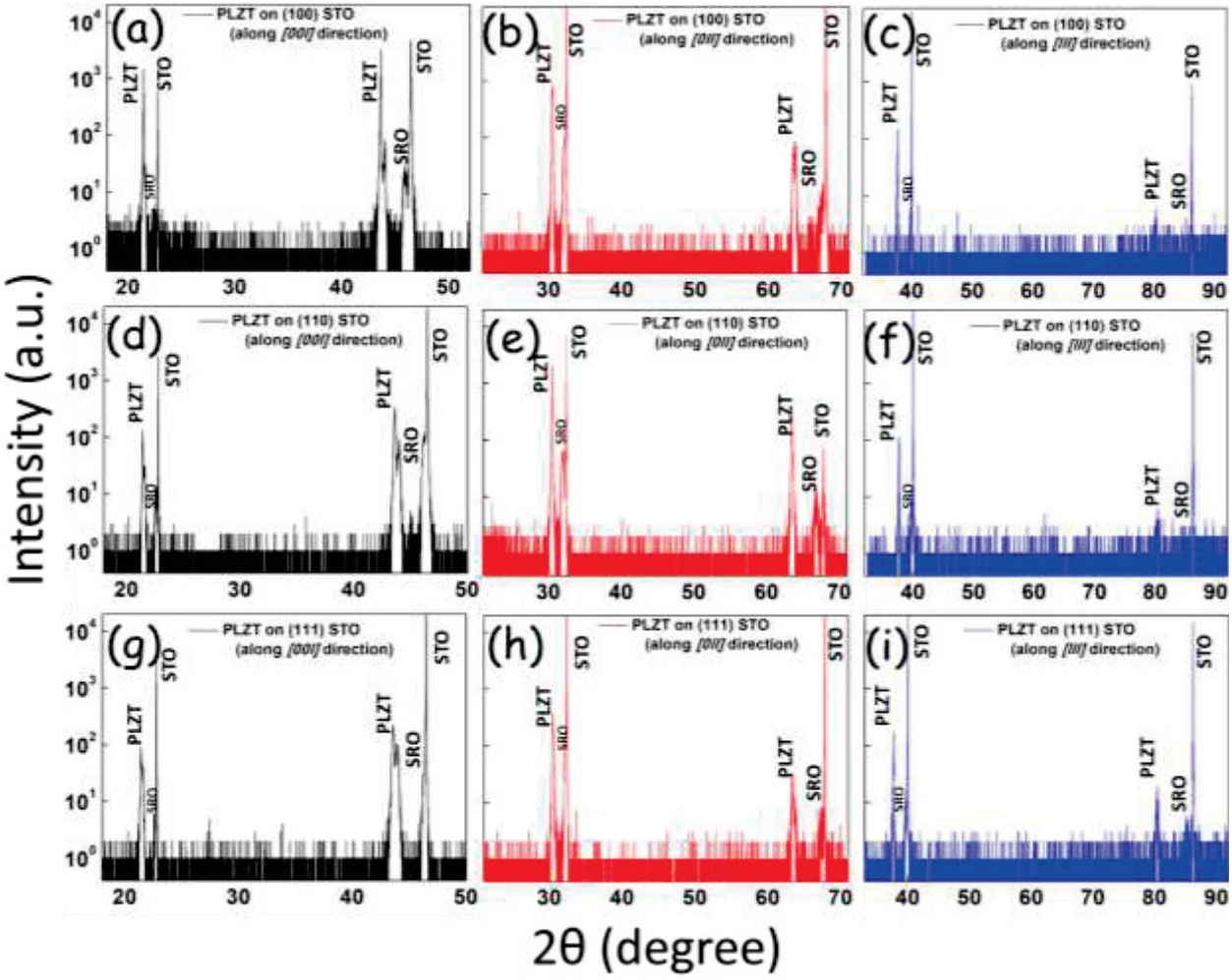

Figure 6.2: XRD line scans of 300 nm PLZT thin films on (a)-(c) (100) STO, (d)-(f) (110) STO, and (g)-(i) (111) STO. The zone axis is along the (00l) direction in (a) (d) (g); along the (0ll) direction in (b) (e) (h); and along the (lll) direction in (c) (f) (i).

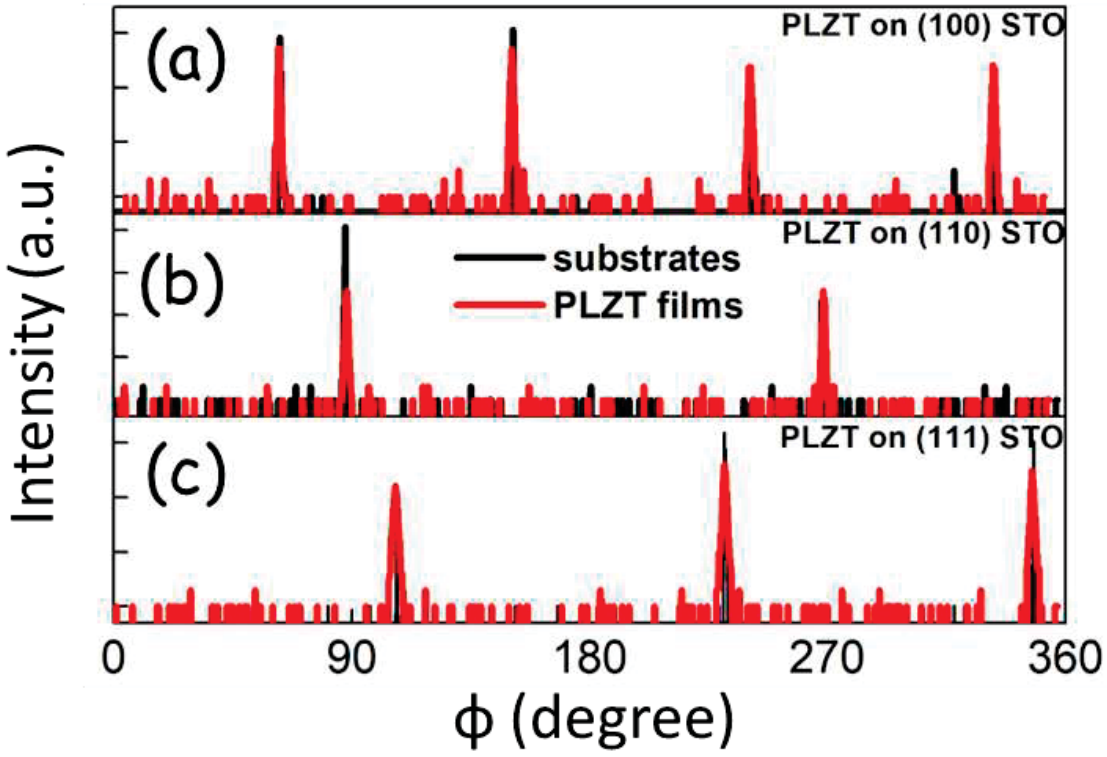

Figure 6.3: XRD φ scans of 300 nm PLZT thin films on (a) (100) STO, (b) (110) STO, and (c) (111) STO substrates.

To obtain more detailed structural information, RSM mesh scans were taken after careful calibrations, as shown in Figure 6.4. By combining them with the XRD line scans, one can more easily determine the crystal structure and the strain condition. For (001) PLZT, doublet peaks along both the (002) and (022) zone axes were identified, indicating a T structure with 90° twin domains, where the c-domain population was dominant over the a-domain [203]. This domain configuration formed because it had a homogeneous IP compressive strain of -0.50% along the <100> and <010> directions, caused by a large IP lattice mismatch of -6.27% between the PLZT film (a=c=4.15 Å, b=4.11 Å for bulk PZT 95/5 [89]) and STO substrate (3.905 Å). Previously, Lu et. al. reported that PZT (95/5) films on (100) STO had an orthorhombic structure, similar to the bulk form, with a

two-fold symmetry [89]. However, our results are notably different, as the φ scans (see Fig. 6.3) clearly evidenced a four-fold symmetry. This difference is likely due to the fact that their films were thicker; thus, the epitaxial strain was capable of being fully relaxed.

For (011) and (111) PLZT films, a doublet splitting along the (002) zone axis and a triplet along the (022) zone axis were found, which were signatures of a monoclinic type-A (M_A) crystal structure [157]. The origin of the M_A structure may be due to an inhomogeneous IP strain that tilts the c axis by a small angle: 0.37 ° on (110) STO, and 0.5 ° on (111) STO. The IP strains for the (011) PLZT were oriented along the <011> and <100>, with values of -0.37% and -0.89%, respectively. Similar analysis was applied to the (111) PLZT film. A difference about the (222) zone was found between the (011) and (111) films. The (111) film had a sharper (222) peak than the (110) one, which indicated the former had a more uniform crystal structure along the (111) direction (its epitaxial growth direction).

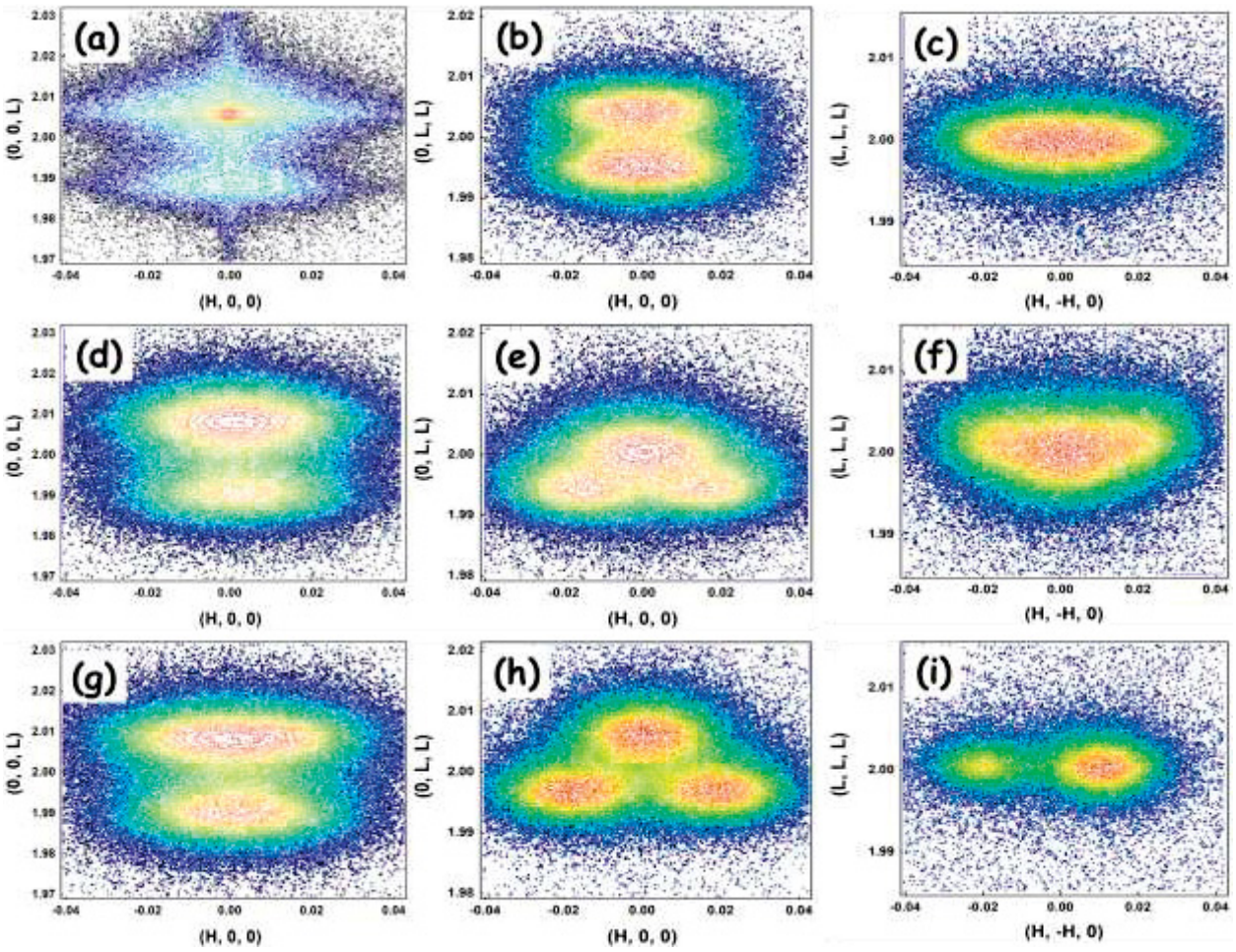

Figure 6.4: RSM images of (a)-(c) (001) PLZT film, (d)-(f) (011) PLZT film, and (g)-(i) (111) PLZT film. (a) (d) (g) were taken along the (002) zone axis; (b) (e) (h) along the (022) zone axis; and (c) (f) (i) along the (222) zone axis.

6.4. Temperature dependent phase transitions and energy storage performances

6.4.1. Room temperature P-E characteristics and energy storage performances

Figure 6.5a-c illustrates the room temperature bipolar P-E loops for all three samples taken at various maximum E-fields. The asymmetry of the electrodes (bottom: SRO; top: Pt) resulted in loop drifting, as reported in several prior PZT film studies [204,205]. Figure 6.5d-f provides the calculated ESD and ESE values as a function of E. Under low E-fields (E≤280 kV/cm), all three

samples exhibited typical AFE loops with a small remanent polarization, low P-E loop areas (i.e. low loss), and hence a relatively high ESE. As the maximum E was increased, a critical field E_{FE} was reached, where the AFE→FE phase transition was induced. For the (001), (011), and (111) PLZT films, the values of E_{FE} were determined by calculating the inflections of the loops, which were about 330 kV/cm, 320 kV/cm, and 285 kV/cm, respectively. Please note that measurements were carried out only along the OP direction, which was the [001] for (001) PLZT, [011] for (011), and [111] for (111). For the bulk PZT samples, the sub-lattice interaction of the AFE phase was along the <110> direction. The easy axis of the spontaneous polarization was along [001] direction for T structure, and along the (110) plane for M_A (see Fig. 1.5a). In the bulk materials, the AFE→FE transition resulted in a O→R phase transition, where the easy polarization axis of R was along $(111)_{pc}$. These observations, along with the strain effects, may explain the differences in the E_{FE} values [102,206].

Remanent polarizations data for the (001), (011), and (111) PLZT films were about 16 $\mu C/cm^2$, 34 $\mu C/cm^2$, and 17 $\mu C/cm^2$, respectively. These values were notably larger than that of bulk AFE PLZT samples, indicating a higher tendency to retain an FE order at zero E-field after the AFE→FE transition has been induced [103,207]. This result may be due to the film/electrode interface layer, and/or residual stress/strain condition [208-210]. Normally, such effects are thickness dependent [208]. However, one cannot exclude the influence from the observed T or M_A phase, considering that PZT films with a T or M_A phase exhibit FE characteristics. The saturation polarizations of all three films were exceptionally high, having values of about 70 $\mu C/cm^2$, which will enable higher ESD values. From the shape of the P-E loops, it can be seen that the (111) PLZT featured the steepest slope at the inflection point, relative to either (001) or (011). Correspondingly,

Figure 6.5d-f show that (111) PLZT had the highest ESD (~40 J/cm^3) and ESE (~53%) values, compared to (001) PLZT (~27 J/cm^3, ~40%) and (011) PLZT (~16 J/cm^3, ~22%).

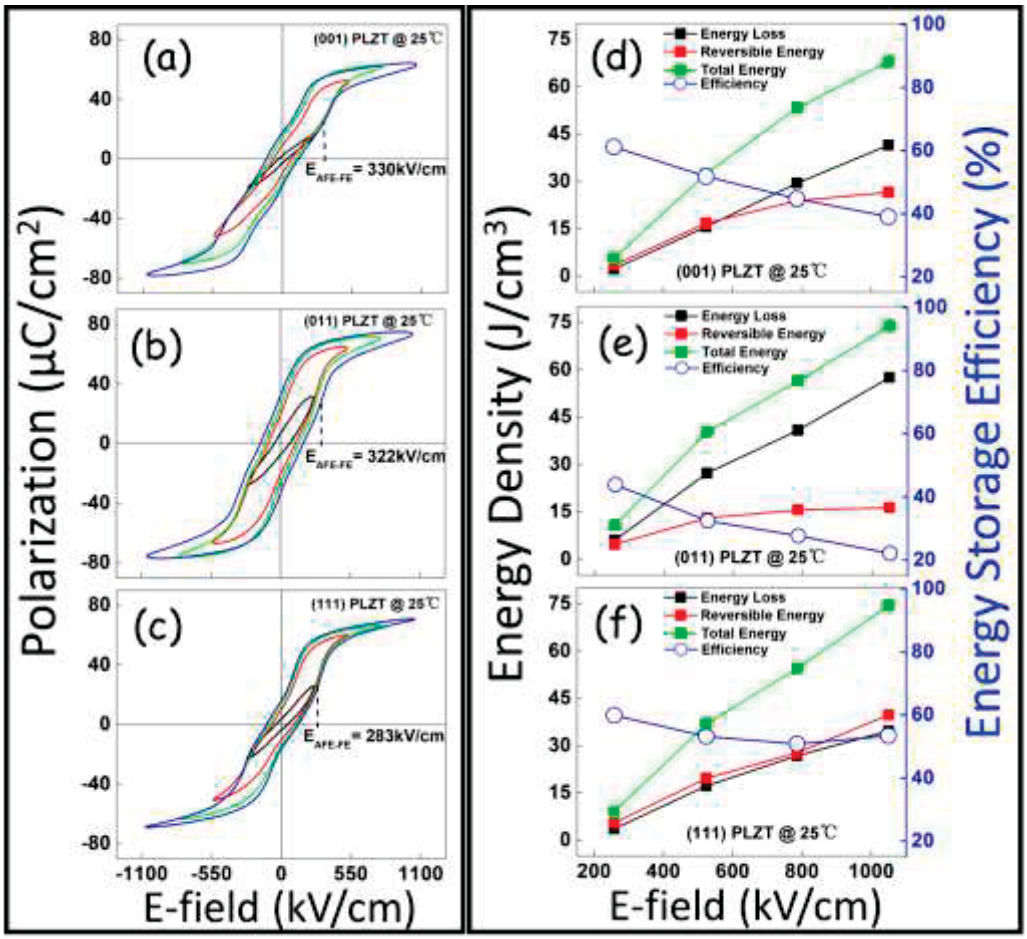

Figure 6.5: P-E loops of (a) (001) PLZT, (b) (011) PLZT, and (c) (111) PLZT at room temperature with increasing E-fields. (d)-(f) show the corresponding energy density and ESE values calculated from (a)-(c).

Figure 6.6 show the frequency (f) dependent P-E loops taken at room temperature. The curves were stable for 10 kHz≤f≤100 kHz in all three oriented films, which show their capability of functioning within the frequency range of typical pulsed capacitor devices [100]. The changes in the P-E loops at lower frequencies are probably caused by leakage currents with decreasing AC

frequencies [211]. Since our samples were more stable at higher frequencies, these measurements were all obtained at 100 kHz.

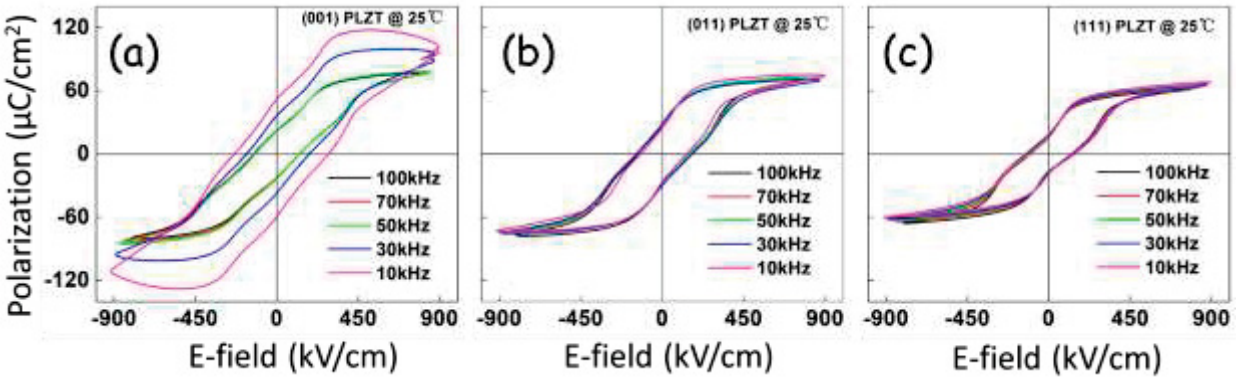

Figure 6.6: P-E loops of (a) (001) PLZT, (b) (011) PLZT, and (c) (111) PLZT at room temperature at various frequencies between 100 kHz and 10 kHz.

6.4.2. Dependence of structures, dielectric properties, and energy storage behaviors on temperature

Next, the P-E loops were measured at various temperatures on heating from 25 ℃ to 250 ℃, with results revealing an AFE/FE→RFE transition in each case. A panel of selected P-E loops is shown in Figure 6.7. These data demonstrate that the pinched P-E loops with significant hysteretic area became slim loops with increasing temperature. The slim loops are indicative of RFE characteristics. Note that while the details of these P-E loop changes were different for (001) PLZT relative to the other two, the generalities were the same. For (001) PLZT, a pinched AFE/FE P-E loop became a slim (RFE) loop on heating from 70 ℃ to 100 ℃. Conversely, for the (011) and (111) PLZT films, the pinched AFE/FE loops first transited to typical FE loops on heating (50~70 ℃ for (011) PLZT, and 100~125 ℃ for (111) PLZT), and then gradually evolved into slim (RFE) loops with further increases in temperature.

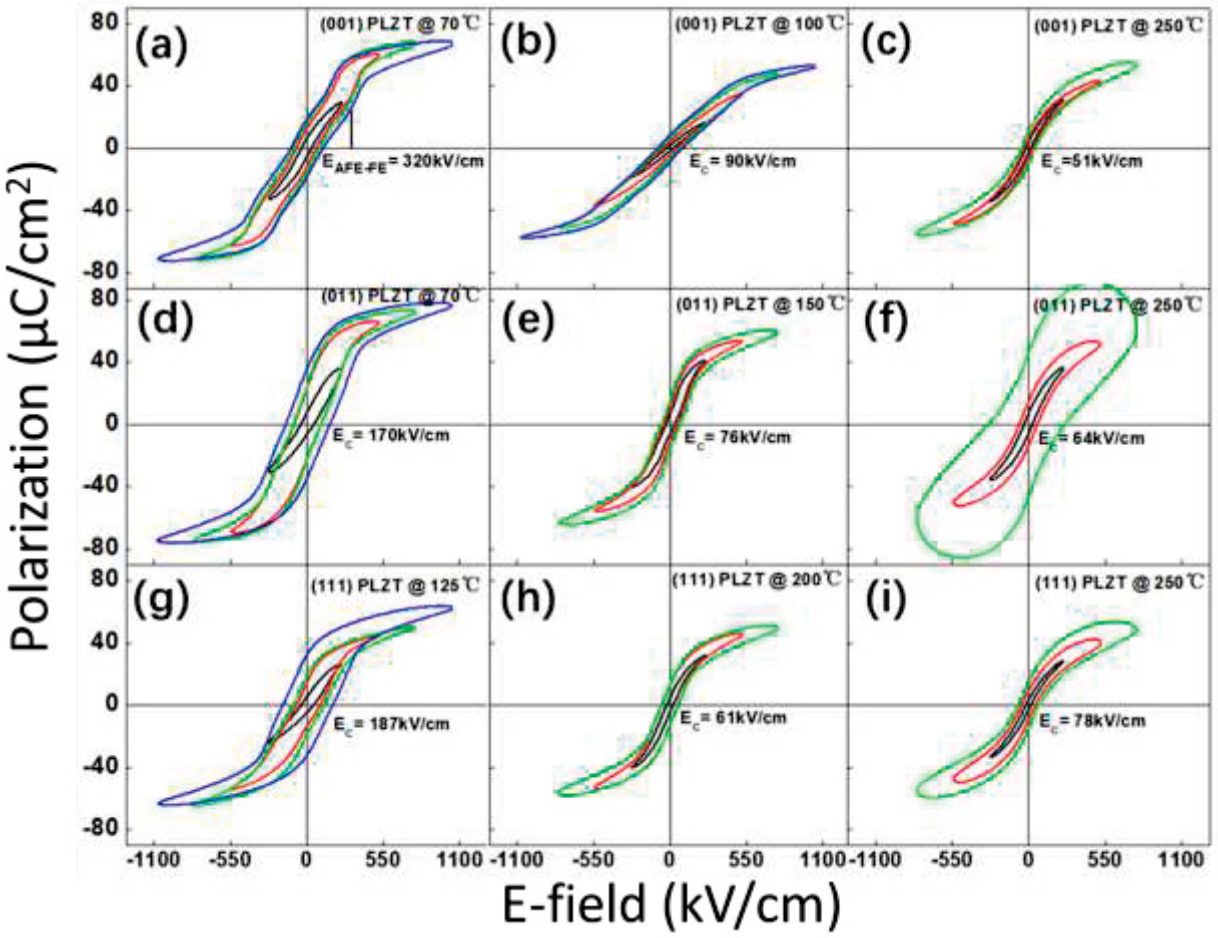

Figure 6.7: P-E loops of (a)-(c) (001) PLZT, (d)-(f) (011) PLZT, and (g)-(i) (111) PLZT measured at various temperatures that reveal different ferroelectric phase stabilities: (a) AFE; (d), (g) FE, and others are RFE. The wider loops in (f) and (i) were caused by leakage currents.

After reaching the slim loop (RFE phase) state, their coercivity (E_C) was continuously reduced with increasing temperature to 250 ℃, as can be seen in Figure 6.8. This gradual decrease in E_C is typical of a diffuse transformation from FE to paraelectric (PE) phases [90,212]. We want to note that the phase transition sequences here were determined on the basis of the qualitative shape change of the hysteresis loops, associated with the decrease in coercivity. As such, additional temperature dependent dielectric constant measurements may be helpful to precisely identify the

phase transition points. Fig. 6.7 also evidences that the PLZT films remained in the RFE phase until reaching a temperature of 250 °C, demonstrating that the Curie temperature range was increased to higher temperatures compared to the bulk (about 230 °C [83]). This trend can be attributed to epitaxial strain effects, which may stabilize the polar phase to higher temperatures, thereby potentially extending the working range of the RFE phase of PLZT films [211,213].

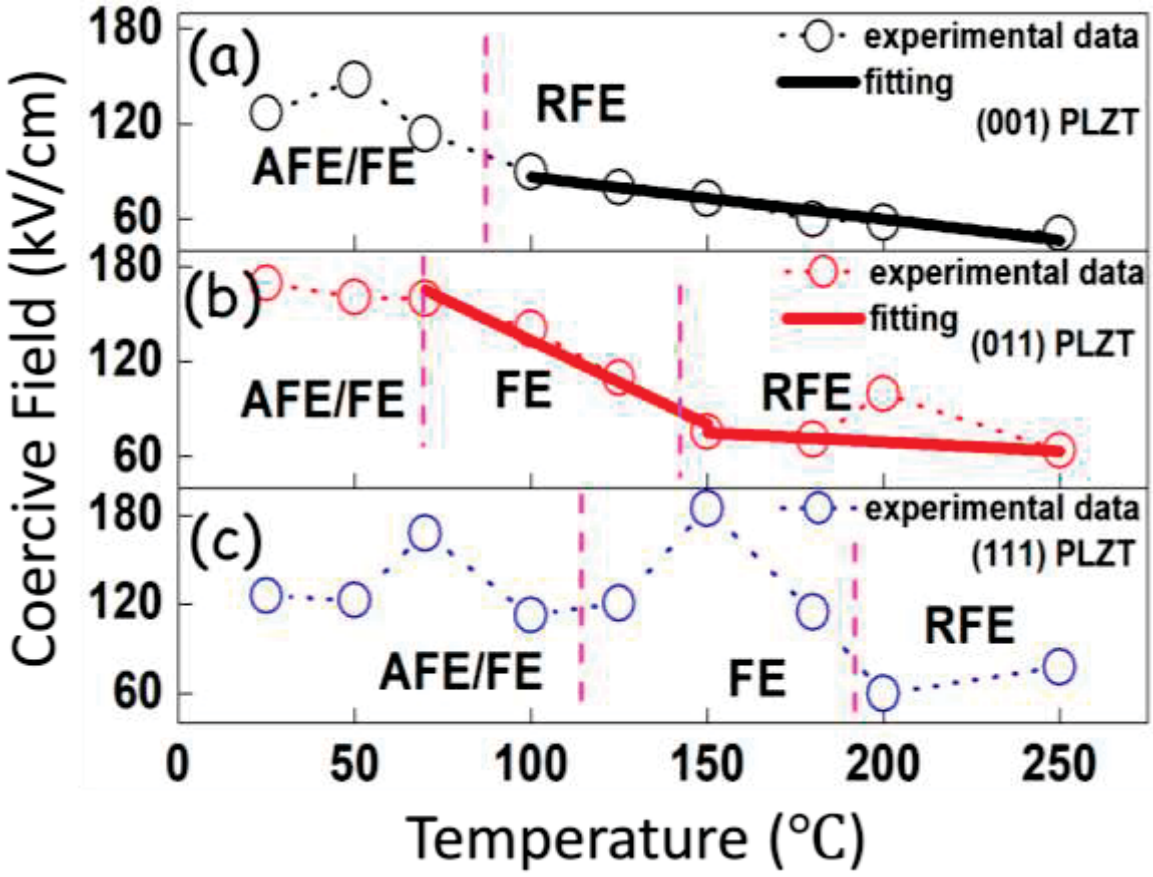

Figure 6.8: Coercive field of (a) (001) PLZT, (b) (011) PLZT, and (c) (111) PLZT as a function of the temperature. Dotted lines refer to experimental data, while solid lines indicate the fitting results. The purple dashed lines separate different phase regions based on their P-E loop characteristics.

Values for the ESD, ESE, and remanent polarization were calculated from the P-E loops. The results are summarized as functions of both temperature and E in Figure 6.9. The saturation

polarization, ELD, and total energy density are given in Figure 6.10. Similar phase transition trends were identified for the three samples. For E≤600 kV/cm, all three samples exhibited relatively stable ESD values over the temperature range of 25 ℃ to 250 ℃. The Small changes that were observed can be attributed to increased leakage currents caused by higher oxygen vacancy mobility at higher temperatures. In contrast, under higher E the three samples exhibited definite changes in ESD, which can be explained by differences in their phase transformational pathways, as discussed above. For the (001) PLZT, as the temperature was increased, the ESD value was slightly decreased in the AFE/FE region. It then increased from 20 J/cm^3 to 35 J/cm^3 above the AFE/FE→RFE transition, and remained relatively high with further increases in temperature in the RFE region. For the (011) PLZT, the value of ESD decreased with increasing temperature in the AFE/FE→FE transformational region from 18 J/cm^3 to 15 J/cm^3, and then increased back to 18 J/cm^3 upon heating into the FE→RFE transition range. Similar to the (011) film, the (111) PLZT film exhibited a similar general trend with increasing temperature as for the (011) film—although its values of ESD were higher. Initially, the ESD for the (111) PLZT film decreased dramatically from 40 J/cm^3 to 17 J/cm^3 upon heating into the AFE/FE→FE transitional region. This value remained low upon heating until 180 ℃ within the FE region, but then increased to 25 J/cm^3 upon further heating to 250 ℃ in the RFE region.

The value of ESE (see Fig. 6.9d-f) exhibited an opposite trend to that of the remanent polarization (see Fig. 6.9g-i). This finding indicates that the efficiency is affected not only by ESD, but also by the energy losses during a charge/discharge cycle, which is strongly related to the samples' remanent polarization. Accordingly, in the FE region, the (011) and (111) PLZT films displayed notably lower efficiencies, whereas in the other phase regions, the efficiencies of these three samples remained high. The drop in efficiency at higher temperatures and higher E-fields is

probably due to increased leakage currents. Fig. 6.9 summarizes the proper working temperature ranges for the differently oriented PLZT films in terms of the highest ESD and ESE values: 70~200 ℃ for (001) PLZT (25~35 J/cm^3, 50~70%), 150~200 ℃ for (011) PLZT (12~18 J/cm^3, 30~50%), and both 25 ℃ to 70 ℃ and 200~250 ℃ for (111) PLZT (20~40 J/cm^3, 30~55%).

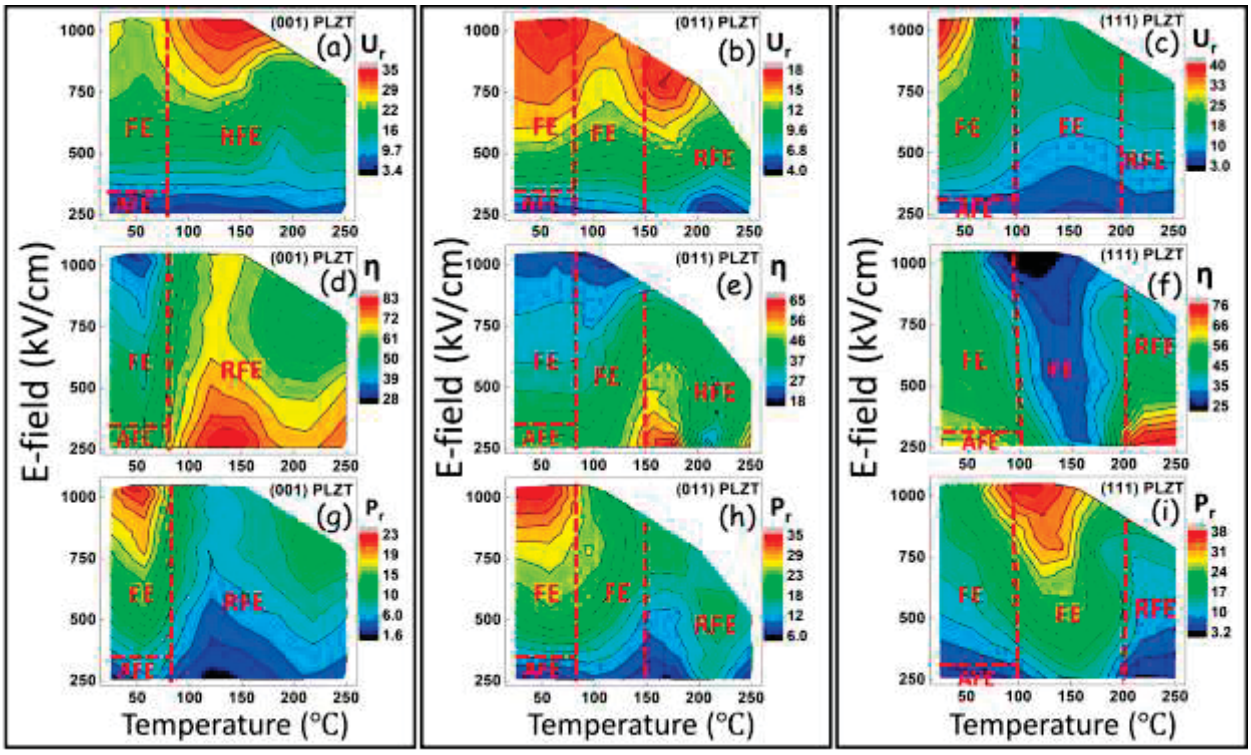

Figure 6.9: (a)-(c) ESD (J/cm^3), (d)-(f) ESE (%), and (g)-(i) remanent polarization (μC/cm^2) of oriented PLZT films as functions of both E and temperature. (a) (d) (g) (001) PLZT, (b) (e) (h) (011) PLZT, and (c) (f) (i) (111) PLZT. Different phase regions are marked by red dashed lines in each figure.

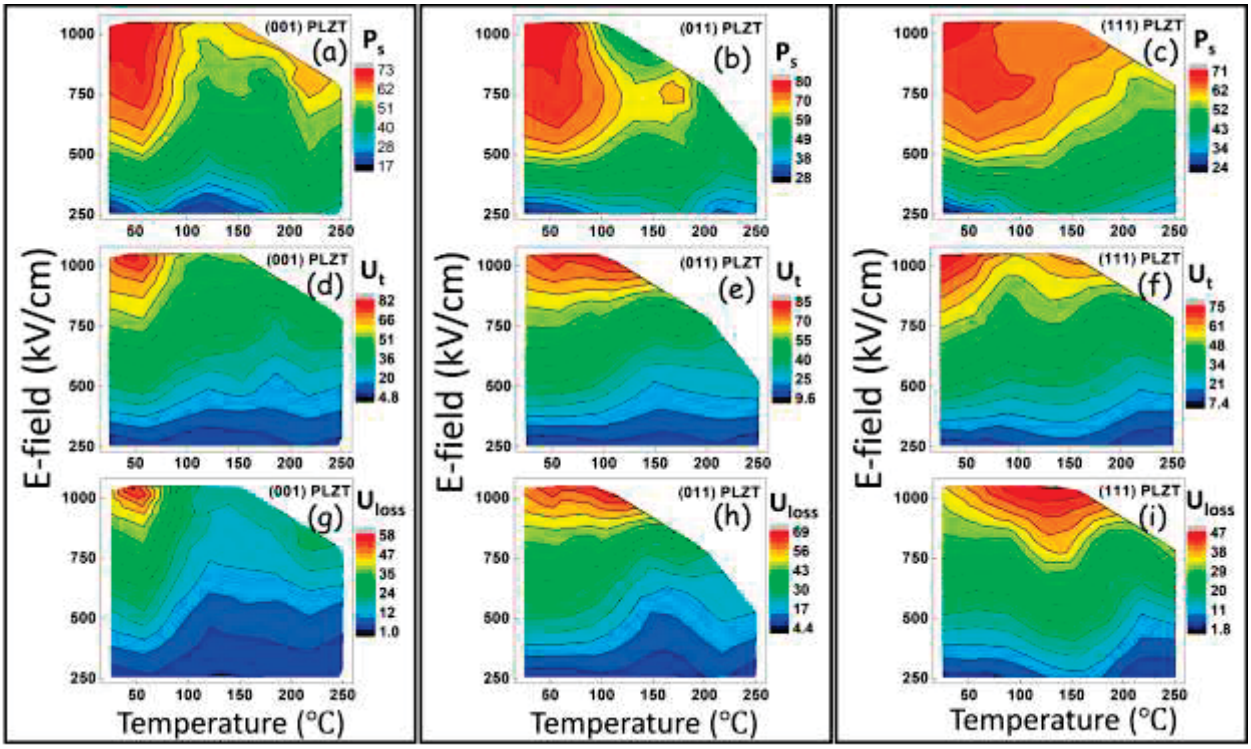

Figure 6.10: (a)-(c) Saturation polarization (μC/cm^2), (d)-(f) total energy density (J/cm^3), and (g)-(i) ELD (J/cm^3) of oriented PLZT films as functions of both bipolar E and temperature. (a) (d) (g) (001) PLZT, (b) (e) (h) (011) PLZT, and (c) (f) (i) (111) PLZT.

Temperature variable XRD data were then obtained to determine the crystal structure and lattice parameter changes. XRD line scans (see Figure 6.11a-b) show that the low-angle side of the PLZT peaks did not change much with increasing temperature. Rather, the high-angle side of the peaks continuously shifted to smaller 2θ values with increasing temperature, and finally merged with the low-angle peaks near 250 °C. The RSM scans confirmed that the crystal structure did not change for any of these films over the temperature range investigated (see Figure 6.11c-f). The temperature dependence of the lattice parameters for both PLZT and STO are shown in Figure 6.11g-i. The lattice parameter of STO was linearly extended with increasing temperature due to thermal expansion, which may have served to partially relax the lattice mismatch between the

substrates and the films, thereby reducing the IP strain of the PLZT layers. No evidence of sudden changes in the c/a ratio of the PLZT films was observed until temperatures exceeded 200 ℃. Conversely, the value of c/a gradually approached 1 as the temperature was increased towards 250 ℃. Temperature variable XRD results indicate that the changes in P-E characteristics with temperature discussed above can be attributed to a reduction in tetragonality or monoclinicity, which are more likely strain-induced transitions rather than symmetry-related ones [214].

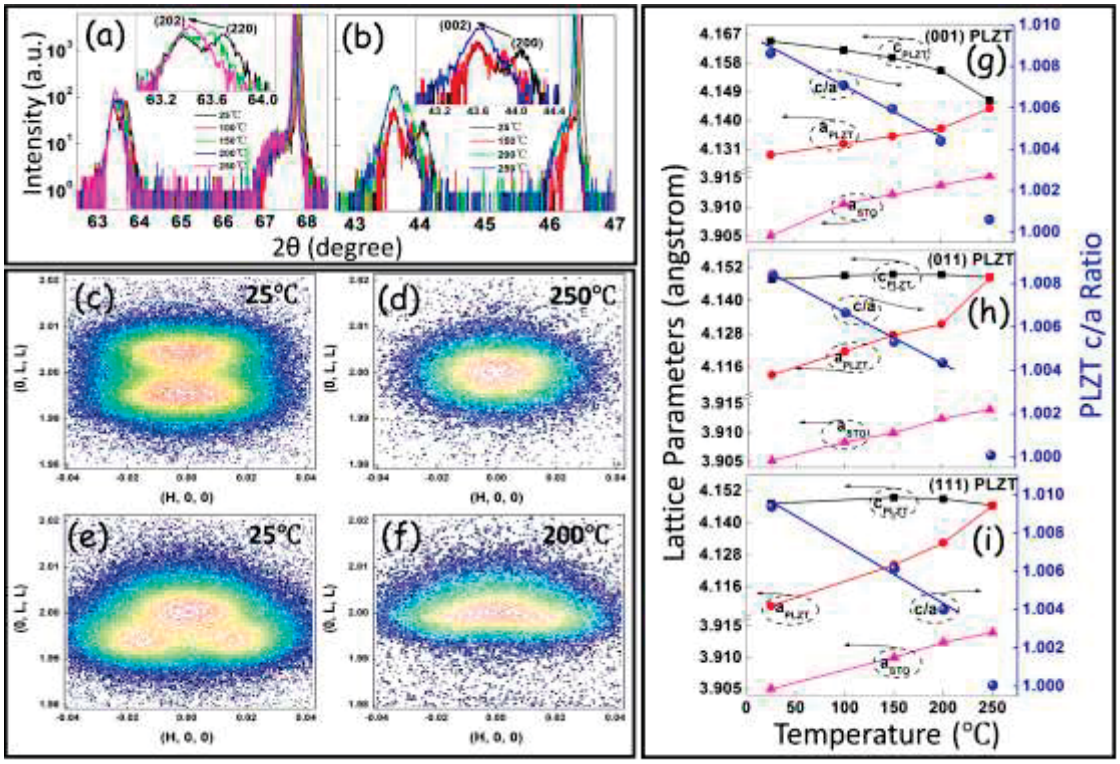

Figure 6.11: Temperature dependent XRD patterns of (a) PLZT/SRO on (001) STO, and (b) PLZT/SRO on (111) STO. Parts (c)-(f) RSM images of (c), (d) (001) PLZT; and (e), (f) (011) PLZT. The zone axis is along the (022) in (a), (c)-(f); and along the (002) in (b). (g)-(i) Calculated lattice parameters of STO substrate (a_{STO}) and PLZT film (a_{PLZT}, c_{PLZT}), as well as the c/a ratio of PLZT, as a function of temperature. The orientations of the substrate in (g), (h), and (i) are (100), (110), and (111), respectively. The c/a ration of PLZT was linearly fitted to temperature in the range of 25 to 200 ℃.

6.4.3. Unipolar drive and improved energy storage characteristics

The PLZT films featured a mixed AFE/FE phase stability, after bipolar drive, as evidenced by the large P_r values for E=0. Thus, on reversal of applied E-field, the polarization rotation in the FE regions may consume more energy, which, in turn, diminishes the ESE. In domain-engineered piezoelectric crystals, the unipolar drive has been shown as an effective way to decrease both hysteretic losses and energy consumption [109]. Furthermore, under unipolar drive, since the polarity of E does not switch, defects such as oxygen vacancies will not continuously migrate. Thus, fatigue limits for high-frequency charging/discharging cycles will improve, and thereby, reducing the unwanted degradation in ESE values due to the leakage current [108].

As shown in Figure 6.12a-c, under unipolar drive, the remanent polarization was noticeably smaller than those under bipolar drive. At the same time, the unipolar-driven ESD values (see Fig. 6.12d-f) were considerably more stable in comparison to the bipolar ones over the entire temperature range studied. The maximum ESD values were about 19 J/cm^3, 15 J/cm^3, and 17 J/cm^3 for the (001) PLZT, (011) PLZT, and (111) PLZT, respectively. These values are comparable to the bipolar results, when considering the fact that the unipolar cycle was half of the bipolar cycle. Due to the lower remanent polarization values in the unipolar cases, the ESE values in Fig. 6.12g-i were significantly higher than the bipolar ones, in particular for the (011) film. The efficiency at the maximum ESD value reached 77%, 60%, and 70% for the (001), (011), and (111) PLZT, respectively. All three samples exhibited a gradual AFE/FE-RFE transformation with increasing temperature.

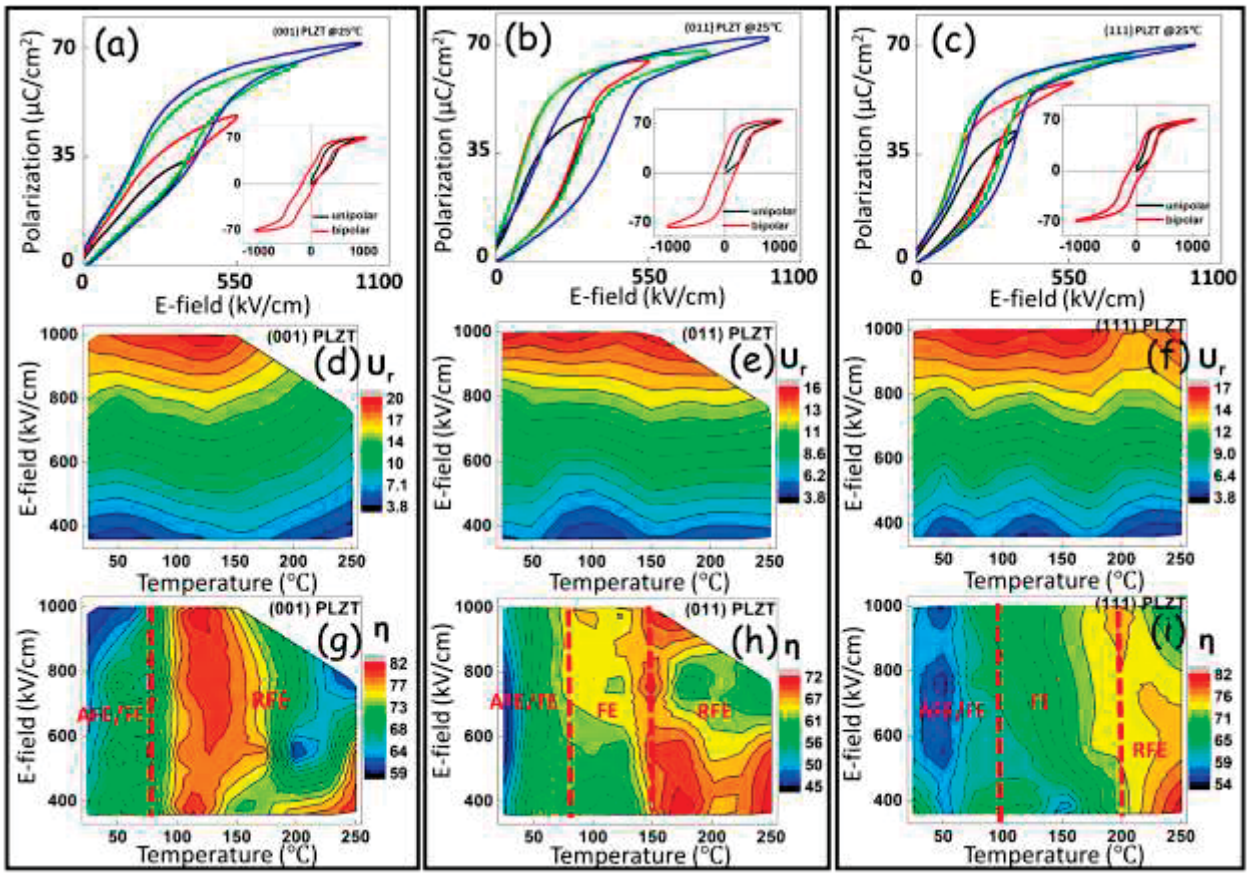

Figure 6.12: Unipolar P-E loops of (a) (001) PLZT, (b) (011) PLZT, and (c) (111) PLZT. The insets exhibit a comparison between unipolar and bipolar loops. (d)-(f) and (g)-(i) are the corresponding ESD (J/cm^3), and ESE (%), respectively. The red dashed lines in (g)-(i) divides the different phase regions based on the bipolar result characteristics.

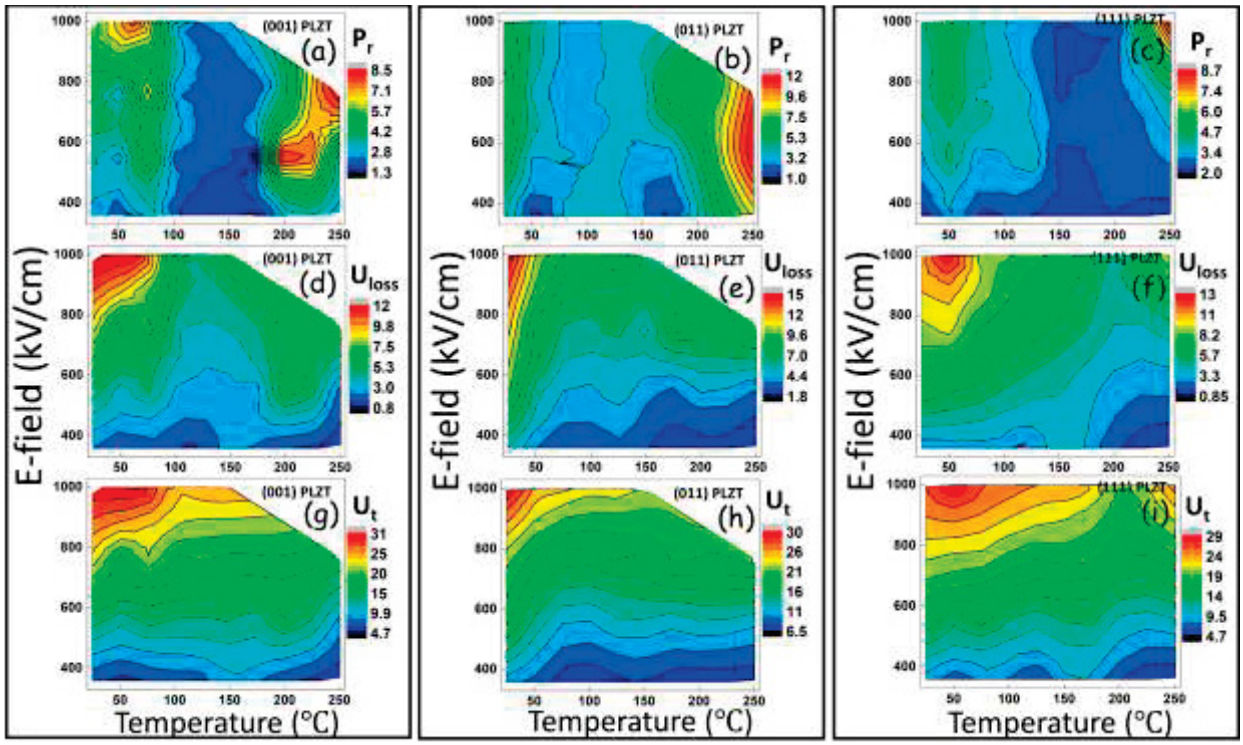

Figure 6.13: (a)-(c) Remanent polarization (μC/cm^2), (d)-(f) ELD (J/cm^3), and (g)-(i) total energy density (J/cm^3) of oriented PLZT films as functions of both unipolar E and temperature. (a) (d) (g) (001) PLZT, (b) (e) (h) (011) PLZT, and (c) (f) (i) (111) PLZT.

With respect to potential industrial applications, fatigue limit tests of these PLZT films revealed that the energy storage performance characteristics could be maintained after 10^8 charging/discharging cycles under a maximum field of 765 kV/cm and at room temperature, as shown in Figure 6.14. These findings differ from those obtained for induced AFE→FE transitions in bulk, where large c/a ratio changes resulted in rapid deterioration of the samples' mechanical strength with cycling. Clearly, the unipolar drive may be a promising way to enhance the energy storage capability of AFE thin film materials for pulsed capacitors.

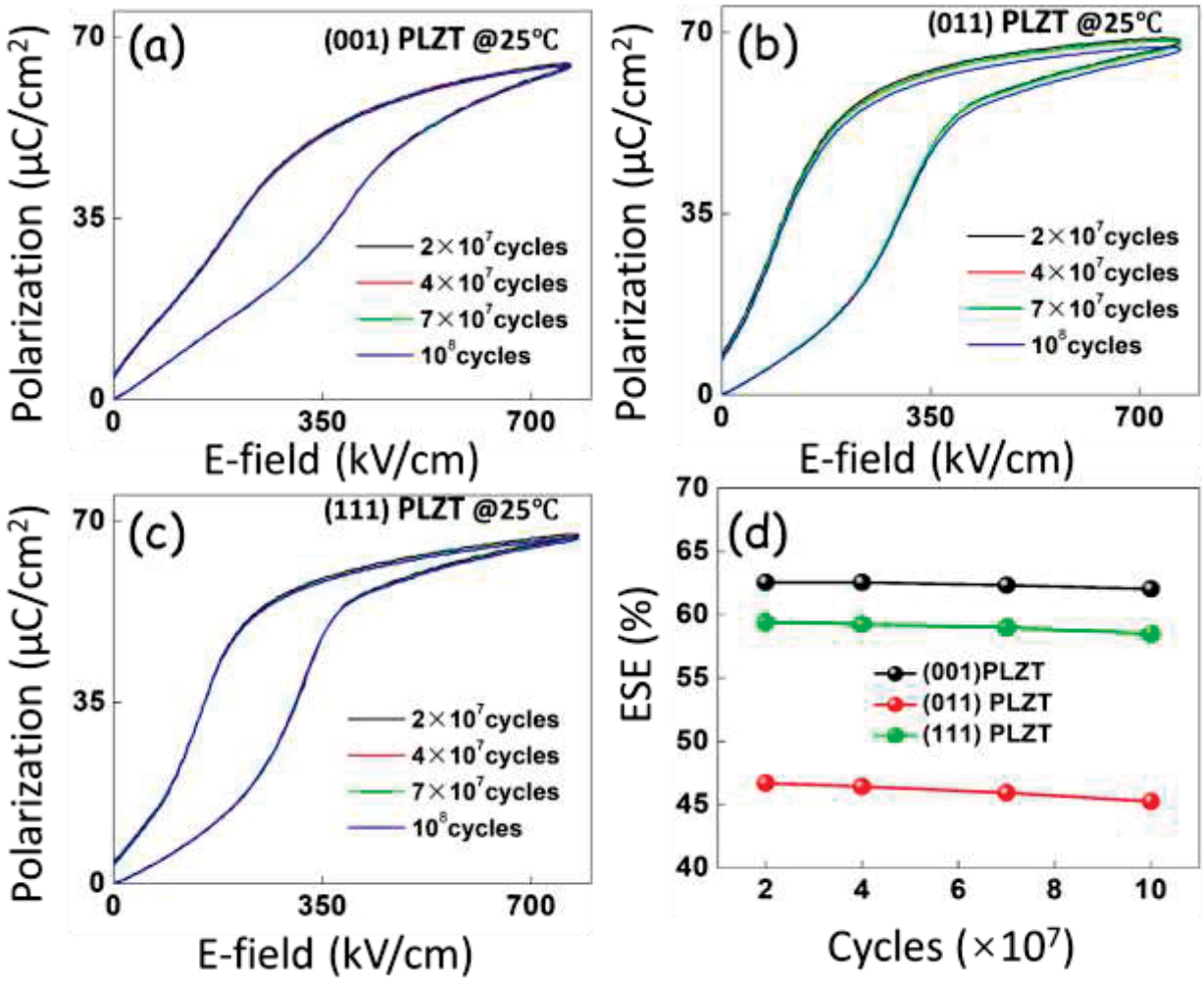

Figure 6.14: Unipolar P-E loops of (a) (001) PLZT, (b) (011) PLZT, and (c) (111) PLZT at room temperature with increasing numbers of charge/discharge cycles. (d) is the calculated energy storage efficiency as a function of the running cycles.

6.4.4. Discussion on temperature dependent structural and dielectric phase transitions

Intermediate T phases have previously been reported in $PbZrO_3$ ceramics and crystals [83,215], which have been found only over narrow temperature ranges (about 5 °C) sandwiched between the cubic (C) and AFE orthorhombic (AFE_O) phases. It has remained controversial whether this T phase is stable or metastable, and whether it features FE or AFE order [83,85,216,217]. Previous studies

by Dai et al. revealed ferroelectric P-E hysteresis loops in this intermediate phase field [83]. Here, our findings for (001) PLZT (2/95/5) demonstrate that both the AFE_T and FE_T phases can be stabilized by epitaxial strain. The phase transformational sequence on heating is then $AFE_T \rightarrow RFE_T \rightarrow C$. Furthermore, a new monoclinic M_A phase region has been found in high Zr-content PLZT, which was previously unknown. Our data demonstrate that (011) and (111) PLZT (2/95/5) has both AFE_{MA} and FE_{MA} phases that are stabilized by epitaxial strain. The phase transformational sequence on heating is then $AFE_{MA} \rightarrow FE_{MA} \rightarrow RFE_{MA} \rightarrow C$. Clearly, the phase stability on the AFE side of the PLZT (and PZT) systems can be significantly altered by epitaxial engineering.

The fact that the crystal structure remains either T or M_A during the AFE→FE transition results in the transformational strains being negligible compared to that for bulk samples. Correspondingly, the energy storage efficiency does not degrade with repeated cycling of the field for $\geqslant 10^8$ times, and the film remains mechanically robust.

Heating in all cases resulted in an AFE→FE transition. Further increase in temperature within the FE phase region resulted in slim hysteresis loops, typical of RFE. Slim P-E hysteresis loops have previously been reported at elevated temperatures in Sn-doped PZT (PZST) [17,206], and PLZT ceramics that undergo an $AFE_O \rightarrow FE_R \rightarrow C$ transformational sequence. Substitution by La was shown to disrupt the long range translation symmetry of the polarization in the FE_R state of this sequence, favoring the RFE and polar nanodomain state [104,105,200]. Our findings here are consistent with this perspective. The principle difference between the various orientations of epitaxial PLZT (2/95/5) thin layers is the temperature at which the slim loop RFE phase appears upon heating in the transformational sequence.

Comparisons of the bipolar and unipolar P-E loops at room temperature will reveal an important consideration for all oriented PLZT films studied. The value of P_r (after cycling through

saturation) was notably higher under bipolar drive (15-30 μC/cm^2) compared to unipolar (~5 μC/cm^2). The same value of saturation (P_s≈70 μC/cm^2) was achieved in both cases. As a consequence, the double loop characteristics were not as evident under bipolar drive as they were for the unipolar drive. We believe this discrepancy is due to the close proximity of the RFE state characterized by polar nanoregions (PNRs). In fact, in high Zr-content PLZT ceramics, PNRs have previously been found to coexist with AFE_O domain modulations whose wave vectors were nearly the same size as the PNRs [110,218]. Investigations of poled piezoelectric single crystals of PMN-PT have previously shown that rearranging PNRs within the geometrical restrictions imposed by the elastic compatibility conditions results in reduced hysteresis under unipolar drive, whereas reversing the direction of polarization under bipolar drive results in large hysteresis losses [109,219]. In this investigation, since the AFE and FE phases have the same crystal structure, the AFE modulations and PNRs could easily arrange into geometrical patterns that achieve compatibility under unipolar drive, reducing hysteretic losses compared to the bipolar case where renucleation of PNRs under reversed drive would occur.

This knowledge has important implications for explaining the differences in the ESD and ESE of the variously oriented PLZT (2/95/5) thin films under bipolar and unipolar drive. Under bipolar drive, the films feature ESD values that vary with temperature and orientation, reflecting changes not only due to phase transition, but also changes in P_r. However, under unipolar drive, the films evidence very stable values of ESD as a function of temperature between 25 and 250 °C at set field levels. Correspondingly, the ESEs were higher and more stable under unipolar drive within individual AFE, FE, and RFE phase regions.

6.5. Depth dependent ferroelectric to incommensurate/commensurate antiferroelectric phase transition

As noted in Section 6.4, the P-E curves exhibited non-negligible remanent polarization, evidencing the coexistence of AFE and FE phases in PLZT thin films. Thus, as detailed in this section, we employed TEM to observe the phase distribution through the thickness direction.

6.5.1. Overall TEM measurement and selected area electron diffraction analysis

Figures 6.15a and 6.15c provide cross-sectional TEM images for (001) and (011) PLZT films, respectively. The images indicate a columnar-like growth of the films. Figures 6.15b and 6.15d show the corresponding SAED patterns for the two films. Well-distinguished reflections for both films and substrates evidence a good epitaxy. The lattice parameters were calculated based on the distance between reflections, which enabled us to achieve accuracy to the second decimal place; resulting values are consistent with those previously determined by XRD. The (001) PLZT film had a tetragonal structure with lattice parameters of c_t = 4.14(3) Å, and a_t = 4.12(6) Å. The (011) film was monoclinic with c_m = 4.15(3) Å, and a_m = 4.13(0) Å.

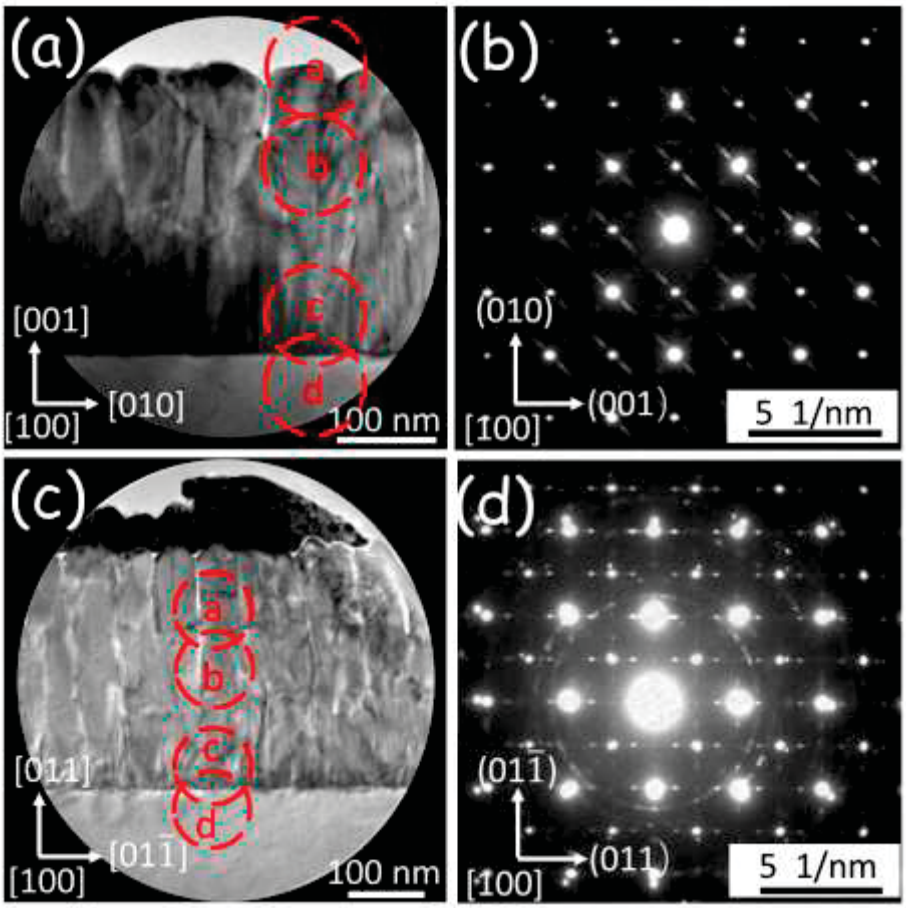

Figure 6.15: TEM cross-sectional images of (001) PLZT thin film (a), and (011) PLZT thin film (c). (b) and (d) are corresponding SAED patterns of (a) and (c), respectively. Red circles in (a) and (c) mark the areas from which SAED patterns were obtained in Figures 6.16 and 6.17, respectively.

In the SAED patterns, structural modulations were clearly evident along the <011> directions. Both $\frac{1}{2}\{011\}$ and $\frac{1}{4}\{011\}$ superlattice reflections were found for (001) and (011) films. These superlattice reflections confirmed the super-periodicity of both films, which was determined to be double or quadruple, respectively, to that of the primitive unit cell of PLZT films along the <011>. The $\frac{1}{2}(011)$ superlattice reflections can be attributed to both antiparallel (↑↓↑↓)

displacements of Pb ions along the <011> (M'_5 mode), and the cog-wheel-like oxygen octahedral rotations along the <001> (M_3 mode); whereas, the $\frac{1}{4}\{011\}$ ones are due to the arrangement of Pb ions in a pattern of two-up-two-down (↑↑↓↓↑↑↓↓) along the <011> ($\sum_3$ mode) [83,220-222]. Superlattice reflections were observed along both in-plane directions, indicative of a 90° rotation between AFE domains. The $\frac{1}{2}\{011\}$ superlattice reflections had a much lower intensity than the $\frac{1}{4}\{011\}$ ones, evidencing that the $\sum_3$ mode was dominate, as previously reported [83,110,223]. However, the dim $\frac{1}{2}\{011\}$ superlattice reflections could also be related to the weaker scattering factors from oxygen. In sum, the appearance of these superlattice reflections confirms the AFE nature of the PLZT thin films [221].

Careful inspection of the SAED patterns revealed that the $\frac{1}{4}\{011\}$ superlattice reflections in the (001) film were notably elongated along the $[01\bar{1}]$ direction, forming streaking-like reflections (marked as $\frac{1}{x}[01\bar{1}]$ reflections). The $\frac{1}{x}[01\bar{1}]$ reflections evidence that the (001) films featured an incommensurate modulation that did not have a perfectly quadruple periodicity of the primitive cell [83,110,202]. In fact, calculations indicate an incommensurate periodicity of n = 5.78 along the $[01\bar{1}]$ direction (with a corresponding modulation wavelength of 1.71 nm). In comparison, the $\frac{1}{4}[011]$ superlattice reflections had a well-defined uniform shape demonstrating a commensurate periodicity of n = 4.04 (with a corresponding modulation wave length of 1.18 nm). It has been reported that the incommensurate modulation wavelengths can vary across a 90° domain wall in AFE $PbZrO_3$-based ceramics [202]. Our observations above for the (001) films indicate that epitaxial strain may stabilize coexisting incommensurate-commensurate phases. The origin of the incommensurate structure, similar to bulk AFE orthorhombic (AFE_O) PLZT ceramics, may be a competition between FE and AFE interactions [83,110].

With regard to the (011) films, the sharp and uniform $\frac{1}{4}\{011\}$ superlattice reflections indicated a commensurate structure (n = 4.02) along two orthogonal directions. The monoclinic tilting angle in the M_A structure of the (011) films may have been able to adjust the small mismatch between frustrated dipole arrangements induced by La substitution and crystal lattice parameters.

6.5.2. Depth profile and thickness dependent phase transition

Next, a series of SAED patterns with a smaller aperture of 100 nm were obtained as a function of depth along the thickness direction from the surface to the interface with the substrate. Selected regions are marked by red circles in Figure 6.15a and 6.15c, from which patterns were measured. The appearance of the superlattice reflection (or absence thereof) was used to determine whether the AFE (or FE) phase was stable in these local regions as a function of depth into the films. As shown in Figures 6.16a and 6.17a, near the surface regions both the (001) and (011) PLZT films exhibited only fundamental reflections, indicative that the FE phase was stable.

Deeper into the layers, however, superlattice reflections became apparent (Figures 6.16b and 6.17b), becoming most obvious near the interface region with the substrate (Figures 6.16c and 6.17c). Note that (001) PLZT exhibited an AFE phase at a depth of about 100 nm from the surface; whereas for the (011) layers, the FE phase remained stable at a larger depth of about 160 nm. These results are consistent with the P-E data, where (011) PLZT layers exhibited a higher remanent polarization (33 μC/cm^2) than (001) PLZT (18 μC/cm^2), indicating that (011) PLZT contains a larger volume fraction of FE phase than the (001) sample. Nonetheless, incommensurate elongated $\frac{1}{x}[01\bar{1}]$ reflections were observed in Fig. 6.16b and 6.16c. The values of n calculated from Fig. 6.16b and 6.16c were about 5.57 and 6.41, respectively, which was slightly smaller or larger than

the apparent value calculated from Figure 6.15b. These data findings evidence that the incommensurate modulation was modified by epitaxial strain and dependent on the depth.

On moving towards the interface region, coherent selected areas fell within the substrate, the superlattice reflections disappeared (Figures 6.16d and 6.17d), suggesting a thin FE region at the interface. Thin FE regions due to film/electrode interfacial layers and strain effects have previously been reported by various groups [208-210,224].

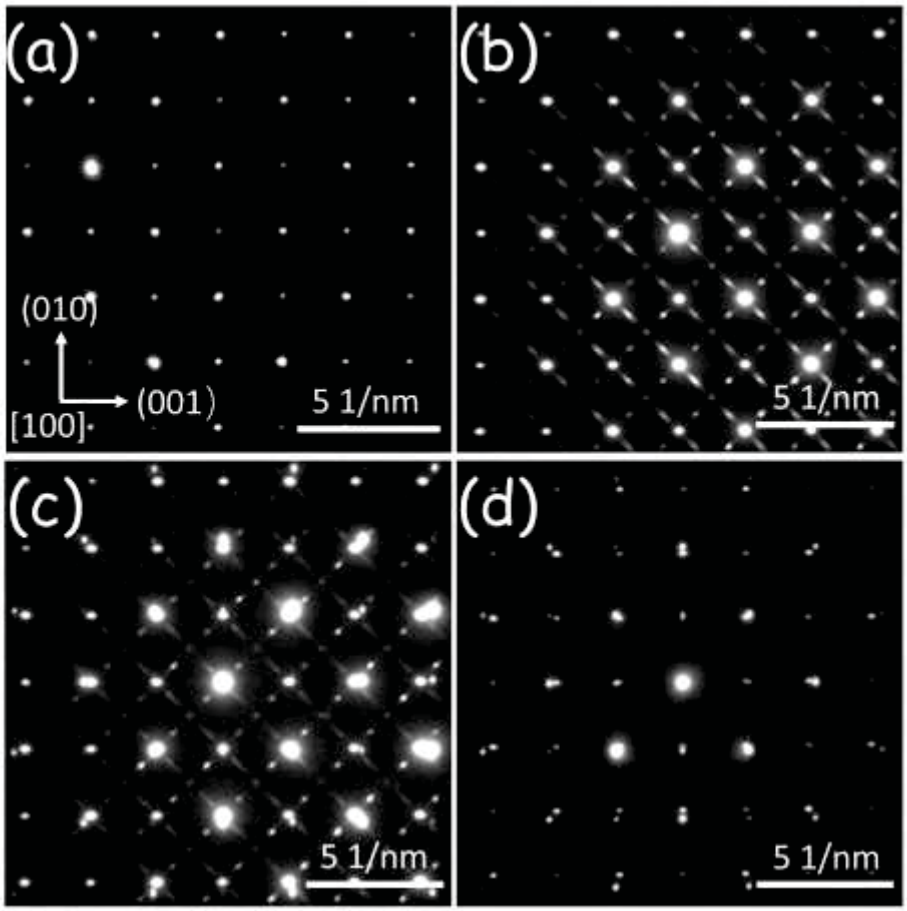

Figure 6.16: SAED patterns for a (001) PLZT thin film at various depths. The selected areas are labeled in Figure 6.15a.

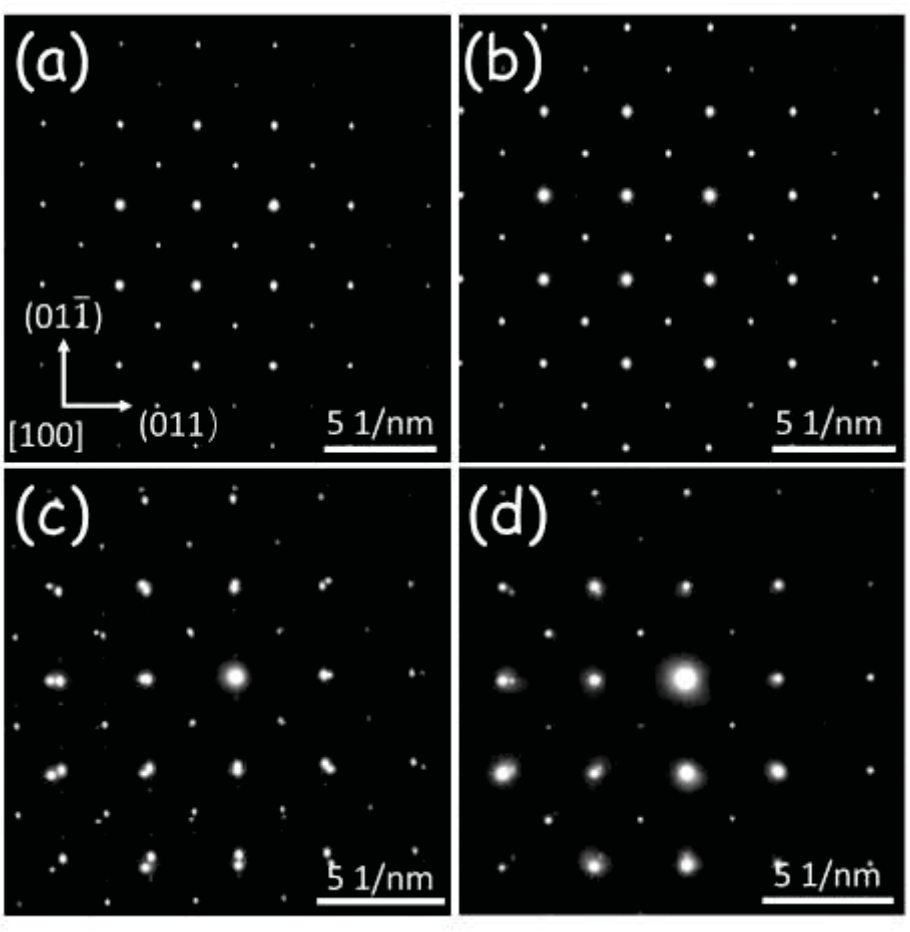

Figure 6.17: SAED patterns for a (011) PLZT thin film at various depths. The selected areas are labeled in Figure 6.15c.

To explore the origin of the FE phase in the surface region, the lattice parameters were calculated based on the reflections in Figure 6.16 and 6.17. As shown in Figures 6.18a and 6.18b, although the accuracy was not perfect, the trend of c/a ratios (tetragonality or monoclinicity) of the PLZT gradually decreased on moving from the interface to the surface. Note that the apparent c/a ratios obtained from entire films remained larger than 1. The decrease in c/a ratios approaching a value close to unity near the surface indicates a local phase transition near the surface from either tetragonal or monoclinic phase to rhombohedral (R). Consequently, the AFE_T or AFE_{MA} phase

would transform into a FE_R one. Such a phase transition would be driven by the relaxation of the epitaxial strain. The PLZT (a = b = 4.15 Å, c = 4.11 Å for bulk PLZT (0/95/5) [89]) and STO substrate (3.905 Å) have a large lattice mismatch of -6.27%, which leads to a significant large in-plane compressive strain in the films. This in-plane compressive strain induced a tetragonal phase for the (001) PLZT films (a = b = 4.12(2) Å, c = 4.15(4) Å at interface region), and a monoclinic A phase for the (011) PLZT films (a = b = 4.11(8) Å, c = 4.14(6) Å at interface region). Moving towards the surface regions, the in-plane strain gradually relaxed, reducing the c/a ratios which then approached unity. Consequently, the stable phase changed from AFE to FE. Accordingly, one would expect that if the thickness of the thin film was further increased (i.e., bulk with c/a ratio < 1), the film will again exhibit AFE characteristics, as illustrated in Figure 6.18c. This expectation is based on the simple fact that the same composition of bulk samples is AFE [83,200]. Our findings demonstrate a way to control the AFE/FE phase in epitaxial thin films by strain engineering.

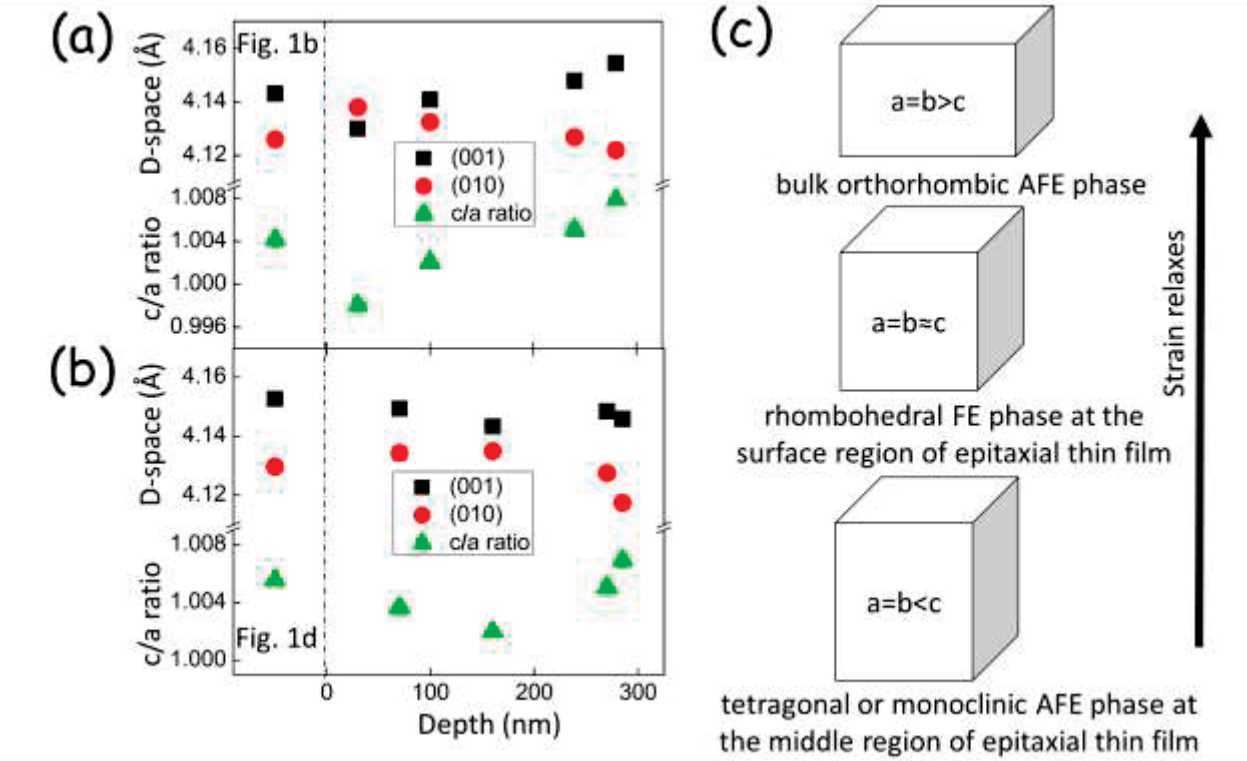

Figure 6.18: Depth resolved d-spacing values for (001) PLZT film (a), and (011) PLZT film (b). Error bars represent the standard deviation. The values on the left side of the dash lines were calculated based on Figures 6.15b and 6.15d, and those on the right side were calculated based on Figures 6.16 and 6.17, respectively. (c) Schematic illustration of the strain related evolution from highly strained AFE_T or AFE_{MA} to partially relaxed FE_R and bulk AFE_O phases.

6.6. Summary

In summary, thin films of PLZT (2/95/5) were epitaxially deposited on (100), (110), and (111) STO substrates. An orientation effect imparted to the PLZT films, via diverse values of the IP strains, resulted in either T phase stability for PLZT on (100) STO or M_A phase for PLZT on (110) and (111) STO. The interrelationship amongst crystal structure, dielectric phase transition, and energy storage performance was studied over the temperature range of 25 to 250 °C. The (001)

PLZT films exhibited an $AFE_T/FE_T \rightarrow RFE_T$ transition under E, where the bipolar drive resulted in an ESD of ≥35 J/cm^3 and an ESE of ≥70%. The (011) and (111) PLZT films exhibited an $AFE_{MA}/FE_{MA} \rightarrow FE_{MA} \rightarrow RFE_{MA}$ transition, but their ESD (ESE) values only reached ≤18 J/cm^3 (50%) and ≤40 J/cm^3 (55%), respectively. Investigations under the unipolar drive were also performed, revealing notably higher ESE values due to low energy losses.

Depth resolved SAED was used to study the crystal structure and phase stability of epitaxial (001) and (011) PLZT films on STO. With an increase in depth from the surface to the interface region, the (001) PLZT thin films underwent a phase sequence of $FE_R \rightarrow$ incommensurate $AFE_T \rightarrow FE_T$; whereas, the (011) films exhibited a phase sequence of $FE_R \rightarrow$ commensurate $AFE_{MA} \rightarrow FE_{MA}$. Our results demonstrate that the phase stability of high Zr-content PZT can be controlled by thickness related strain effects, providing a new approach for manipulating the relative AFE/FE stability through strain engineering, which also facilitates enhanced control of physical properties.

Chapter 7. Conclusion

In this dissertation, different kinds of multiferroic heterostructures were fabricated, and their crystal structures, phase transitions, and physical properties were analyzed using multiple methods, including AFM, XRD, VSM, P-E, TEM, neutron diffraction, etc. Using the approach of strain engineering, I sought to determine the relationship among epitaxial strain, phase transitions, and ferroic properties, with the goal of achieving the strain-mediated E manipulation of magnetization in heterostructures.

First, epitaxial BFO thin films were deposited on top of (001)-oriented PMN-30PT single crystal substrates. The strain states of BFO and crystal structural phases were tunable by E applied on the PMN-30PT via both the IP and OP modes. The strain-mediated antiferromagnetic state changes of BFO were studied using neutron diffraction spectroscopy, which unveiled a series of identifiable antiferromagnetic states due to strain changes induced by E.

Second, to enhance the performance of ME heterostructures with PMN-PT substrates, PMN-PT single crystals with nanograted electrodes were studied, which evidenced an enhancement in piezoelectric properties and dielectric constant by 36.7% and 38.3%, respectively. The XRD-RSM technique was used to monitor E-induced changes in the apparent symmetry and domain distribution of near-surface regions for nanograted PMN-30PT crystals.

Third, CFO/T-BFO nanocomposites were successfully fabricated on top of (001)-oriented LAO single crystal substrates. The surface morphology, crystal structure, magnetic properties, and ME effects were discussed and compared with the CFO/R-BFO nanocomposites.

Finally, epitaxial antiferroelectric PLZT thin films were deposited on differently oriented STO substrates. A thickness dependent incommensurate/commensurate antiferroelectric-to-ferroelectric phase transition was identified. The temperature dependent crystal structure, phase

transition characteristics and pathways, and energy storage behaviors were studied; resulting data facilitated a more systematic understanding of PLZT-based AFE epitaxial thin films.

Chapter 8. Future work

First, neutron diffraction has demonstrated the existence of multiple antiferromagnetic states in BFO under various E. However, it is important to clarify how these different states transit from one to another under E. Accordingly, neutron diffraction with a smaller step size of applied E would be helpful. Additionally, since there is a strain gradient within BFO thin films, it would be interesting to study how different antiferromagnetic states actually distribute through the thickness direction. Utilizing atomic-resolution TEM in a future effort would be helpful in determining this.

Second, a future investigation could be directed at using PMN-PT with nanograted electrodes as a substrate for growing epitaxial thin films like BFO. The enhanced piezoelectric properties in this case could favor the improvement of the strain-mediated ME effect.

Third, T-BFO has been proven to work as a template for inducing a T-phase-like CFO, and the CFO/T-BFO nanocomposites exhibit dramatic differences in comparison to CFO/R-BFO ones. Accordingly, additional research should be directed at using T-BFO to induce a T-phase structure of other ferromagnetic materials. Consequently, new physical phenomena would be expected due to the large c/a ratio of the T-phase structure. For instance, $La_{0.67}Sr_{0.33}MnO_3$ (LSMO) represents an excellent oxide conductive candidate in the spintronic region [56,199,225]. Since prior studies have indicated exchange coupling of LSMO with R-BFO thin films [56,199], it would be purposeful to investigate the coupling between LSMO with T-BFO, and determine if T-BFO could lead to a T-phase LSMO as well.

Fourth, since we have already evidenced that the antiferroelectricity of PLZT thin films can be tuned by epitaxial strain, it would be reasonable to combine PLZT with magnetostrictive

materials like CFO to obtain new multiferroic nanocomposites. Magnetic field induced antiferroelectric property changes could be expected.

Fifth, flexible thin films are gaining importance for use in wearable electronic devices and also in foldable cellphones [226,227]. An easy method for fabricating flexible thin films was proposed by Shen et al., whereby LSMO plays a role as a sacrifice layer that can be wet etched using a specific solution, setting free the thin films on the top [228]. This method could be adopted for fabricating flexible thin films. While the flexible thin film is able to bend, tremendous strains could be introduced that might impact the multiferroic properties.

References

1 Heron, J. T., Schlom, D. G. & Ramesh, R. Electric field control of magnetism using $BiFeO_3$-based heterostructures. *Applied Physics Reviews* **1**, 021303 (2014).

2 Spaldin, N. A. & Ramesh, R. Advances in magnetoelectric multiferroics. *Nature Materials* **18**, 203-212 (2019).

3 Schmid, H. Multi-ferroic magnetoelectrics. *Ferroelectrics* **162**, 317-338 (1994).

4 Eerenstein, W., Mathur, N. D. & Scott, J. F. Multiferroic and magnetoelectric materials. *Nature* **442**, 759 (2006).

5 Kimura, T. *et al.* Magnetic control of ferroelectric polarization. *Nature* **426**, 55 (2003).

6 Spaldin, N. A. & Fiebig, M. The Renaissance of Magnetoelectric Multiferroics. *Science* **309**, 391-392 (2005).

7 Zhang, Y. *Magnetoelectric Thin Film Heterostructures and Electric Field Manipulation of Magnetization*, Virginia Tech, (2015).

8 Wang, Z. *Magnetoelectric Effect in Ferroelectric-Ferromagnetic Heterostructures*, Virginia Tech, (2014).

9 Van Aken, B. B., Rivera, J.-P., Schmid, H. & Fiebig, M. Observation of ferrotoroidic domains. *Nature* **449**, 702 (2007).

10 Hur, N. *et al.* Electric polarization reversal and memory in a multiferroic material induced by magnetic fields. *Nature* **429**, 392 (2004).

11 Cheong, S.-W. & Mostovoy, M. Multiferroics: a magnetic twist for ferroelectricity. *Nature Materials* **6**, 13 (2007).

12 Bichurin, M. I., Petrov, V. M., Kiliba, Y. V. & Srinivasan, G. Magnetic and magnetoelectric susceptibilities of a ferroelectric/ferromagnetic composite at microwave frequencies. *Physical Review B* **66**, 134404 (2002).

13 Zhou, Z. *et al.* Antiferroelectric Materials, Applications and Recent Progress on Multiferroic Heterostructures. *SPIN* **05**, 1530001 (2015).

14 Kim, D. H., Lee, H. N., Varela, M. & Christen, H. M. Antiferroelectricity in multiferroic $BiCrO_3$ epitaxial films. *Applied Physics Letters* **89**, 162904 (2006).

15 Wang, J. *Deposition and characterization of multiferroic $BiFeO_3$ thin films*, (2005).

16 Maat, S., Thiele, J. U. & Fullerton, E. E. Temperature and field hysteresis of the antiferromagnetic-to-ferromagnetic phase transition in epitaxial FeRh films. *Physical Review B* **72**, 214432 (2005).

17 Hao, X., Zhai, J. & Yao, X. Improved energy storage performance and fatigue endurance of Sr‐doped $PbZrO_3$ antiferroelectric thin films. *Journal of the American Ceramic Society* **92**, 1133-1135 (2009).

18 Schmid, H. Introduction to the proceedings of the 2nd international conference on magnetoelectric interaction phenomena in crystals, MEIPIC-2. *Ferroelectrics* **161**, 1-28 (1994).

19 Rivera, J. P. On definitions, units, measurements, tensor forms of the linear magnetoelectric effect and on a new dynamic method applied to Cr-Cl boracite. *Ferroelectrics* **161**, 165-180 (1994).

20 Landau, L. & Lifshitz, E. Electrodynamics of Continuous Media, Eddison-Wesley. *Reading, MA* (1960).

21 Astrov, D. N. The magnetoelectric effect in antiferromagnetics. *Sov. Phys. JETP* **11**, 708-709 (1960).

22 Folen, V. J., Rado, G. T. & Stalder, E. W. Anisotropy of the Magnetoelectric Effect in Cr_2O_3. *Physical Review Letters* **6**, 607-608 (1961).
23 Smolensky, G., Isupov, V. & Krainik, N. Agranovskaya, AI IsVest. *Akad. Nauk SSSR, Ser. Fiz* **25**, 1333 (1961).
24 Ascher, E., Rieder, H., Schmid, H. & Stössel, H. Some Properties of Ferromagnetoelectric Nickel‐Iodine Boracite, $Ni_3B_7O_{13}I$. *Journal of Applied Physics* **37**, 1404-1405 (1966).
25 Al'Shin, B., Astrov, D., Tishchenko, A. & Petrov, S. Magnetoelectric effect in $BaCoF_4$. *ZhETF Pisma Redaktsiiu* **12**, 206 (1970).
26 Rivera, J. P. & Schmid, H. Linear and quadratic magnetoelectric (ME) effect in Ni‐Cl boracite. *Journal of Applied Physics* **70**, 6410-6412 (1991).
27 Hill, N. A. Why Are There so Few Magnetic Ferroelectrics? *The Journal of Physical Chemistry B* **104**, 6694-6709 (2000).
28 Van Aken, B. B., Palstra, T. T. M., Filippetti, A. & Spaldin, N. A. The origin of ferroelectricity in magnetoelectric $YMnO_3$. *Nature Materials* **3**, 164 (2004).
29 Wang, Y. *et al.* An Extremely Low Equivalent Magnetic Noise Magnetoelectric Sensor. *Advanced Materials* **23**, 4111-4114 (2011).
30 Leung, C. M., Li, J., Viehland, D. & Zhuang, X. A review on applications of magnetoelectric composites: from heterostructural uncooled magnetic sensors, energy harvesters to highly efficient power converters. *Journal of Physics D: Applied Physics* **51**, 263002 (2018).
31 Kleemann, W. Multiferroic and magnetoelectric nanocomposites for data processing. *Journal of Physics D: Applied Physics* **50**, 223001 (2017).
32 Xu, Z. *et al.* Co Nanoparticles Induced Resistive Switching and Magnetism for the Electrochemically Deposited Polypyrrole Composite Films. *ACS Applied Materials & Interfaces* **6**, 17823-17830 (2014).
33 Zhong, X. L. *et al.* Multiferroic nanoparticulate $Bi_{3.15}Nd_{0.85}Ti_3O_{12}$–$CoFe_2O_4$ composite thin films prepared by a chemical solution deposition technique. *Applied Physics Letters* **90**, 152903 (2007).
34 Deng, Y. *et al.* Three-dimensional phases-connectivity and strong magnetoelectric response of self-assembled feather-like $CoFe_2O_4$–$BaTiO_3$ nanostructures. *Chemical Physics Letters* **496**, 301-305 (2010).
35 Yan, L. *et al.* Review of magnetoelectric perovskite–spinel self-assembled nano-composite thin films. *Journal of Materials Science* **44**, 5080-5094 (2009).
36 Zheng, H. *et al.* Controlling Self-Assembled Perovskite−Spinel Nanostructures. *Nano Letters* **6**, 1401-1407 (2006).
37 Moreau, J. M., Michel, C., Gerson, R. & James, W. J. Ferroelectric $BiFeO_3$ X-ray and neutron diffraction study. *Journal of Physics and Chemistry of Solids* **32**, 1315-1320 (1971).
38 Kubel, F. & Schmid, H. Structure of a ferroelectric and ferroelastic monodomain crystal of the perovskite $BiFeO_3$. *Acta Crystallographica Section B: Structural Science* **46**, 698-702 (1990).
39 Catalan, G. & Scott, J. F. Physics and Applications of Bismuth Ferrite. *Advanced Materials* **21**, 2463-2485 (2009).
40 Kuo, C. Y. *et al.* Single-domain multiferroic $BiFeO_3$ films. *Nature Communications* **7**, 12712 (2016).

41 Ederer, C. & Fennie, C. J. Electric-field switchable magnetization via the Dzyaloshinskii–Moriya interaction: $FeTiO_3$versus $BiFeO_3$. *Journal of Physics: Condensed Matter* **20**, 434219 (2008).
42 Fiebig, M. Revival of the magnetoelectric effect. *Journal of Physics D: Applied Physics* **38**, R123-R152 (2005).
43 Teague, J. R., Gerson, R. & James, W. J. Dielectric hysteresis in single crystal $BiFeO_3$. *Solid State Communications* **8**, 1073-1074 (1970).
44 Michel, C., Moreau, J.-M., Achenbach, G. D., Gerson, R. & James, W. J. The atomic structure of $BiFeO_3$. *Solid State Communications* **7**, 701-704 (1969).
45 Wang, J. *et al.* Epitaxial $BiFeO_3$ Multiferroic Thin Film Heterostructures. *Science* **299**, 1719 (2003).
46 Yang, J. C. *et al.* Orthorhombic $BiFeO_3$. *Physical Review Letters* **109**, 247606 (2012).
47 Chen, L. *et al.* Electrical and mechanical switching of ferroelectric polarization in the 70 nm $BiFeO_3$ film. *Scientific Reports* **6**, 19092 (2016).
48 Yang, J.-C. *et al.* Electrically enhanced magnetization in highly strained $BiFeO_3$ films. *Npg Asia Materials* **8**, e269 (2016).
49 Chu, Y. H. *et al.* Ferroelectric size effects in multiferroic $BiFeO_3$ thin films. *Applied Physics Letters* **90**, 252906 (2007).
50 Zeches, R. J. *et al.* A Strain-Driven Morphotropic Phase Boundary in $BiFeO_3$. *Science* **326**, 977 (2009).
51 Sando, D. *et al.* Crafting the magnonic and spintronic response of $BiFeO_3$ films by epitaxial strain. *Nature Materials* **12**, 641 (2013).
52 Kiselev, S. V. Detection of magnetic order in ferroelectric $BiFeO_3$ by neutron diffraction. *Sov. Phys.* **7**, 742 (1963).
53 Sosnowska, I., Neumaier, T. P. & Steichele, E. Spiral magnetic ordering in bismuth ferrite. *Journal of Physics C: Solid State Physics* **15**, 4835-4846 (1982).
54 Lebeugle, D. *et al.* Electric-Field-Induced Spin Flop in BFO_3 Single Crystals at Room Temperature. *Physical Review Letters* **100**, 227602 (2008).
55 Bai, F. *et al.* Destruction of spin cycloid in $(111)_c$-oriented $BiFeO_3$ thin films by epitiaxial constraint: Enhanced polarization and release of latent magnetization. *Applied Physics Letters* **86**, 032511 (2005).
56 Zhang, W. *et al.* Piezostrain-enhanced photovoltaic effects in $BiFeO_3/La_{0.7}Sr_{0.3}MnO_3$/PMN–PT heterostructures. *Nano Energy* **18**, 315-324 (2015).
57 Wu, S. Z. *et al.* Strain-mediated electric-field control of exchange bias in a $Co_{90}Fe_{10}/BiFeO_3/SrRuO_3$/PMN-PT heterostructure. *Scientific Reports* **5**, 8905 (2015).
58 He, Q. *et al.* Electrically controllable spontaneous magnetism in nanoscale mixed phase multiferroics. *Nature Communications* **2**, 225 (2011).
59 Zhang, J. X. *et al.* Microscopic Origin of the Giant Ferroelectric Polarization in Tetragonal-like $BiFeO_3$. *Physical Review Letters* **107**, 147602 (2011).
60 Tong, W.-Y., Ding, H.-C., Gong, S. J., Wan, X. & Duan, C.-G. Magnetic ordering induced giant optical property change in tetragonal $BiFeO_3$. *Scientific Reports* **5**, 17993 (2015).
61 Park, S.-E. & Shrout, T. R. Ultrahigh strain and piezoelectric behavior in relaxor based ferroelectric single crystals. *Journal of Applied Physics* **82**, 1804-1811 (1997).
62 Guo, Y. *et al.* The phase transition sequence and the location of the morphotropic phase boundary region in (1-x)[Pb $(Mg_{1/3}Nb_{2/3})O_3$]-x$PbTiO_3$single crystal. *Journal of Physics: Condensed Matter* **15**, L77-L82 (2003).

63 Rajan, K. K., Shanthi, M., Chang, W. S., Jin, J. & Lim, L. C. Dielectric and piezoelectric properties of [001] and [011]-poled relaxor ferroelectric PZN–PT and PMN–PT single crystals. *Sensors and Actuators A: Physical* **133**, 110-116 (2007).
64 Park, S.-E. & Shrout, T. R. Relaxor based ferroelectric single crystals for electro-mechanical actuators. *Materials Research Innovations* **1**, 20-25 (1997).
65 Han, P., Yan, W., Tian, J., Huang, X. & Pan, H. Cut directions for the optimization of piezoelectric coefficients of lead magnesium niobate–lead titanate ferroelectric crystals. *Applied Physics Letters* **86**, 052902 (2005).
66 Bellaiche, L. & Vanderbilt, D. Intrinsic Piezoelectric Response in Perovskite Alloys: PMN-PT versus PZT. *Physical Review Letters* **83**, 1347-1350, doi:10.1103/PhysRevLett.83.1347 (1999).
67 Bai, F. *et al.* X-ray and neutron diffraction investigations of the structural phase transformation sequence under electric field in $0.7Pb(Mg_{1/3}Nb_{2/3})$-$0.3PbTiO_3$ crystal. *Journal of Applied Physics* **96**, 1620-1627 (2004).
68 Wang, Y. *et al.* Temperature-induced and electric-field-induced phase transitions in rhombohedral $Pb(In_{1/2}Nb_{1/2})O_3$−$Pb(Mg_{1/3}Nb_{2/3})O_3$−$PbTiO_3$ ternary single crystals. *Physical Review B* **90**, 134107 (2014).
69 Fu, H. & Cohen, R. E. Polarization rotation mechanism for ultrahigh electromechanical response in single-crystal piezoelectrics. *Nature* **403**, 281 (2000).
70 Cao, H., Li, J., Viehland, D. & Xu, G. Fragile phase stability in $(1-x)Pb(Mg_{1/3}Nb_{2/3}O_3)-xPbTiO_3$ crystals: A comparison of [001] and [110] field-cooled phase diagrams. *Physical Review B* **73**, 184110 (2006).
71 Zhang, S. *et al.* Advantages and challenges of relaxor-$PbTiO_3$ ferroelectric crystals for electroacoustic transducers – A review. *Progress in Materials Science* **68**, 1-66 (2015).
72 Viehland, D. D. & Salje, E. K. H. Domain boundary-dominated systems: adaptive structures and functional twin boundaries. *Advances in Physics* **63**, 267-326 (2014).
73 Shuvalov, L. A. *Modern crystallography IV: physical properties of crystals*. Vol. 4 (Springer, 1988).
74 Viehland, D. Symmetry-adaptive ferroelectric mesostates in oriented $Pb(BI_{1/3}BII_{2/3})O_3$–$PbTiO_3$ crystals. *Journal of Applied Physics* **88**, 4794-4806 (2000).
75 Wechsler, M. S., Lieberman, D. S. & Read, T. A. On the Theory of the Formation of Martensite. *Transactions of the American Institute of Mining and Metallurgical Engineers* **197(11)**, p. 1503-1515 (1953).
76 Burns, G. & Dacol, F. H. Glassy polarization behavior in ferroelectric compounds $Pb(Mg_{1/3}Nb_{2/3})O_3$ and $Pb(Zn_{1/3}Nb_{2/3})O_3$. *Solid State Communications* **48**, 853-856 (1983).
77 Chang, W.-Y. *et al.* Patterned nano-domains in PMN-PT single crystals. *Acta Materialia* **143**, 166-173 (2018).
78 Wada, S. *et al.* Enhanced Piezoelectric Property of Barium Titanate Single Crystals with Engineered Domain Configurations. *Japanese Journal of Applied Physics* **38**, 5505-5511 (1999).
79 Yamashita, Y., Yamamoto, N., Itsumi, K. & Hosono, Y. Effects of Manganese Oxides/Gold Composite Electrode on Piezoelectric Properties of Lead Magnesium Niobate Titanate Single Crystal. *Japanese Journal of Applied Physics* **50**, 09NC05 (2011).
80 Zhang, S. & Shrout, T. R. Relaxor-PT single crystals: observations and developments. *IEEE Transactions on Ultrasonics, Ferroelectrics, and Frequency Control* **57**, 2138-2146 (2010).

81 Gao, P. *et al.* Revealing the role of defects in ferroelectric switching with atomic resolution. *Nature Communications* **2**, 591 (2011).
82 Liu, Z. *et al.* Antiferroelectrics for Energy Storage Applications: a Review. *Advanced Materials Technologies* **3**, 1800111 (2018).
83 Dai, X. *New perspectives of pure and lanthanum modified lead zirconate titanate crystalline solutions*, University of Illinois at Urbana-Champaign, (1995).
84 Fesenko, O. E., Kolesova, R. V. & Sindeyev, Y. G. The structural phase transitions in lead zirconate in super-high electric fields. *Ferroelectrics* **20**, 177-178 (1978).
85 Ge, J. *et al.* Enhancement of energy storage in epitaxial $PbZrO_3$ antiferroelectric films using strain engineering. *Applied Physics Letters* **105**, 112908 (2014).
86 Zuo, Z.-H. *et al.* Enhanced energy storage behaviors in free-standing antiferroelectric Pb $(Zr_{0.95}Ti_{0.05})O_3$ thin membranes. *Chinese Physics B* **25**, 087702 (2016).
87 Uchino, K. & Nomura, S. Electrostriction in PZT-family antiferroelectrics. *Ferroelectrics* **50**, 191-196 (1983).
88 Noheda, B. *et al.* A monoclinic ferroelectric phase in the $Pb(Zr_{1-x}Ti_x)O_3$ solid solution. *Applied physics letters* **74**, 2059-2061 (1999).
89 Lu, C., Shen, H. & Wang, Y. The growth and phase transitions of epitaxial $Pb(Zr_{0.95}Ti_{0.05})O_3$ thin films prepared by sputter deposition combined with post-annealing on $SrTiO_3$ (100). *Journal of crystal growth* **191**, 113-118 (1998).
90 Gupta, S. M., Li, J. F. & Viehland, D. Coexistence of Relaxor and Normal Ferroelectric Phases in Morphotropic Phase Boundary Compositions of Lanthanum - Modified Lead Zirconate Titanate. *Journal of the American Ceramic Society* **81**, 557-564 (1998).
91 Ma, C., Ma, B., Mi, S.-B., Liu, M. & Wu, J. Enhanced dielectric nonlinearity in epitaxial $Pb_{0.92}La_{0.08}Zr_{0.52}Ti_{0.48}O_3$ thin films. *Applied Physics Letters* **104**, 162902 (2014).
92 Vu, H. T. *et al.* Ferroelectric and piezoelectric responses of (110) and (001)-oriented epitaxial $Pb(Zr_{0.52}Ti_{0.48})O_3$ thin films on all-oxide layers buffered silicon. *Materials research bulletin* **72**, 160-167 (2015).
93 Hu, G. *et al.* Enhanced energy density with a wide thermal stability in epitaxial $Pb_{0.92}La_{0.08}Zr_{0.52}Ti_{0.48}O_3$ thin films. *Applied Physics Letters* **109**, 193904 (2016).
94 Saito, K., Kurosawa, T., Akai, T., Oikawa, T. & Funakubo, H. Structural characterization and 90° domain contribution to ferroelectricity of epitaxial $Pb(Zr_{0.35},Ti_{0.65})O_3$ thin films. *Journal of Applied Physics* **93**, 545-550 (2002).
95 Lee, H. N. *et al.* Suppressed dependence of polarization on epitaxial strain in highly polar ferroelectrics. *Phys Rev Lett* **98**, 217602 (2007).
96 Chisholm, M. F., Luo, W., Oxley, M. P., Pantelides, S. T. & Lee, H. N. Atomic-scale compensation phenomena at polar interfaces. *Physical Review Letters* **105**, 197602 (2010).
97 Liu, Z. *et al.* Temperature-dependent stability of energy storage properties of $Pb_{0.97}La_{0.02}(Zr_{0.58}Sn_{0.335}Ti_{0.085})O_3$ antiferroelectric ceramics for pulse power capacitors. *Applied Physics Letters* **106**, 262901 (2015).
98 Burn, I. & Smyth, D. Energy storage in ceramic dielectrics. *Journal of Materials Science* **7**, 339-343 (1972).
99 Hu, Z., Ma, B., Koritala, R. & Balachandran, U. Temperature-dependent energy storage properties of antiferroelectric $Pb_{0.96}La_{0.04}Zr_{0.98}Ti_{0.02}O_3$ thin films. *Applied Physics Letters* **104**, 263902 (2014).
100 Jo, H. R. & Lynch, C. S. A high energy density relaxor antiferroelectric pulsed capacitor dielectric. *Journal of Applied Physics* **119**, 024104 (2016).

101 Love, G. R. Energy Storage in Ceramic Dielectrics. *Journal of the American Ceramic Society* **73**, 323-328 (1990).
102 Pan, H., Zeng, Y., Shen, Y., Lin, Y.-H. & Nan, C.-W. Thickness-dependent dielectric and energy storage properties of $(Pb_{0.96}La_{0.04})(Zr_{0.98}Ti_{0.02})O_3$ antiferroelectric thin films. *Journal of Applied Physics* **119**, 124106 (2016).
103 Ma, B., Kwon, D.-K., Narayanan, M. & Balachandran, U. B. Dielectric properties and energy storage capability of antiferroelectric $Pb_{0.92}La_{0.08}Zr_{0.95}Ti_{0.05}O_3$ film-on-foil capacitors. *Journal of Materials Research* **24**, 2993-2996 (2009).
104 Thomas, N. W. A new framework for understanding relaxor ferroelectrics. *Journal of Physics and Chemistry of Solids* **51**, 1419-1431 (1990).
105 Li, J.-F., Dai, X., Chow, A. & Viehland, D. Polarization switching mechanisms and electromechanical properties of La-modified lead zirconate titanate ceramics. *Journal of Materials Research* **10**, 926-938 (1995).
106 Luo, C. *Structural Study of Heterogeneous States in Lead-free NBT-based Single Crystals*, Virginia Tech, (2016).
107 Li, B. *et al.* Antiferroelectric to relaxor ferroelectric phase transition in PbO modified $(Pb_{0.97}La_{0.02})(Zr_{0.95}Ti_{0.05})O_3$ ceramics with a large energy-density for dielectric energy storage. *RSC Advances* **7**, 43327-43333 (2017).
108 Viehland, D. & Powers, J. Effect of uniaxial stress on the electromechanical properties of $0.7Pb(Mg_{1/3}Nb_{2/3})O_3–0.3PbTiO_3$ crystals and ceramics. *Journal of Applied Physics* **89**, 1820-1825 (2001).
109 Viehland, D. Effect of uniaxial stress upon the electromechanical properties of various piezoelectric ceramics and single crystals. *Journal of the American Ceramic Society* **89**, 775-785 (2006).
110 Viehland, D., Dai, X. H., Li, J. F. & Xu, Z. Effects of quenched disorder on La-modified lead zirconate titanate: Long- and short-range ordered structurally incommensurate phases, and glassy polar clusters. *Journal of Applied Physics* **84**, 458-471, doi:10.1063/1.368049 (1998).
111 Xu, Z., Viehland, D. & Payne, D. A. in *Proceedings of 1994 IEEE International Symposium on Applications of Ferroelectrics.* 589-590.
112 Dai, X., Xu, Z. & Viehland, D. Phase stability and transformations in pure and lanthanum modified lead zirconate ceramics. *Journal of Applied Physics* **77**, 5086-5094, doi:10.1063/1.359317 (1995).
113 Xu, Z., Dai, X. & Viehland, D. Impurity-induced incommensuration in antiferroelectric La-modified lead zirconate titanate. *Physical Review B* **51**, 6261-6271, doi:10.1103/PhysRevB.51.6261 (1995).
114 Blinc, R. The soft mode concept and the history of ferroelectricity. *Ferroelectrics* **74**, 301-303, doi:10.1080/00150198708201310 (1987).
115 Hewat, A. W. Soft modes and the structure, spontaneous polarization and Curie constants of perovskite ferroelectrics: tetragonal potassium niobate. *Journal of Physics C: Solid State Physics* **6**, 1074-1084 (1973).
116 Gao, M. *et al.* E-field controlled phase transformation in bismuth ferrite thin films, and effect of laser energy density. *Applied Physics Letters* **111**, 152905 (2017).
117 Gao, M. *et al.* Apparent phase stability and domain distribution of PMN-30PT single crystals with nanograted Au/MnOx electrodes. *Acta Materialia* **169**, 28-35 (2019).

118 Gao, M. *et al.* Magnetoelectricity of $CoFe_2O_4$ and tetragonal phase $BiFeO_3$ nanocomposites prepared by pulsed laser deposition. *Scientific Reports* **8**, 323 (2018).
119 Gao, M. *et al.* Phase transition and energy storage behavior of antiferroelectric PLZT thin films epitaxially deposited on SRO buffered STO single crystal substrates. *Journal of the American Ceramic Society* **102**, 5180-5191 (2019).
120 Gao, M., Tang, X., Dai, S., Li, J. & Viehland, D. Depth dependent ferroelectric to incommensurate/commensurate antiferroelectric phase transition in epitaxial lanthanum modified lead zirconate titanate thin films. *Applied Physics Letters* **115**, 072901 (2019).
121 Zhao, X., Fang, B., Cao, H., Guo, Y. & Luo, H. Dielectric and piezoelectric performance of PMN–PT single crystals with compositions around the MPB: influence of composition, poling field and crystal orientation. *Materials Science and Engineering: B* **96**, 254-262 (2002).
122 Yin, Z.-W., Luo, H.-S., Wang, P.-C. & Xu, G.-S. Growth, characterization and properties of relaxor ferroelectric PMN-PT single crystals. *Ferroelectrics* **229**, 207-216 (1999).
123 Luo, H., Xu, G., Xu, H., Wang, P. & Yin, Z. Compositional Homogeneity and Electrical Properties of Lead Magnesium Niobate Titanate Single Crystals Grown by a Modified Bridgman Technique. *Japanese Journal of Applied Physics* **39**, 5581-5585 (2000).
124 Nan, T., Liu, M., Ren, W., Ye, Z.-G. & Sun, N. X. Voltage Control of Metal-insulator Transition and Non-volatile Ferroelastic Switching of Resistance in VO_x/PMN-PT Heterostructures. *Scientific Reports* **4**, 5931 (2014).
125 Smith, H. M. & Turner, A. Vacuum deposited thin films using a ruby laser. *Applied Optics* **4**, 147-148 (1965).
126 Krebs, H.-U. *et al.* in *Advances in Solid State Physics* (ed Bernhard Kramer) 505-518 (Springer Berlin Heidelberg, 2003).
127 Fähler, S., Störmer, M. & Krebs, H. U. Origin and avoidance of droplets during laser ablation of metals. *Applied Surface Science* **109-110**, 433-436 (1997).
128 Singh, R. K. & Narayan, J. Pulsed-laser evaporation technique for deposition of thin films: Physics and theoretical model. *Physical Review B* **41**, 8843-8859 (1990).
129 Phipps, C. R. *et al.* Impulse coupling to targets in vacuum by KrF, HF, and CO_2 single‐pulse lasers. *Journal of Applied Physics* **64**, 1083-1096 (1988).
130 Cai, R. *et al.* Origin of Different Growth Modes for Epitaxial Manganite Films. *Journal of the American Ceramic Society* **96**, 1660-1665 (2013).
131 Chu, Y. H. *et al.* Nanoscale Domain Control in Multiferroic $BiFeO_3$ Thin Films. *Advanced Materials* **18**, 2307-2311 (2006).
132 Tang, X. *et al.* Nanopillars with E-field accessible multi-state ($N \geqslant 4$) magnetization having giant magnetization changes in self-assembled BiFeO3-CoFe2O4/Pb(Mg1/3Nb2/3)-38at%PbTiO3 heterostructures. *Scientific Reports* **8**, 1628, doi:10.1038/s41598-018-19673-8 (2018).
133 Binnig, G., Quate, C. F. & Gerber, C. Atomic Force Microscope. *Physical Review Letters* **56**, 930-933 (1986).
134 Albrecht, T. R., Grütter, P., Horne, D. & Rugar, D. Frequency modulation detection using high‐Q cantilevers for enhanced force microscope sensitivity. *Journal of Applied Physics* **69**, 668-673 (1991).
135 Bonnell, D. Scanning Probe Microscopy and Spectroscopy. *Theory, Techniques, and Applications* **289** (2000).

136 Kalinin, S. V. & Bonnell, D. A. Imaging mechanism of piezoresponse force microscopy of ferroelectric surfaces. *Physical Review B* **65**, 125408 (2002).
137 Güthner, P. & Dransfeld, K. Local poling of ferroelectric polymers by scanning force microscopy. *Applied Physics Letters* **61**, 1137-1139 (1992).
138 Kalinin, S. V. *et al.* Vector Piezoresponse Force Microscopy. *Microscopy and Microanalysis* **12**, 206-220 (2006).
139 Martin, Y. & Wickramasinghe, H. K. Magnetic imaging by ''force microscopy'' with 1000 Å resolution. *Applied Physics Letters* **50**, 1455-1457 (1987).
140 Yan, L. *Two phase magnetoelectric epitaxial composite thin films*, Virginia Tech, (2009).
141 Bragg William, H. & Bragg William, L. The reflection of X-rays by crystals. *Proceedings of the Royal Society of London. Series A, Containing Papers of a Mathematical and Physical Character* **88**, 428-438 (1913).
142 Diamant, H., Drenck, K. & Pepinsky, R. Bridge for Accurate Measurement of Ferroelectric Hysteresis. *Review of Scientific Instruments* **28**, 30-33 (1957).
143 Foner, S. Versatile and Sensitive Vibrating - Sample Magnetometer. *Review of Scientific Instruments* **30**, 548-557 (1959).
144 Yang, Y. *Barium Titanate-Based Magnetoelectric Nanocomposites*, Virginia Tech, (2011).
145 Clarke, J. a. A. B. E. (Wiley-VCH Weinheim, 2004).
146 Egerton, R. F. *Physical principles of electron microscopy*. (Springer, 2005).
147 Muller, D. Introduction to electron microscopy. *Cornell University* (2008).
148 https://neutrons.ornl.gov/fietax.
149 Ke, X. *et al.* Magnetic structure of epitaxial multiferroic $BiFeO_3$ films with engineered ferroelectric domains. *Physical Review B* **82**, 134448 (2010).
150 Ratcliff Ii, W. *et al.* Neutron Diffraction Investigations of Magnetism in $BiFeO_3$ Epitaxial Films. *Advanced Functional Materials* **21**, 1567-1574 (2011).
151 Wang, Z., Wang, Y., Luo, H., Li, J. & Viehland, D. Crafting the strain state in epitaxial thin films: A case study of ${\mathrm $CoFe_2O_4$ films on $Pb(Mg,Nb)O_3$-$PbTiO_3$. *Physical Review B* **90**, 134103 (2014).
152 Lee, G., Fuentes-Fernandez, E. M. A., Lian, G., Katiyar, R. S. & Auciello, O. Hetero-epitaxial $BiFeO_3/SrTiO_3$ nanolaminates with higher piezoresponse performance over stoichiometric $BiFeO_3$ films. *Applied Physics Letters* **106**, 022905 (2015).
153 Li, Q. *et al.* Giant elastic tunability in strained $BiFeO_3$ near an electrically induced phase transition. *Nature Communications* **6**, 8985 (2015).
154 You, T. *et al.* Engineering interface-type resistive switching in $BiFeO_3$ thin film switches by Ti implantation of bottom electrodes. *Scientific Reports* **5**, 18623 (2015).
155 Lux, R. *et al.* Pulsed-laser deposition and growth studies of $Bi_3Fe_5O_{12}$ thin films. *Journal of Applied Physics* **100**, 113511 (2006).
156 Zheng, R. K., Habermeier, H. U., Chan, H. L. W., Choy, C. L. & Luo, H. S. Effect of ferroelectric-poling-induced strain on the phase separation and magnetotransport properties of $La_{0.7}Ca_{0.15}Sr_{0.15}MnO_3$ thin films grown on ferroelectric single-crystal substrates. *Physical Review B* **80**, 104433 (2009).
157 Chen, Z. *et al.* Low-Symmetry Monoclinic Phases and Polarization Rotation Path Mediated by Epitaxial Strain in Multiferroic $BiFeO_3$ Thin Films. *Advanced Functional Materials* **21**, 133-138 (2011).
158 Noheda, B., Cox, D. E., Shirane, G., Gao, J. & Ye, Z. G. Phase diagram of the ferroelectric relaxor (1-x) $PbMg_{1/3}Nb_{2/3}O_3$-$xPbTiO_3$. *Physical Review B* **66**, 054104 (2002).

159 Schlom, D. G. *et al.* Strain Tuning of Ferroelectric Thin Films. *Annual Review of Materials Research* **37**, 589-626 (2007).
160 You, L. *et al.* Characterization and Manipulation of Mixed Phase Nanodomains in Highly Strained $BiFeO_3$ Thin Films. *ACS Nano* **6**, 5388-5394 (2012).
161 Gao, T. *et al.* Electric-Field Induced Reversible Switching of the Magnetic Easy Axis in Co/$BiFeO_3$ on $SrTiO_3$. *Nano Letters* **17**, 2825-2832 (2017).
162 Béa, H., Bibes, M., Petit, S., Kreisel, J. & Barthélémy, A. Structural distortion and magnetism of $BiFeO_3$ epitaxial thin films: A Raman spectroscopy and neutron diffraction study. *Philosophical Magazine Letters* **87**, 165-174 (2007).
163 Przenioslo, R., Regulski, M. & Sosnowska, I. Modulation in Multiferroic $BiFeO_3$: Cycloidal, Elliptical or SDW? *Journal of the Physical Society of Japan* **75**, 084718-084718 (2006).
164 Lynn, J. W., Shirane, G. & Blume, M. Covalency Effects in the Magnetic Form Factor of Ir in K_2IrCl_6. *Physical Review Letters* **37**, 154-157 (1976).
165 Zhao, T. *et al.* Electrical control of antiferromagnetic domains in multiferroic $BiFeO_3$ films at room temperature. *Nature Materials* **5**, 823-829 (2006).
166 Tang, X. *et al.* Non-volatility using materials with only volatile properties: Vertically integrated magnetoelectric heterostructures and their potential for multi-level-cell devices. *Applied Physics Letters* **114**, 242903 (2019).
167 Tang, X. *et al.* Nanostructure-enhanced magnetoelectric/magnetostrictive properties and reduced losses in self-assembled epitaxial $CuFe_2O_4$–$BiFeO_3$ layers on $Pb(Mg_{1/3}Nb_{2/3})O_3$–33at%$PbTiO_3$ crystals. *Journal of the American Ceramic Society* (2019).
168 Ye, Z. G., Noheda, B., Dong, M., Cox, D. & Shirane, G. Monoclinic phase in the relaxor-based piezoelectric/ferroelectric $Pb(Mg_{1/3}Nb_{2/3})O_3$–$PbTiO_3$ system. *Physical Review B* **64**, 184114 (2001).
169 Béa, H. *et al.* Mechanisms of Exchange Bias with Multiferroic $BiFeO_3$ Epitaxial Thin Films. *Physical Review Letters* **100**, 017204 (2008).
170 Lee, S. *et al.* Single ferroelectric and chiral magnetic domain of single-crystalline $BiFeO_3$ in an electric field. *Physical Review B* **78**, 100101 (2008).
171 Chang, W.-Y. *et al.* Study on dielectric and piezoelectric properties of $0.7Pb(Mg_{1/3}Nb_{2/3})O_3$-$0.3PbTiO_3$ single crystal with nano-patterned composite electrode. *Journal of Applied Physics* **114**, 114103 (2013).
172 Bai, F., Li, J. & Viehland, D. Domain hierarchy in annealed (001)-oriented $Pb(Mg_{1/3}Nb_{2/3})O_3$-x%$PbTiO_3$ single crystals. *Applied Physics Letters* **85**, 2313-2315 (2004).
173 Viehland, D., Kim, M. C., Xu, Z. & Li, J. F. Long‐time present tweedlike precursors and paraelectric clusters in ferroelectrics containing strong quenched randomness. *Applied Physics Letters* **67**, 2471-2473 (1995).
174 Xiang, Y., Zhang, R. & Cao, W. Optimization of piezoelectric properties for $[001]_c$ poled $0.94Pb(Zn_{1/3}Nb_{2/3})O_3$–$0.06PbTiO_3$ single crystals. *Applied Physics Letters* **96**, 092902 (2010).
175 Ohwada, K., Hirota, K., Rehrig, P. W., Fujii, Y. & Shirane, G. Neutron diffraction study of field-cooling effects on the relaxor ferroelectric $Pb[(Zn_{1/3}Nb_{2/3})_{0.92}Ti_{0.08}]O_3$. *Physical Review B* **67**, 094111 (2003).
176 Jin, Y. M., Wang, Y. U., Khachaturyan, A. G., Li, J. F. & Viehland, D. Adaptive ferroelectric states in systems with low domain wall energy: Tetragonal microdomains. *Journal of Applied Physics* **94**, 3629-3640 (2003).

177 Zhao, J., Zhang, Q. M., Kim, N. & Shrout, T. Electromechanical Properties of Relaxor Ferroelectric Lead Magnesium Niobate-Lead Titanate Ceramics. *Japanese Journal of Applied Physics* **34**, 5658-5663 (1995).
178 Yang, J. J. *et al.* Electric field manipulation of magnetization at room temperature in multiferroic $CoFe_2O_4/Pb(Mg_{1/3}Nb_{2/3})_{0.7}Ti_{0.3}O_3$ heterostructures. *Applied Physics Letters* **94**, 212504 (2009).
179 Li, J. *et al.* The role of magnetoelastic strain on orbital control and transport properties in an $LaTiO_3$–$CoFe_2O_4$ heterostructure. *Journal of Physics: Condensed Matter* **21**, 276002 (2009).
180 Zheng, H. *et al.* Multiferroic $BaTiO_3$-$CoFe_2O_4$ Nanostructures. *Science* **303**, 661 (2004).
181 Fritsch, D. & Ederer, C. First-principles calculation of magnetoelastic coefficients and magnetostriction in the spinel ferrites $CoFe_2O_4$ and $NiFe_2O_4$. *Physical Review B* **86**, 014406 (2012).
182 Nogués, J. *et al.* Exchange bias in nanostructures. *Physics Reports* **422**, 65-117 (2005).
183 Zhang, W. *et al.* Strain relaxation and enhanced perpendicular magnetic anisotropy in $BiFeO_3$:$CoFe_2O_4$ vertically aligned nanocomposite thin films. *Applied Physics Letters* **104**, 062402 (2014).
184 Choi, E.-M. *et al.* Strong room temperature exchange bias in self-assembled $BiFeO_3$–Fe_3O_4 nanocomposite heteroepitaxial films. *Applied Physics Letters* **102**, 012905 (2013).
185 Wu, S. M. *et al.* Reversible electric control of exchange bias in a multiferroic field-effect device. *Nature Materials* **9**, 756 (2010).
186 Comes, R., Khokhlov, M., Liu, H., Lu, J. & Wolf, S. A. Magnetic anisotropy in composite $CoFe_2O_4$-$BiFeO_3$ ultrathin films grown by pulsed-electron deposition. *Journal of Applied Physics* **111**, 07D914 (2012).
187 Wang, Z., Yang, Y., Viswan, R., Li, J. & Viehland, D. Giant electric field controlled magnetic anisotropy in epitaxial $BiFeO_3$-$CoFe_2O_4$ thin film heterostructures on single crystal $Pb(Mg_{1/3}Nb_{2/3})_{0.7}Ti_{0.3}O_3$ substrate. *Applied Physics Letters* **99**, 043110 (2011).
188 Dix, N. *et al.* Selectable Spontaneous Polarization Direction and Magnetic Anisotropy in $BiFeO_3$−$CoFe_2O_4$ Epitaxial Nanostructures. *ACS Nano* **4**, 4955-4961 (2010).
189 Liao, S.-C. *et al.* Misorientation Control and Functionality Design of Nanopillars in Self-Assembled Perovskite−Spinel Heteroepitaxial Nanostructures. *ACS Nano* **5**, 4118-4122 (2011).
190 Liu, Y.-T., Ku, C.-S., Chiu, S.-J., Lee, H.-Y. & Chen, S.-Y. Ultrathin Oriented $BiFeO_3$ Films from Deposition of Atomic Layers with Greatly Improved Leakage and Ferroelectric Properties. *ACS Applied Materials & Interfaces* **6**, 443-449 (2014).
191 Wang, X. W., Zhang, Y. Q., Meng, H., Wang, Z. J. & Zhang, Z. D. Perpendicular magnetic anisotropy in 70nm $CoFe_2O_4$ thin films fabricated on SiO_2/Si(100) by the sol–gel method. *Journal of Alloys and Compounds* **509**, 7803-7807 (2011).
192 Schulthess, T. C. & Butler, W. H. Consequences of Spin-Flop Coupling in Exchange Biased Films. *Physical Review Letters* **81**, 4516-4519 (1998).
193 Zheng, H., Kreisel, J., Chu, Y.-H., Ramesh, R. & Salamanca-Riba, L. Heteroepitaxially enhanced magnetic anisotropy in $BaTiO_3$–$CoFe_2O_4$ nanostructures. *Applied Physics Letters* **90**, 113113 (2007).
194 Aimon, N. M., Kim, D. H., Sun, X. & Ross, C. A. Multiferroic Behavior of Templated $BiFeO_3$–$CoFe_2O_4$ Self-Assembled Nanocomposites. *ACS Applied Materials & Interfaces* **7**, 2263-2268 (2015).

195 Aimon, N. M., Choi, H. K., Sun, X. Y., Kim, D. H. & Ross, C. A. Templated Self-Assembly of Functional Oxide Nanocomposites. *Advanced Materials* **26**, 3063-3067 (2014).
196 Rodriguez, B. J. *et al.* Spatially resolved mapping of ferroelectric switching behavior in self-assembled multiferroic nanostructures: strain, size, and interface effects. *Nanotechnology* **18**, 405701 (2007).
197 Yan, F., Chen, G., Lu, L., Finkel, P. & Spanier, J. E. Local probing of magnetoelectric coupling and magnetoelastic control of switching in $BiFeO_3$-$CoFe_2O_4$ thin-film nanocomposite. *Applied Physics Letters* **103**, 042906 (2013).
198 Pan, M., Hong, S., Guest, J. R., Liu, Y. & Petford-Long, A. Visualization of magnetic domain structure changes induced by interfacial strain in $CoFe_2O_4$/$BaTiO_3$ heterostructures. *Journal of Physics D: Applied Physics* **46**, 055001 (2013).
199 Yin, L., Zhang, Q., Li, D., Mi, W. & Wang, X. Electric Field Modulation on Special Interfacial Magnetic States in Tetragonal $La_{2/3}Sr_{1/3}MnO_3$/$BiFeO_3$ Heterostructures. *The Journal of Physical Chemistry C* **120**, 15342-15348 (2016).
200 Dai, X. & Viehland, D. Effects of lanthanum modification on the antiferroelectric - ferroelectric stability of high zirconium - content lead zirconate titanate. *Journal of applied physics* **76**, 3701-3709 (1994).
201 Xu, Z., Dai, X., Li, J. F. & Viehland, D. Coexistence of incommensurate antiferroelectric and relaxorlike ferroelectric orderings in high Zr - content La - modified lead zirconate titanate ceramics. *Applied Physics Letters* **68**, 1628-1630 (1996).
202 He, H. & Tan, X. Electric-field-induced transformation of incommensurate modulations in antiferroelectric $Pb_{0.99}Nb_{0.02}[(Zr_{1-x}Snx)_{1-y}Ti_y]_{0.98}O_3$. *Physical Review B* **72**, 024102, doi:10.1103/PhysRevB.72.024102 (2005).
203 Kim, Y. K., Morioka, H. & Funakubo, H. Domain structures in highly (100)-oriented epitaxial $Pb(Zr_{0.35},Ti_{0.65})O_3$ thin films. *Journal of Applied Physics* **101**, 064112 (2007).
204 Baek, S. *et al.* Giant piezoelectricity on Si for hyperactive MEMS. *Science* **334**, 958-961 (2011).
205 Warusawithana, M. P. *et al.* A ferroelectric oxide made directly on silicon. *Science* **324**, 367-370 (2009).
206 Sharifzadeh Mirshekarloo, M., Yao, K. & Sritharan, T. Large strain and high energy storage density in orthorhombic perovskite $(Pb_{0.97}La_{0.02})(Zr_{1-x-y}Sn_xTi_y)O_3$ antiferroelectric thin films. *Applied Physics Letters* **97**, 142902 (2010).
207 Kong, L. & Ma, J. Preparation and characterization of antiferroelectric PLZT2/95/5 thin films via a sol–gel process. *Materials Letters* **56**, 30-37 (2002).
208 Xu, B., Ye, Y., Wang, Q.-M. & Cross, L. E. Dependence of electrical properties on film thickness in lanthanum-doped lead zirconate titanate stannate antiferroelectric thin films. *Journal of Applied Physics* **85**, 3753-3758 (1999).
209 Chen, H., Li, K., Gaskey, C. & Cross, L. Thickness-dependent electrical properties in lanthanum-doped PZT thick films. *Ferroelectric Thin Films V* **433**, 325-332 (1996).
210 Larsen, P., Dormans, G., Taylor, D. & Van Veldhoven, P. Ferroelectric properties and fatigue of $PbZr_{0.51}Ti_{0.49}O_3$ thin films of varying thickness: Blocking layer model. *Journal of Applied Physics* **76**, 2405-2413 (1994).
211 Bharadwaja, S. & Krupanidhi, S. Dielectric relaxation in antiferroelectric multigrain $PbZrO_3$ thin films. *Materials Science and Engineering B-Solid State Materials for Advanced Technology* **78**, 75-83 (2000).

212 Hao, X., Wang, Y., Yang, J., An, S. & Xu, J. High energy-storage performance in $Pb_{0.91}La_{0.09}(Ti_{0.65}Zr_{0.35})O_3$ relaxor ferroelectric thin films. *Journal of applied physics* **112**, 114111 (2012).
213 Pertsev, N., Zembilgotov, A. & Tagantsev, A. Effect of mechanical boundary conditions on phase diagrams of epitaxial ferroelectric thin films. *Physical Review Letters* **80**, 1988 (1998).
214 Kang, S. J. & Joung, Y. H. Fatigue, retention and switching properties of PLZT (x/30/70) thin films with various La concentrations. *Journal of Materials Science* **42**, 7899-7905 (2007).
215 Jaffe, B., Cook, J. & Jaffe, H. Piezoelectric Ceramics. *Nonmetallic Solid: Series of Monographs*, 53-57 (1971).
216 Zhai, J. *et al.* Dielectric properties of oriented $PbZrO_3$ thin films grown by sol-gel process. *Journal of applied physics* **92**, 3990-3994 (2002).
217 Scott, B. & Burns, G. Crystal growth and observation of the ferroelectric phase of $PbZrO_3$. *Journal of the American Ceramic Society* **55**, 331-333 (1972).
218 Bokov, A. & Ye, Z.-G. Recent progress in relaxor ferroelectrics with perovskite structure. *Journal of Materials Science* **41**, 31-52 (2006).
219 khil, B. *et al.* Intermediate temperature scale T∗ in lead-based relaxor systems. *J Physical Review B* **80**, 064103 (2009).
220 Rabe, K. M. Antiferroelectricity in oxides: A reexamination. *Functional Metal Oxides*, 221-244 (2013).
221 Lines, M. E. & Glass, A. M. *Principles and applications of ferroelectrics and related materials*. (Oxford university press, 2001).
222 Fujii, Y., Hoshino, S., Yamada, Y. & Shirane, G. Neutron-scattering study on phase transitions of $CsPbCl_3$. *Physical Review B* **9**, 4549-4559 (1974).
223 Sawaguchi, E., Maniwa, H. & Hoshino, S. Antiferroelectric Structure of Lead Zirconate. *Physical Review* **83**, 1078-1078 (1951).
224 Roy Chaudhuri, A. *et al.* Epitaxial strain stabilization of a ferroelectric phase in $PbZrO_3$ thin films. *Physical Review B* **84**, 054112 (2011).
225 Thiele, C. *et al.* Voltage-controlled epitaxial strain in $La_{0.7}Sr_{0.3}MnO_3$ / $Pb(Mg_{1/3}Nb_{2/3})O_3$-$PbTiO_3$ (001) films. *Applied Physics Letters* **87**, 262502 (2005).
226 Jin, J. *et al.* Green Electronics: Chitin Nanofiber Transparent Paper for Flexible Green Electronics. *Advanced Materials* **28**, 5141-5141 (2016).
227 Yao, B. *et al.* Flexible Transparent Molybdenum Trioxide Nanopaper for Energy Storage. *Advanced Materials* **28**, 6353-6358 (2016).
228 Shen, L. *et al.* Epitaxial Lift-Off of Centimeter-Scaled Spinel Ferrite Oxide Thin Films for Flexible Electronics. *Advanced Materials* **29**, 1702411 (2017).